Politecnico di Torino

Politecnico di Torino

Corso di Laurea Magistrale in
Ingegneria Aerospaziale

A.a 2021/2022

Sessione di Laurea Giugno 2022

Skin friction reduction obtained with riblets

Relatori:

Prof. Gaetano Iuso

Prof. Gioacchino Cafiero

Candidato:

Giuseppe Pipia

Index

Chapter 1 - Introduction

Every object in movement in a fluid will generate drag. Drag can be substantially divided in form drag, depending exclusively on the shape of the object moving through the fluid, and skin friction drag, generated by fluid molecules moving across the surface of the object which will experience a slow down.

While form drag has been extensively resolved, with airfoil and profiles that can be used in an efficient manner to hypersonic speeds, the major disadvantage is the poorly understood and somewhat unresolved by humans effect of the skin friction. This kind of parasitic drag is especially present in laminar flows, that are quite rare in nature. During the eons, evolution has found several ways to take advantage of the turbulent flow, thus finding ways to reduce skin friction on birds and fish, to avoid wasting precious resources just to move in their environment. Humans, since the birth of flying, and even when sailing was more prominent, have always been almost

afraid of turbulent flows, always searching for the smoothest surface to apply to any moving object.

Since the discovery of the coherent structures in turbulent boundary layer, first by Kline et al. (1967) and years later mostly summarized by Robinson (1991), there has been a growing knowledge of how the turbulent boundary layer is populated with all kinds of coherent structures, sparking obvious interest into harnessing such structures on our favor. The way to harness turbulence is obviously inspired by nature. If we observe the skins of several predatory animals, like sharks, we can find they are not actually smooth but covered in tiny scales that let them burst in water at speeds of 50km/h, only powered on their muscular force. Later in this thesis there will be a more specific mention on some studies about their particular skin and how some researchers have looked into it to improve the human technology of riblets.

Riblets are tiny ribs that develop in the longitudinal direction of the flow that have promising applications on reducing skin friction. Several have studied riblets in laboratories, reporting an optimistic reduction in skin friction, while Szodruch (1991) covered in 3M riblets 70% of the surface of an Airbus A320,

shown in figure 1.1, and measured a total drag reduction of little less than 2% in the Mach range of [0.77; 0.79].

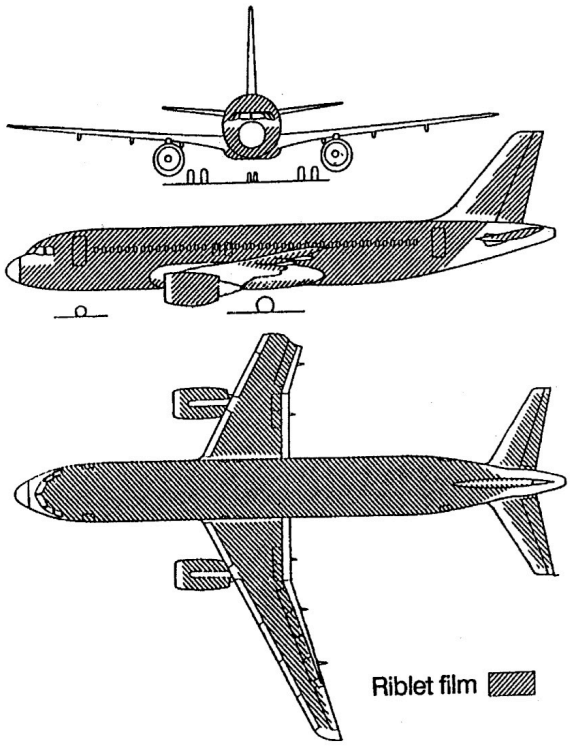

Fig. 1.1: Views of the A320 covered in riblet film. (Szodruch, 1991)

It might not seem a significant decrease, but it's easy to realize that if that reduction is applied for a fleet of several hundreds of aircrafts operating medium range flights, that 2% ends up in a substantial fuel reduction costs for the company operating those flights. As an estimate, Bechert and Hage (2006) considered an Airbus A340-300, one of the choices a decade ago for long-range commercial flights, with 70% of its upper surface covered with a riblet film as shown in figure 1.2. The aircraft has an empty weight of 126t, with a fuel capacity of

80t, capable of transporting a payload of 48t, corresponding to about 295 passengers, topping a maximum take-off weight of 254t. Assuming a fuel cost of about 30% of the direct operating costs, a 2% reduction in fuel consumption, thanks to the same percentage amount of drag reduction, would yield a saving of about 0.7% of the direct operating costs. Although it appears small, it translates into an additional payload of 3.3% or 10 more passengers, giving an increase of 4% in profitability: that means about one million 2005 American dollars every year.

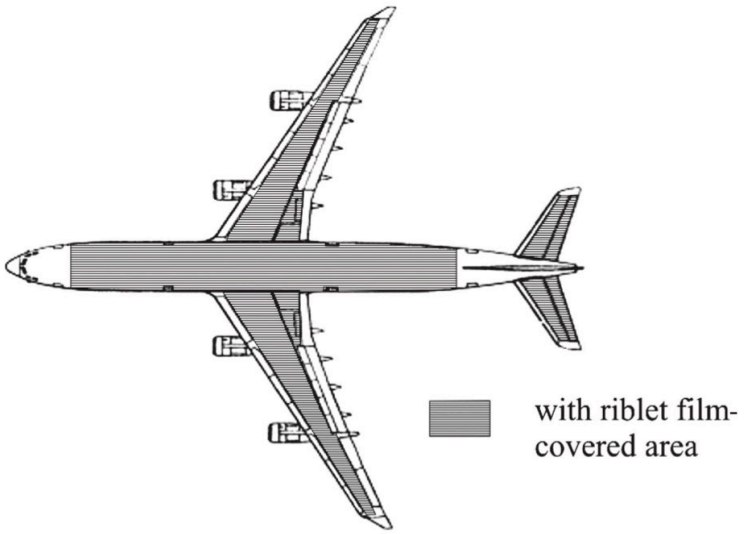

Fig. 1.2: Schematics of long-range aircraft Airbus A340-300 covered in riblet-film on the upper portion. (Bechert and Hage, 2006)

The experimental work, carried out in the aerodynamic laboratory Modesto Panetti of the Polytechnic Institute of Torino, with the guide of Professor Gaetano Iuso and assistant

Gioacchino Cafiero, together with fellow graduate student Luigi Scrimieri, was aimed to assess the drag reduction on several riblets configurations and to define a test procedure to adopt for future research. In the following chapters, the reader will find first a review of current knowledge and understanding of the turbulent boundary layer, with the limitations of current methods, an in depth analysis of how riblets have become of particular research interest in laboratories across the world and how they work, according to the current state of research. Later there will be a description of the experimental facility used for this work and the procedure to acquire the data, which will be then analyzed and discussed and compared to other results found in literature. Lastly few words on how this project will continue and what can be studied in more detail.

Chapter 2 - The turbulent boundary layer

The turbulent boundary layer has been one of, if not the one, the topic attracting much of the attention in aerodynamic research, often not compensated by a true progress in the understanding of the phenomenon. Most of the research could be seen just as purely descriptive articles without any break-through model that would prompt researchers and engineers to use the turbulence in our favor all the times. Even methods that are still taught around the globe, as it will be mentioned later in this chapter, have proven to be highly unreliable for accurate results. In this chapter will be described what the research has looked like, what we currently know of the turbulent boundary layer, and what has to be looked for, to avoid gross mistakes.

2.1 Definitions of the turbulent boundary layer

Any object in a flow will interfere with the flow itself in the same way. The flow away from the object will not change its characteristics, but as we get closer to the object the speed of the flow will decrease to the point, at the surface of the object, to have a zero velocity. The part of the flow in which the flow decreases, as it approaches the surface, its velocity is identified as the boundary layer.

The boundary layer can be laminar or turbulent. The main difference, in a qualitative way, is that while the former has a unique velocity of the flow, that can be determined at every progressive distance from the wall at any given moment, the latter does so in a very limited range, defined as the viscous sublayer, while the rest of the boundary layer hosts a wide variety of velocities, due to small structures recirculating the fluid. The turning point between the two types is defined by the Reynolds number calculated as

$$\mathrm{Re} = \frac{uL}{\nu} = \frac{\rho u L}{\mu}$$

where:

- u is the flow speed [m/s];

- L is the characteristic linear dimension, usually the boundary layer thickness for the turbulent boundary layer, or also the channel half-height or the maximum length of an object, respectively for channel flows and flows around any object, or even the distance between the leading edge of a canonical flat plate and the point along the streamwise direction that is studied [m];

- ϱ is the density of the fluid [kg/m^3];

- μ is the dynamic viscosity of the fluid [N·s/m^2] or [kg/(m·s)];

- ν is the kinematic viscosity of the fluid [m^2/s].

This ratio gives an idea of which is stronger between the inertial forces, found in the numerator, and the viscous forces, found at the denominator. If their ratio is less than 1, then viscous forces are predominant, if it is greater than 1, then the inertial forces are the predominant ones. The higher the Reynolds number, the more turbulent the flow will be.

The boundary layer is often divided into two main regions, in relation of their position from the wall: the inner and the outer

regions. The viscous sublayer is located in the inner region: it is here that the energy coming from the outer region, is dissipated by the viscous forces, which ultimately generate friction on the wall. This subdivision is visible in figure 2.1 by Akindale (2005).

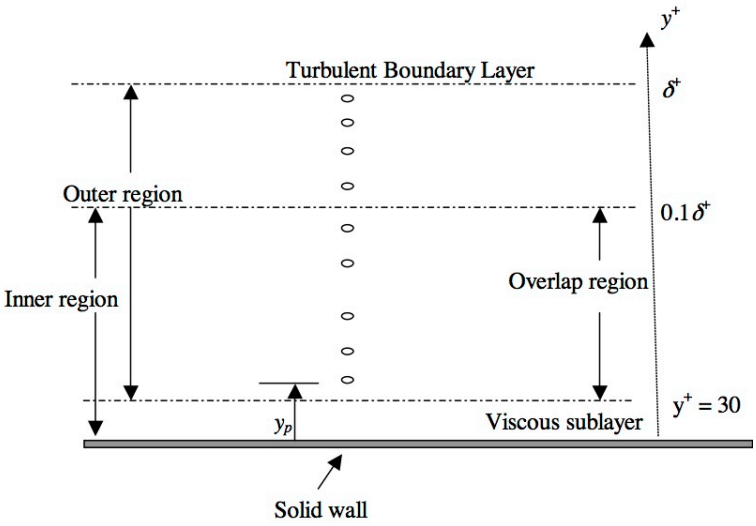

Fig. 2.1: Graphical distinction of the the outer, overlap, and inner region, with increasing wall units. (Akinlade, 2005)

On the wall it's applied the hypothesis that the fluid is standing at zero velocity. The shear stress can be calculated according to the formula obtained from Newton's second law

$$\tau = \mu \frac{\partial U}{\partial y} - \rho \overline{u'v'} = \tau_w$$

where the amount that is subtracted, containing the fluctuations of the velocity components, is known as the Reynolds stress tensor. Therefore to the total amount is added

the foot *w*. Once this quantity is known, we can calculate the shear velocity according to the formula

$$u_\tau = \sqrt{\frac{\tau_w}{\rho}}$$

Then we can normalize the velocity and the distance from the way, by the following, so called, wall variables:

$$\begin{cases} U^+ = \dfrac{U}{u_\tau} \\ y^+ = \dfrac{y u_\tau}{\nu} \end{cases}$$

Using the spacial coordinate as the independent variable and the velocity as the dependent variableIn the inner region, the velocity profile is linearly dependent from the distance from the wall as in the relation

$$U^+ = y^+$$

which is a first order approximation, as Bernard et al. (2002) and Pope (2000) proved, of the evaluation with a Taylor series expansion at the wall of the integration of the streamwise momentum equation. Prandtl (1925) firstly proposed it, along with its range of validity, within the first 5 wall units, in the inner layer.

After the discovery of the linear wall, Prandtl and his student von Kármán were in a "world competition" as the latter stated

after Prandtl won a battle by introducing in 1926 the concept of the mixing length.

Von Kármán (1930) won the second round. In high Reynolds number flows, the inner layer shows a velocity profile described by the wall units, regardless of the thickness of the boundary layer and the outer velocity such as

$$\frac{du^+}{dy^+} = \Phi_{inner}\left(y^+\right)$$

while for the outer region the viscosity doesn't influence the velocity profile, that can be described as

$$\frac{du^+}{dy^+} = \Phi_{outer}\left(\frac{y}{\delta}\right)$$

Then, for

$$l_\tau \ll y \ll \delta$$

which considers a distance from the wall greater than the mixing length suggested by Prandtl, but still smaller than the height of the boundary layer, the following is obtained

$$\Phi_{inner}\left(y^+\right) = \Phi_{outer}\left(\frac{y}{\delta}\right)$$

satisfied only if the two equations are constant, therefore

$$\frac{du^+}{dy^+} = \frac{1}{ky^+}$$

from which, by integrating this last relation, von Kármán was able to obtain what has become known as his formula for the logarithmic law of the wall

$$U^+ = \frac{1}{k}\ln y^+ + B$$

with proposed value of k equal to 0.36 for thee mean velocity and 0.38 for the friction relation, while B was the intercept. Modern values for these constants have varied, for wall bounded flows independent of pressure gradient, around

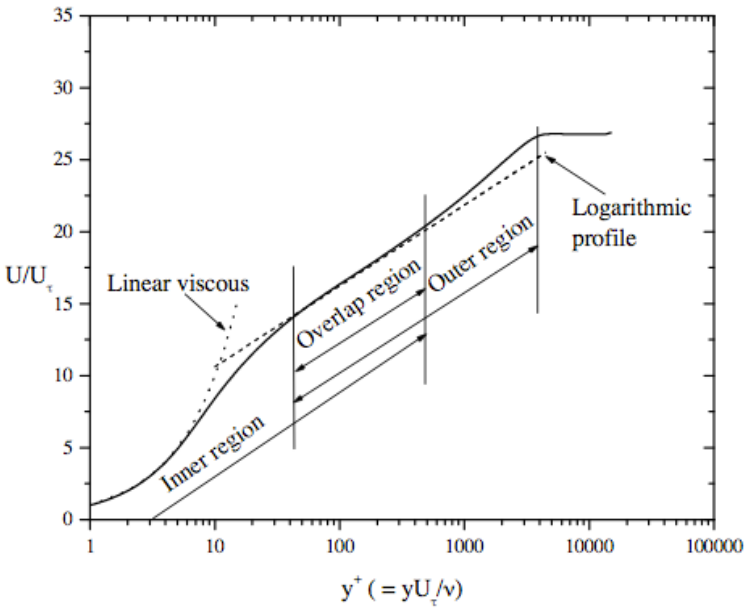

Fig. 2.2: Schematic diagram of the velocity profiles in the inner, overlap, and outer regions of a turbulent boundary layer. (Akinlade, 2005)

k=[0.37; 0.41] and B=[4.17; 5.5]. The same relationship was derived later on by Prandtl (1932) and Millikan (1938), the latter using asymptotic matching. In figure 2.2 it is shown a

schematic of what the velocity profiles would look like in a semi-logarithmic graph.

The extension of the logarithmic region, found in the inner layer, has not been fully determined. Nor has been even the name, since it has been referred to as "inertial sublayer", "intermediate layer", "fully turbulent layer", "constant stress layer" and others as mentioned by Örlü (2010) in his review. Usually the lower limit is located between 30 and 50 wall units, although Zagarola and Smits (1998) even proposed a lower limit of 600 wall units. Meanwhile, the upper bound of the logarithmic region is calculated as

$$\eta = y/\delta \approx \left[\quad 0.1; \quad 0.2 \quad \right]$$

where δ is the thickness of the boundary layer.

Taking into consideration von Kármán's law, multiplying both side by the ratio of the friction velocity and the velocity of the undisturbed flow yields the following relation

$$\frac{U(y)}{U_\infty} = \left[\frac{1}{k}\frac{u_\tau}{U_\infty}\right]\ln\left(\frac{yU_\infty}{\nu}\right) + \left[\frac{1}{k}\frac{u_\tau}{U_\infty}\ln\left(\frac{u_\tau}{U_\infty}\right) + B\frac{u_\tau}{U_\infty}\right]$$

Introducing the friction coefficient, defined as

$$C_f = 2\left(\frac{u_\tau}{U_\infty}\right)^2$$

the logarithmic law can be rewritten as

$$\frac{U(y)}{U_\infty} = \left[\frac{1}{k}\sqrt{\frac{C_f}{2}}\right]\ln\left(\frac{yU_\infty}{\nu}\right) + \left[\frac{1}{k}\sqrt{\frac{C_f}{2}}\ln\left(\frac{u_\tau}{U_\infty}\right) + B\sqrt{\frac{C_f}{2}}\right]$$

which is known as the Clauser's chart equation, firstly introduced in 1956. Since then this formula has been used widely in textbooks and research to calculate the skin friction coefficient. The reason it has been so widely used is that the velocity profiles can be easily measured via several means, from Pitot tubes to hot-wire anemometry, they can be plotted against a group of lines obtained by varying the drag coefficient. Hence, by an easy comparison between the experimental data and the analytical data, the coefficient is easily determined, assuming the values of k and B constant.

2.2 Inaccuracies in wall similarities methods

As the research has become more refined, it didn't last long to notice that the Clauser chart method to determine friction

velocity and skin friction was flawed, to say the least. While a part of the research focused on the global effectiveness of the log-law on describing the velocity profile in the boundary layer, for example made by Bradshaw and Huang in 1995, but also proposing new additions as the wake parameter, given formally by Coles (1956), others have focused whether or not the von Kármán constants are indeed constants or they show some dependency to the Reynolds number. The latter is easily shown. Taking as an example the hypothetical situation suggested by Wei et al. (2005), they imagined an experiment to determine velocity profiles of turbulent boundary layer flow, measuring the velocity at different locations that would correspond to different and increasingly higher Reynolds numbers. They write that the friction velocity calculated by Clauser's method would be a certain amount of the true friction velocity as follows

$$u_{\tau_c} = f\left(\mathrm{Re}\right)u_{\tau_t}$$

which substituted into the original equation will yield

$$\frac{U\left(y\right)}{u_{\tau_t}} = f\left(\mathrm{Re}\right)\frac{1}{k}\ln\left(\frac{yu_{\tau_t}}{\nu}\right) + f\left(\mathrm{Re}\right)\left(B + \frac{1}{k}\ln\left(f\left(\mathrm{Re}\right)\right)\right)$$

The difference between the true and the calculated friction velocities would then be equal to

$$\frac{u_{\tau_t} - u_{\tau_c}}{u_{\tau_t}} = 1 - f\left(\mathrm{Re}\right)$$

which ranges from 20% to -20% in 10% increments if f(Re)=[0.8; 0.9; 1.0; 1.1; 1.2], giving the graph shown in figure 2.3.

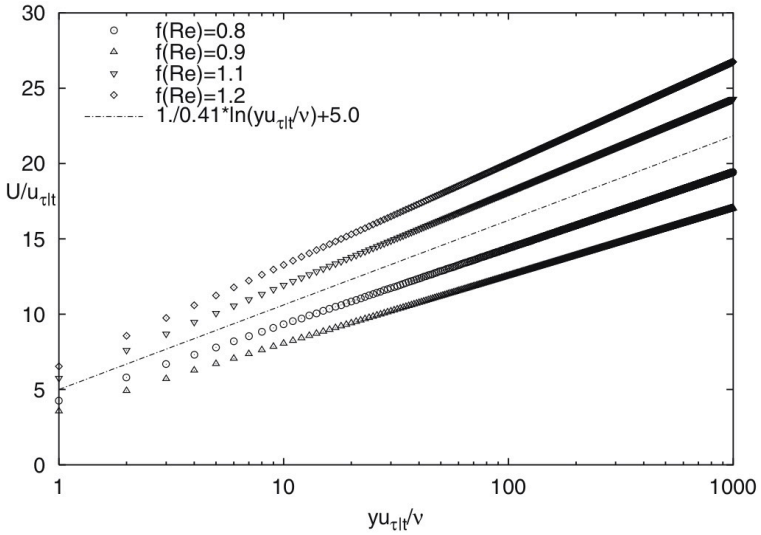

Fig. 2.3: Velocity profiles generated with different values of f(Re). (Wei et al., 2005)

If Clauser method is used the graph in figure 2.4 is obtained: while in figure 2.3 the differences were clear, in figure 2.4 the differences collapsed, as a direct result of the assumption of the method, leading to potentially wrong conclusions one how the mean velocity profiles scale with Reynolds number. Wei et al. (2005) showed that this applies also on weak Reynolds

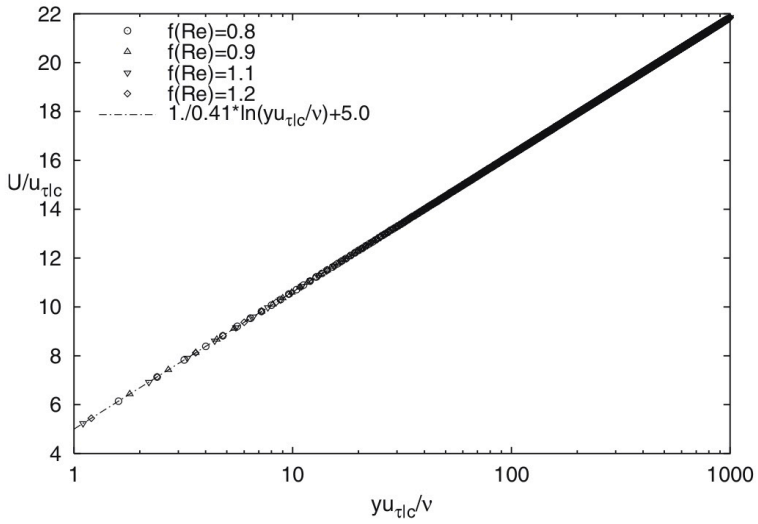

Fig. 2.4: Velocity profiles of figure 2.3 normalized by friction velocity obtained with the Clauser chart method (Wei et al., 2005)

number dependence, demonstrating how pervasive this issue is for pipe flow data, using the data of Patel and Head (1969), and also for turbulent boundary layer flow data, taking into consideration the data collected by Purtell et al. (1981). This striking effect is particular strong at low Reynolds numbers, but it diminishes as the Reynolds number increases.

Determining the wall position is also a challenge that could lead to gross mistakes in the evaluation of skin friction, as thoroughly explained by Örlü et al. (2010). In his paper, he explained how several studies showed flaws in their results when taking measurements of the sublayer. For example Patel (1965) used a Pitot tube which is way too big to actually resolve the tiniest portions of the sublayer, and also it surely

disrupt the boundary layer at that level. The same applies to even studies conducted with a hot-wire, like the cited work of Blackwelder and Haritonidis (1983). Even more sophisticated techniques to measure the distance between the sensing probe and the wall can have their shortcomings. The most frequently used instrument to measure that distance are instruments like microscopes, theodolites and cathetometers. Microscopes separately focus on the wire and then the wall to define the correct distance; with the other two ways, the distance is extracted by halving the distance from the wire to its image reflected from the polished wall, conceded that the viewing angle is perfectly perpendicular to the distance from the sensing probe to the wall. Another possible way to measure the distance from the wall is using a laser. These methods, although they offer accuracies in the order of micrometers, have the necessity to be optically accessible, which for several experimental conditions is not a viable option, like for internal flows. In such cases some researchers, like Azad and Burhanuddin (1983) or McKeon et al. (2004), resolved the issue by making an electrical contact between the sensing probe and the wall. In this case, however, there's the need of a conductive

wall, and also the probe might be lost by a less than ideal contact, since most of the times the probes are moved by a stepping motor. So extreme care is needed in these scenarios. Also, as mentioned by Hutchins and Choi (2002), since the probe is very small and prone to deformations, it is impossible to make electrical contact at the same point each and every time, making this procedure less accurate than it is thought to be.

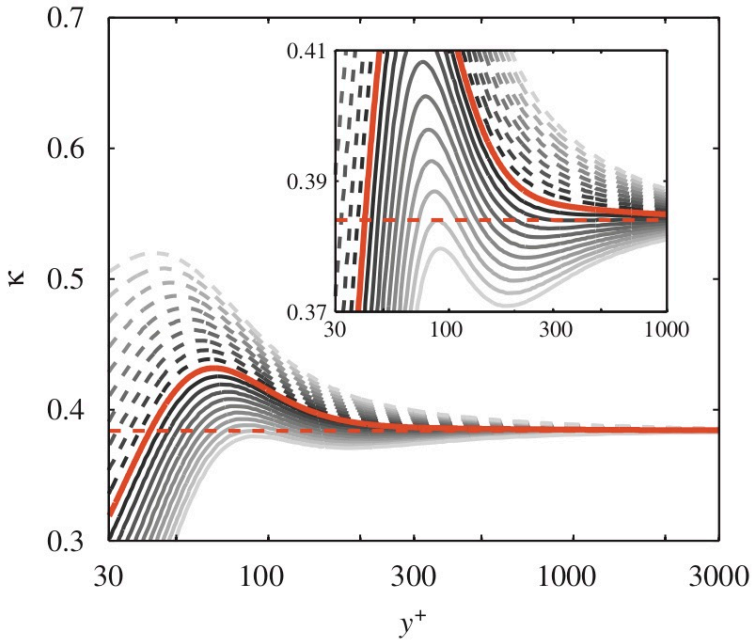

Fig. 2.5: Effect of the inaccuracies in the determined wall position on the von Kármán constant, obtained through the logarithmic indicator function. The thick red line represents the profile for the correct wall position; the dashed and solid gray lines represent negative and positive offset respectively. (Örlü, 2010)

How strong the influence of the wall position is on the parameter k in the log law is shown in figure 2.5, taken from Örlü et al. (2010): in this case the velocity profile description for

the law of the wall comes from the composite profile proposed by Chauhan et al. (2009). The dashed red line represents the asymptotic value of k=0.384, the thick red line represents the correct wall position, the dashed grey lines and the solid grey lines respectively represent the negative and the positive offsets from the correct position of the wall, with decreasing

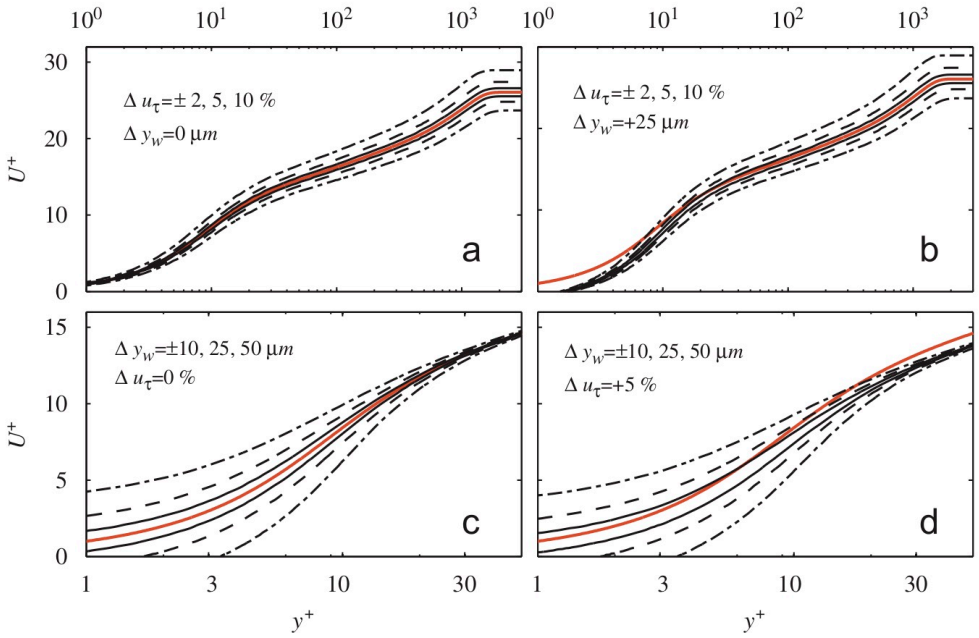

Fig. 2.6: Effects of inaccuracies, particularly: in the determined friction velocity for a) correct and b) erroneous wall position; in the determined wall position for c) correct and d) erroneous computed friction velocity. (Örlü, 2010).

intensity the further the wall is. Figure 2.6 depicts the effects of a wrongly deduced friction velocity and wall position on the inner scaled mean streamwise velocity component, by plotting the data generated from the experiment by Chauhan et al. (2009) with a nominal friction Reynolds number equal to 2000,

and a viscous length scale of 15μm[2]. Figures 2.6 (a) and (b) show what a wrongly deduced friction velocity does to, respectively, a correctly and wrongly deduced wall position, while figures 2.6 (c) and (d) show what a wrongly positioned wall can do to, respectively, a correct and wrong friction velocity. As shown by the graphs in figures 2.5 and 2.6, the effect of such inaccuracies are predominant in the inner layer, and for low Reynolds numbers, while for distances upward of 30 viscous units from the wall, the discrepancy disappears. The same happens if the Reynolds number is very high. Nonetheless some countermeasures have to be taken into account to at least mitigate the issue of not directly measuring the skin friction.

In the same article Örlü et al. (2010), proposed to use more terms of the Taylor series expansion of the linear law of the wall, firstly introduced by Monin (1971) and Townsend (1976), which is

$$U^+\left(y^+\right) = y^+ - \frac{\left(y^+\right)^2}{2\,\mathrm{Re}_\tau} - \frac{\sigma_1}{4}\left(y^+\right)^4 + \frac{\sigma_2}{4}\left(y^+\right)^5 + \cdots$$

where the second order term, which is divided by the friction Reynolds number therefore it becomes negligible and tends to

zero as the Reynolds number increases above 300. Therefore by using this formulation of the linear law of the wall on the database of direct numerical simulation data collected by Tsukahara et al. (2005), Kawamura (1999) and Abe (2004), Örlü et al. (2010) found that the linear velocity profile overestimated

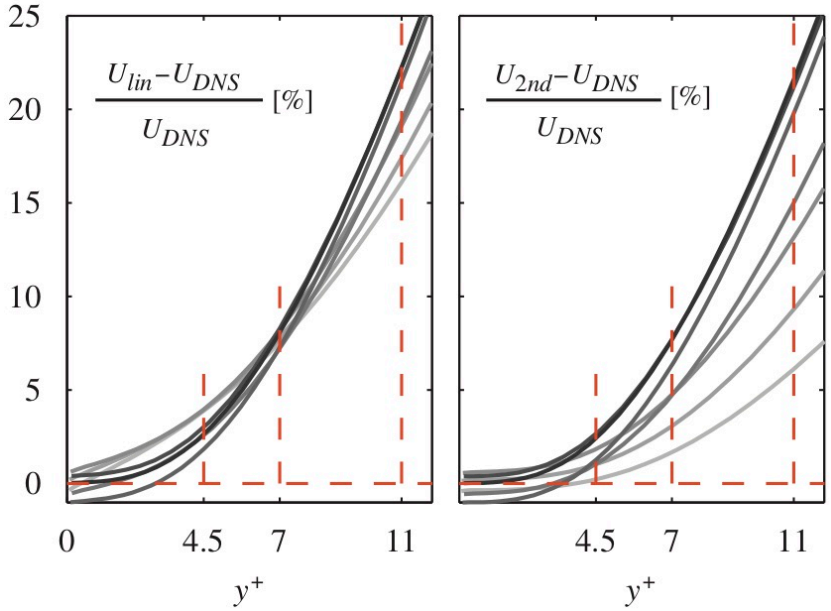

Fig. 2.7: Relative deviation of the linear profile a) without and b) with the second order term from the DNS. (Örlü, 2010).

the DNS results by 2.5% at y+=4.5, while for higher Reynolds numbers, at distances equal to [7, 11, 15], the linear law of the wall overestimates the velocity to respectively about 8%, 20% and even 40%. Instead, by using the second order term of the approximation, the error diminishes as shown in figure 2.7. Finally, how also Hutchins and Choi (2002) reported, to better characterize the inner layer many data sets are needed, even

over 80 individual velocity measurements to achieve a way skin friction with a standard error of ±1.8%.

Another issue is represented by the extension of the actual linear profile: while Cenedese et al. (1998) demonstrated that the quadratic term doesn't extend the useful range, the same group of research and, later on, Park and Chung (2004) showed that the quartic term is able to describe the flow within 5% accuracy up to a distance of about 6/8 wall units, although their studies were based on data of low Reynolds number channel flow DNS, with an important pressure gradient that is represented via the Reynolds number included in the quadratic term. Instead, for high Reynolds numbers, Örlü et al. (2010), by using DNS channel data from several other authors, showed that including the fourth and fifth order terms of the linear law of the wall extends its validity range up to, respectively, 9 and 15 wall units, well beyond the traditional range. This made Örlü et al. (2010) suggest that using the forth and fifth order terms up to y+=15 could be a valid way to determine skin friction and wall position for canonical wall-bounded flows, but being cautious on using this method when a high number of measurements in the viscous layer is available.

For higher Reynolds number flows, it is not always possible to use only near-wall data to determine the wall position, so research has also focused on finding a law that could interpolate between the linear law of the wall and the logarithmic law. This led Coles (1956) to formally propose the first formal description of a mean velocity profile law of the wall with the presence of an additive wake function such as

$$U^+_{\text{composite}} = U^+_{\text{inner}}\left(y^+\right) + \frac{2\Pi}{k} W\left(\frac{y^+}{\delta^+}\right)$$

where ∏ is the wake parameter and W is the wake function dependent on the relative distance from the wall. However this law is highly dependent on data availability and advanced curve fitting, as Örlü et al. (2010) pointed out.

In conclusion, to determine the wall position and the skin friction velocity it is highly advisable to either have a high number of measurements in the viscous sublayer, or using direct methods, that will actually take a measurement of the friction on the wall, as done in this research project.

2.3 Historical review, taxonomy and models of turbulent structures

While the previous pages have reported the basic ideas behind the turbulent boundary layer, it is interesting and useful to the reader to better understand the mechanisms of turbulence. It will help in the further reading on how the riblets have been conceived and why they promise to be highly efficient. Firstly a historic review that brought major breakthroughs in the understanding of the boundary layer, especially the fact that the viscous sublayer is not really laminar and that the main production of turbulence is located in the buffer region. Then an overall explanation of the main structures that can be identified in the turbulent boundary layer and finally a rundown on the main models proposed on how turbulence expands all over the boundary layer.

2.3.1 Historical review on the turbulent boundary layer research

Along side the analytical descriptions of the turbulent boundary layer, there is also interest on what is actually

happening inside the turbulent boundary layer in a deeper understanding of the motions that give those mean streamwise velocities described in the previous pages. The turbulence production in the boundary layer happens in the buffer region, that area where the viscous layer becomes the logarithmic layer. The production is either caused by violent outward ejections of low-speed fluid or inrushes of high-speed fluid at a shallow angle toward the wall. In the outer region, instead, in the interface between the turbulent and non-turbulent area, there is the formation of three-dimensional bulges, comparable to the scale of the boundary layer thickness. These mechanisms cause severe three-dimensional fluctuations of velocity, which prompted Reynolds in 1894 to propose a decomposition in a mean component and a fluctuating one, the latter being implicitly thought to be random, allowing for statistical analysis. However several people noticed that the repeating sequences of events in the turbulent boundary layer appeared in the midst of random fluctuations, making question the approach of average statistical representation of the turbulent fluctuations were actually adequate to study turbulent flows. In facts, Reynolds-averaged turbulence modeling

approaches do not explicitly include an intermittent three-dimensional motion. This constant inability of Reynolds-averaged turbulence models to accurately predict many turbulent flows, along with a need for a deeper understanding of the underlying physics have guided at least two generations of scientists, since the discovery of turbulent motions. Robinson (1991) distinguished four main periods in which important discoveries and/or better technology has been made in the study of turbulent motions:

- the discovery era (1932-1957);
- the flow visualization era (1958-1971);
- the conditional sampling era (1972-1982);
- the computer simulation era (1983-present).

The first period starts when Prandtl (1932) defined the turbulent boundary layer regions, as mentioned previously, along with his student von Kármán (1933) and Millikan (1938) helped describing how the mean streamwise velocity varies depending on the distance from the wall. In a matter of few years, there were the first studies about the turbulence generated in the boundary layer pointing that it was not a continuously random field of velocity fluctuations, but more

organized and repeating motions were populating the outer and near-wall regions. Research was performed on: intermittency in the turbulent/potential interface at the edge of turbulent flows by Corrsin (1943); the large-eddy motions in the outer regions of the boundary layer by Townsend (1956); coherent features in the near-wall region, including the sub-layer streaky structure and violent ejections of near-wall fluid, by Einstein and Li (1956) and Kline and Runstadler (1959). It can be called the discovery era because what research had found was against the knowledge of that time, for example the presence of continual three-dimensional and unsteady motions what was thought to be the laminar viscous sublayer.

Such discoveries sparkled vigorous controversies on their dynamical and statistical relevances, fueling research to better characterize the coherent motions. By this time the flow visualization was the preferred mean of research, combined with quantitative probe anemometry, to try to comprehend the buffer region, where the turbulent production is at its maximum, and the viscous sublayer, with its newly discovered non laminar structure. It was settled, by the works of several authors like Kline et al. (1967), Kim et al. (1971) and Offen &

Kline (1974, 1975), that coherent motions play major roles in the production of new turbulence near the wall and the transport of momentum from outer to inner regions and viceversa, marking the main achievements of the flow visualization era.

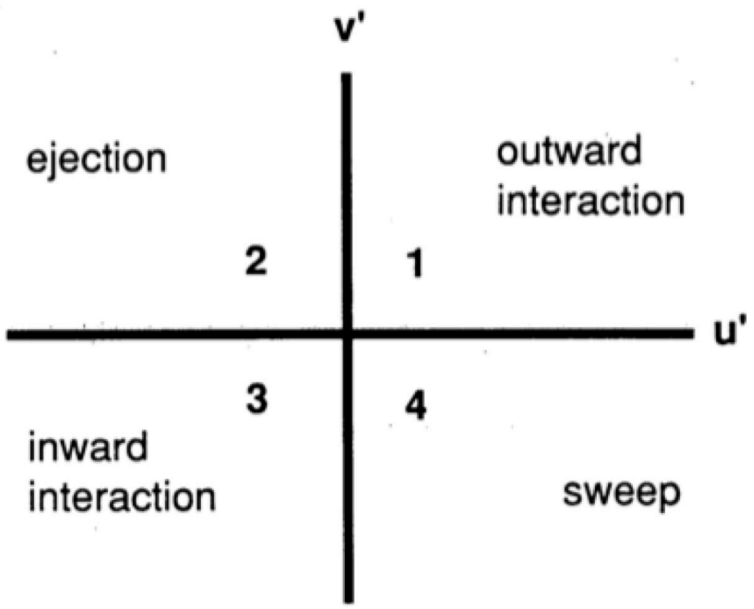

Fig. 2.8: Subdivision of the quadrants and relative structures of the instantaneous u'v' plane. (Wallace et al., Willmarth and Lu, 1972, Robinson, 1991)

Wallace et al. (1972) and Willmarth and Lu (1972) were the first to actually use the quadrant splitting of the u'v' signal, even if more analogue techniques were still broadly in use. The scheme, reported in figure 2.8, denotes the fluctuation velocities u' and v' and it helps determine what motions are present in the flow. Particularly, as noted in the picture, the motions that occupy the second quadrant are identified as

ejections, while those that are located in the fourth quadrants are called sweeps. This new technique was made possible thanks to the availability of cheaper digital laboratory computers, yielding a community-wide transition and focus on conditional sampling methods, hence the beginning of a new era. Robinson (1991) states that the major controversy over the unknown scaling parameters for the frequency of bursts detected by a stationary probe. Such dilemma was first motivated by the unresolved issue about the dominance of near-wall events over a regenerative cycle of turbulence generation near to the wall, and then if the production processes were instead the result of the passage of outer-flow motions. This problem remains still unresolved, although it is thought to be dependent on the Reynolds number.

Starting from 1980, computers with graphical user interface helped researchers to probe numerically simulated turbulence in search of those answers that experimentalists could not find, no matter how hard they tried. Thanks to means of direct numerical simulations, computing the three-dimensional fields of pressure, vorticity, and velocity fields, the experimental

community shifted their focus to a better understanding of the physics behind the three-dimensional coherent motions.

What was learned in the past 80 years of experimental research can be summarized in the following points, according to Robinson (1991):

- the viscous sublayer is not laminar and the buffer region is not transitional in the laminar-to-turbulent sense;
- the sublayer, buffer region and outer region have each coherent motions with different structural characteristics;
- the sublayer is mainly comprised of elongated, unsteady regions of high and low speed streamwise velocity,
- the near-wall buffer region is the most important for the turbulent boundary layer, since it is where the production and the dissipation of coherent motions take place. Particularly the activity is mainly represented by a bursting process, defined as a sweep of high-speed fluid upstream of a low-speed ejection;
- the outward ejections of low-speed fluid and slightly wallward sweeps of high-speed fluid show an intermittent behavior in the wall region. Both are the main contributors to the Reynolds shear stress;

- throughout the boundary layer and whenever there's interaction between upstream high speed fluid and downstream low speed fluid a thin shear layer can be found. Such layers show a high slope of about 12° to 18°, that gets to about 2° to 4° as they approach the wall;

- the main structures in the intermittent region are large scale motions, existing beneath three-dimensional bulges in the outer interface. Such bulges often appear along with a well defined upstream "back", which is a slow rotational motion in the direction of the mean strain, and deep crevasses of high-speed potential fluid around the edges;

- the potential fluid is usually entrained in the valleys of the turbulent/non-turbulent interface located at the edges of bulges;

- the transverse vortices are found in the outer region;

- the streamwise vortices, with slight upward slope, are located in the wall region.

2.3.2 Taxonomy of structures

At this point it is relevant to point the structures that have been found, though the years of research of the turbulent boundary layer. Although classification is arbitrary because of not well defined rules, a useful distinction was made by Kline and Robinson (1989 a,b), who outlined the descriptions of eight possible structures known as:

- Wall low-speed streaks;
- Ejections of low speed fluid outward from the wall;
- Sweeps of high-speed fluid inward toward the wall;
- Vortical structures of various forms;
- Near-wall shear layers;
- Near-wall pockets;
- Large motions in the outer turbulent/potential interface;
- Backs of large-scale outer-region motions.

The wall low-speed streaks could be defined as regions of fluid at high or low speed that form a streaky structure at the wall. They help identify a wall-bounded flow as either turbulent, simply unsteady or laminar. It's important to differentiate them with the streaks lifted into the buffer region and beyond. They can grow to an approximate mean of 100 viscous lengths,

mode of 80 and a log-normal distribution, as reported by Kim et al. (1971), with a spanwise dimension varying from 20 to 60 viscous lengths, and could even extend to a thousand or more viscous lengths on the canonical flat plate boundary layer studied by Kline et al. (1967), showing a sinusoidal behavior, branching and reconnecting over time. They seem to be Reynolds number independent as Smith and Metzler (1983) reported, adding that the spanwise spacing increases as the distance from the wall outside the sublayer. Robinson (1991) supposed that the most likely way the streaks form is from single quasi-streamwise vortical elements convecting downstream, which leaves some near-wall low-sped fluid trailing from the upward rotating side of the vortices, and high-speed fluid on the downward rotating side of them. Since the streamwise velocity gradient is highest near the wall, the severe shearing action from lifting low-speed regions results in streaks being longer than high-speed regions.

Ejections of low-speed fluid outward from the wall and sweeps of high-speed fluid inward toward the wall, can be easily identified with the help of the quadrant splitting technique, proposed by Wallace et al. (1972) and Willmarth and

Lu (1972), which scheme is reported in figure 2.8. An ejection is defined as any motion that occupies the second quadrant of the u'v' plane, while a sweep is found occupying the fourth quadrant of the same plane. Kim et al. (1971) considered ejections fundamental in the bursting process and occur intermittently when observed from a stationary frame of reference. Robinson (1991) pointed out that their intermittent behavior is more prominent in space than in time, which leads to another view of the bursting process, becoming more of a localized ejection of fluid from the wall caused by a passing quasi streamwise vortex or more of them. Ejections are also contributors to the positive Reynolds shear stress. Meanwhile sweeps are described by Corino and Brodkey (1969) as a large scale, front-like motion sweeping away near-wall ejection activity, and then moving downstream at the local mean streamwise velocity. However Corino and Brodkey did not consider them also contributors to the Reynolds shear stress, which was later overturned by Grass (1971) and they were even found to be dominant contributors to -u'v'. Sweeps are also highly intermittent in space, as found by Robinson (1991) which proved that sweeps in the buffer zone are locally produced and

that direct mass transfer the outer flow is relatively uncommon. In figure 2.9 is an example of a boundary layer populated with ejections and sweeps at y^+=15.

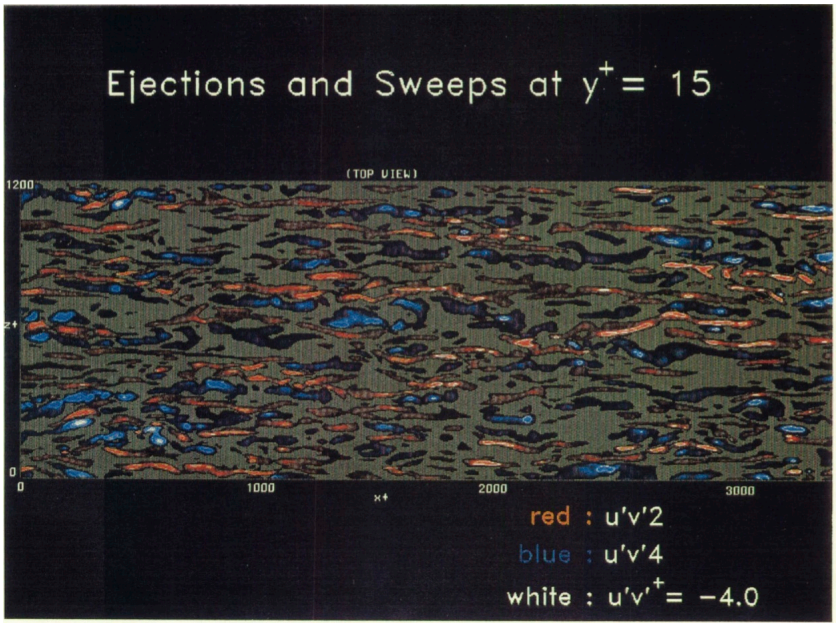

Fig. 2.9: Example of turbulent boundary layer at y+=15 populated with ejections (red) and sweeps (blue). (Robinson, 1991)

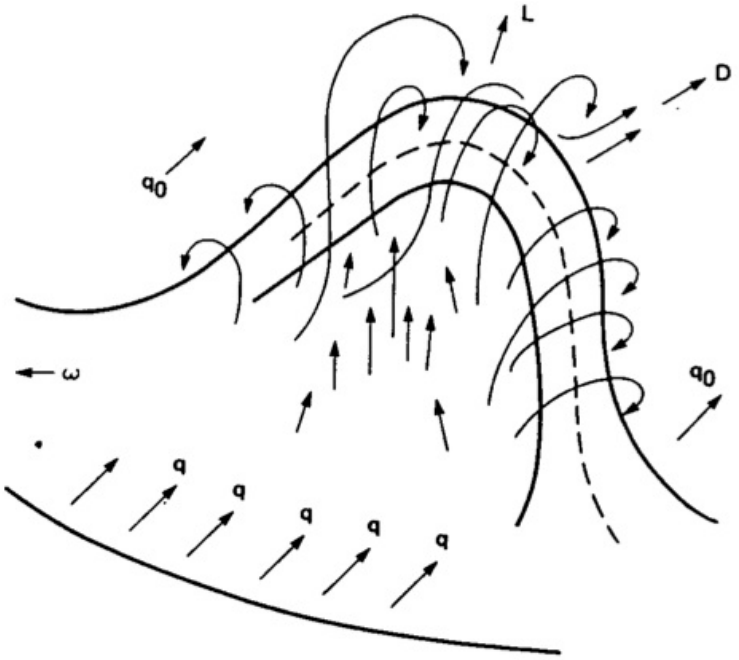

Fig. 2.10: Schematic of primary structure of wallbound turbulence. (Theodorsen, 1952)

Vortices of various shape and dimensions are the main motions that have been studied throughout the decades. Firstly Theodorsen (1952) proposed a model on their formation, figure 2.10, suggesting that vortical tornadoes form in the near-wall regions of low-speed fluid, growing outward with heads inclined downstream at 45°, and spanwise dimensions proportional to the distance from the wall. Vortices in three dimensions often resemble arches or horseshoes, at low and moderate-low Reynolds numbers, or hairpins, at high Reynolds numbers, and populate all the regions of the turbulent boundary layers, as visible in figures 2.11 and 2.12, taken from Robinson (1991). In an x-y cross-section of a hairpin, three main features can be identified: a transverse vortex core of the head that rotates in the same direction of the mean circulation; a low momentum fluid region situated below and upstream of the vortex head; an inclination of the low momentum fluid region of about 35° to 50° from the streamwise direction, below the transverse vortex. Zhou et al. (1996, 1997, 1999) showed that as the hairpin vortices get closer to the wall their legs become longer and quasi-streamwise, which are the main cause of the low-speed streaks previously mentioned and

found in the buffer region, the main area of turbulence production.

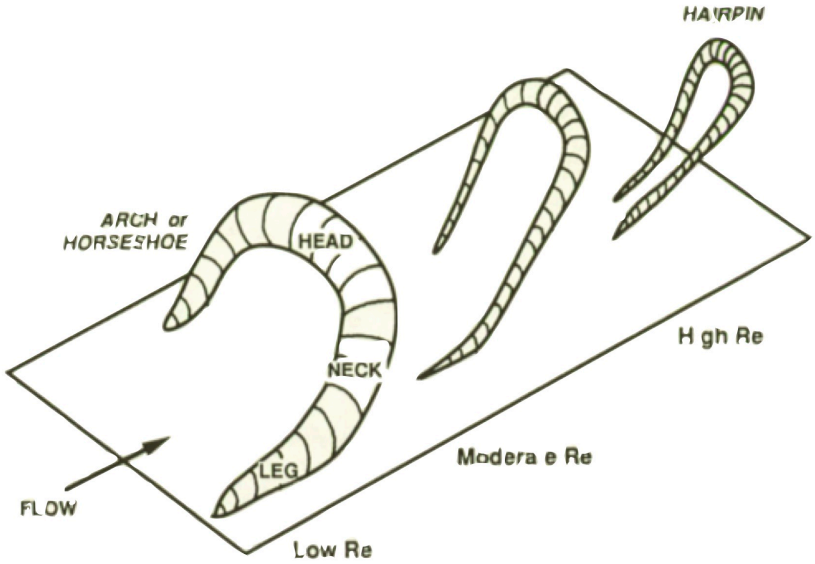

Fig. 2.11: Schematic of vortices dimensions and shape depending on the Reynolds number. (Robinson, 1991)

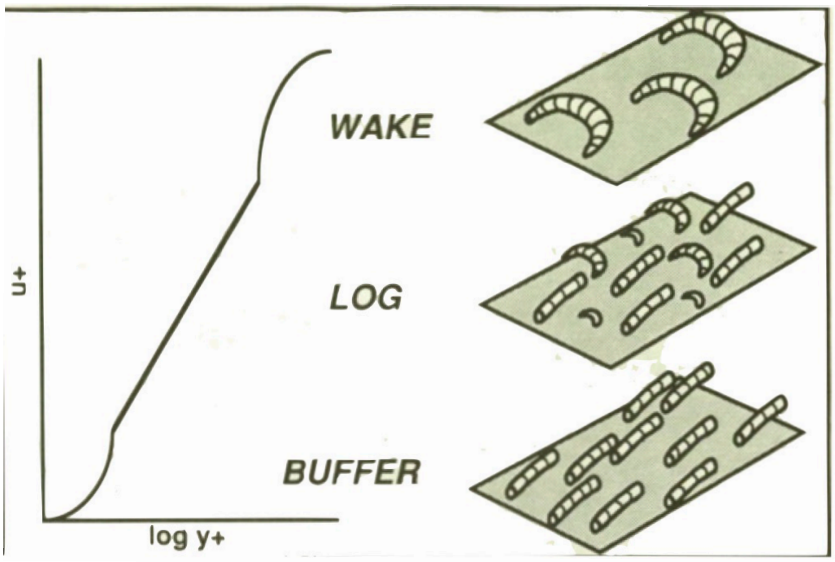

Fig. 2.12: Schematic of the various types of vortical structures in the different regions of the turbulent boundary layer. (Robinson, 1991)

Close to the wall, and up to a distance of 80 viscous units, is the area in which near-wall shear stresses are mostly common.

These structures show a high vorticity everywhere, while a low-pressure region appears to form at the outer tip. The latter feature was reported by Robinson (1991) as the core of a transverse vortex. In the narrow band between 30 and 80 viscous lengths from the wall, rollup may occur, showing that near-wall shear layers are not major direct producers of turbulence, however shear-layer instability could become a significant player in vortex formation in the log region. What happens is that the shear layer sees a concentration of vorticity, that eventually becomes the dominant feature of the layer itself. The formed vortex head separates from the shear layer and moves downstream evolving into a series of vortices.

Near-wall pockets were firstly defined by Falco (1980) as loosely circular regions devoid of marked fluid appearing in plan view, giving the visual impression of a kind of trace of some outer structure that induces fluid toward the wall. Later, Falco (1982) indicated that their formation is due to the impingement of a ring-shaped eddy upon the viscous sublayer. Their spanwise dimensions range from 50 to 100 viscous lengths as reported by Robinson (1991), which also suggested

that pockets are likely to be the effect of fluid swept toward the wall by vortical structures.

Finally the larger structures that are found at the interface between the turbulent boundary layer and the irrotational free stream, such as the large-scale bulges. These motions were attributed by Kim et al. (1971) and Blackwelder and Kovasznay (1972) to the near-wall ejections of fluid into the outer region, while Willmarth and Lu (1972) and Nychas et al. (1973) attributed them to the presence of outer-region vortical structures. Another feature bound to these structures is their backs, basically a share layer formed by the impingement of high-speed fluid over thee slower fluid found upstream of the large-scale motions, as confirmed by Falco (1977). Their spacing in the streamwise direction as well as their height scale with the boundary layer thickness, however their streamwise extensions is limited between 10 and 40 viscous lengths.

2.3.3 Vortices and turbulence production models

A relevant role is played by the vortices that, in various stages and sizes, populate the turbulent boundary layer and

transport mass and momentum throughout its extension. It is important to end this chapter by mentioning how vortices work and what the current knowledge and understanding are regarding turbulence production.

Although Theodorsen (1952) was the first to propose a model, it did not include the quasi-streamwise vortices that represent the legs of the hairpin. Years later there were two new proposed models: Willmarth and Tu (1967) explained the transformation from initially two-dimensional transverse vorticity lines into three-dimensional hairpin shapes sloped downstream at about 10° from the wall. Such structures showed vorticity lines and a streamwise component. The model was limited only to the near-wall region, but left the suggestion that near-wall hairpin vortices could eventually evolve to larger scale structures, yielding an interaction between the inner and outer regions. Black (1968) proposed a flow model based on horseshoe vortices shed from a near-wall instability. Initially the vortex structures are closed loops, i.e. rings, but what happens next in their evolution is a separation: the lower part dissipates in the viscous sublayer, while the upper part develops outward and downstream, becoming a

horseshoe-shaped vortex. Then the heads move away from the wall, therefore stretching the trailing legs and inclining the horseshoe vortex. The vortices were found to induce an outflow of low-speed fluid from the vortex loop: a stationary probe would see the low-speed fluid as an intermittent spikes of Reynolds shear stress. Black (1968) finally suggested that a structure that includes several horseshoe elements at different stages of growth, while sharing a common trajectory in space. Figure 2.13 represents the intermittency explained by random variation in strength of consecutive vortex systems, taken from Black (1968).

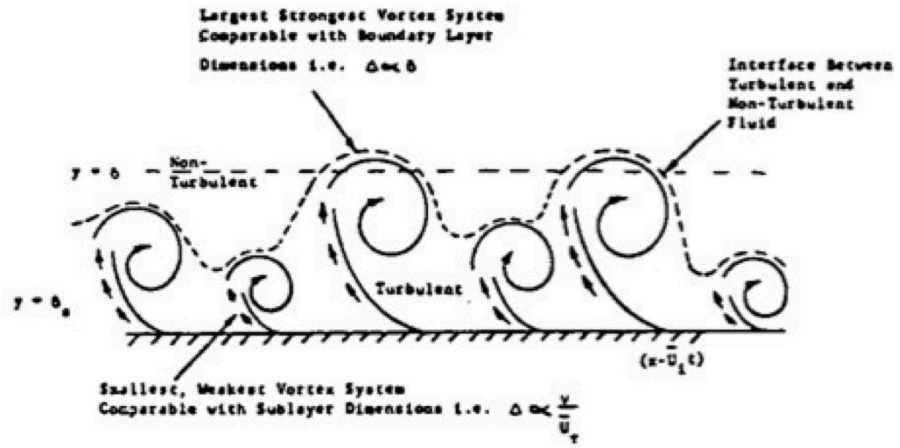

Fig. 2.13: Intermittency explained by random variation in strength of consecutive vortex systems. (Black, 1968)

Head and Bandyopadhyay (1981) were the first to provide actual experimental support for the numerous hairpin vortex models that were proposed, by publishing photographs of

smoke-filled turbulent boundary layers. The photographs showed loop-shaped forms at 45° to the wall. By studying a wide range of Reynolds numbers, from 500 to 17500, they were able to determine the effect of the Reynolds number on the shape of the vortices, as shown in figure 2.14: starting from a low number, the turbulent boundary layer is populated with

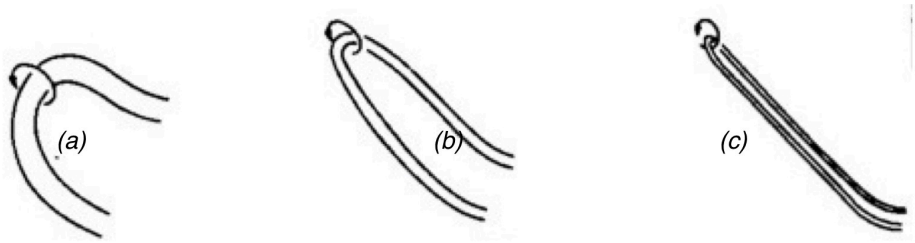

Fig. 2.14: Effect of Reynolds number on features composing an outer region of turbulent boundary layer. (a) very low Re (loops); (b) low-moderate Re (elongated loops or horseshoes); (c) moderate-high Re (elongated hairpins or vortex pairs). (Head and Bandyopadhyay, 1981)

arch-shaped forms, which in turn become elongated loops at moderate numbers, and finally hairpins at moderate-high Reynolds numbers. However the smoke visualization technique, and the quality of the observations, still left the issue over quasi-streamwise vortices, the legs of the hairpin structure, unresolved. Later, large-eddy and direct simulations of turbulent channel flow were used by Moin and Kim (1985) to show, for the outer region of their simulated channel flow, that vorticity vectors lines were commonly found in horseshoe

shaped but asymmetrically. They reported that the horseshoe-shaped structures were the result of merging deformed vortex sheets, therefore they did not show elongated streamwise legs.

The truly first unified model was introduced by Robinson (1991) in which he explained that all what was observed in the past were various stages in time and space of the same structure. Each section of the boundary layer has a characteristic population of vortices: transverse vortices are found in the outer region, quasi-streamwise vortices are the majority in the buffer region, while the overlap region is a mix of the two shapes. Ejections and sweeps motions are related to vortical structures, playing an important role in the Reynolds

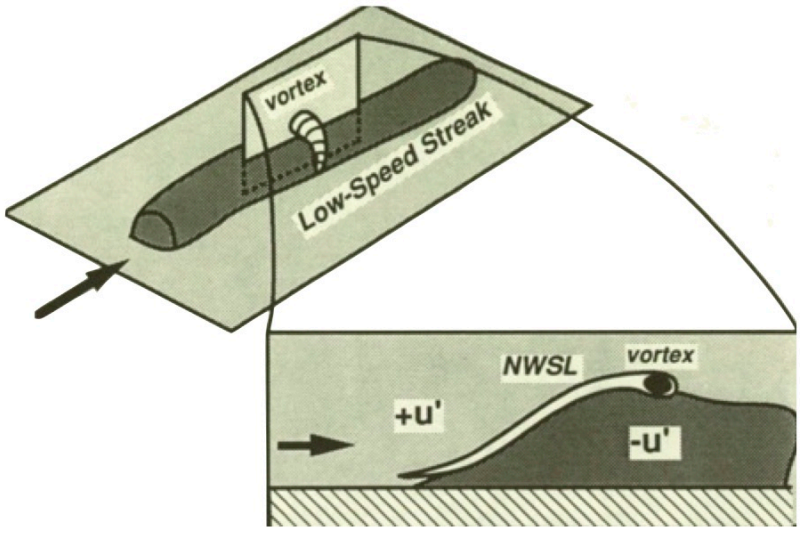

Fig. 2.15: Rollup of a near-wall shear layer formed at the interface between high and low-speed fluid. (Robinson, 1991)

shear stress and in maintaining turbulence mixing. At distances up to 30 viscous lengths from the wall, the vortices majorly responsible for turbulent production are the quasi-streamwise vortices, which are described as the central motion in boundary layer turbulence production. Quasi-streamwise vortices collect and lift low-speed near-wall fluid, while leaving a persistent low-speed streak; the low-speed fluid then encounters relatively high-speed fluid, creating a shear layer that will roll up into a new vortical arch, as depicted in figure 2.15. The arch will grow outwards by means of agglomeration and/or self-induction and circulation lift, repeating the cycle once again. The second way turbulence may be produced is by means of a descending neck from a mature vertical arch into low-momentum near-wall fluid. In this way the vertical neck is rapidly stretched into an elongated vortex leg, eventually dissipating or breaking off. The endorsement of the hairpin vortex model came later, with Adrian (2000) which formally introduced the concept: at the wall a low-momentum fluid, generated by several circumstances, erupts upwards, forming the primary hairpin vortex. Once in the buffer region, the hairpin is stretched and intensified by different values of the

streamwise velocity between its extremes. It grows in time, from a hairpin to an omega and depending on its strength, it can generate another upstream hairpin, by inducing a strong, three-dimensional second-quadrant motion that interacts with high-speed fluid behind the primary hairpin. The second hairpin then may also generate another vortex. The heads of the various hairpins can be connected with an imaginary line that has a certain slope depending on the rate of continuous vertically and spanwise growth, the hairpin's streamwise convection velocity, and the relatively uniform time between the formation of successive hairpins. This hairpin cascade formation concept was also discovered by Zhou et al. (1999): the signature in the velocity fields in the streamwise and spanwise directions is depicted in figure 2.16. Experimentally, Liu and Adrian (1998) found that symmetry of the hairpins packet is highly influenced by the symmetry of the low-momentum fluid generating it, however this does not hinder the ability of calculating the slope of the heads. It can be considered, in facts, that that packets grow linearly, although each at different rates for the purpose of an idealized model. The distances between a hairpin and the other in the packet

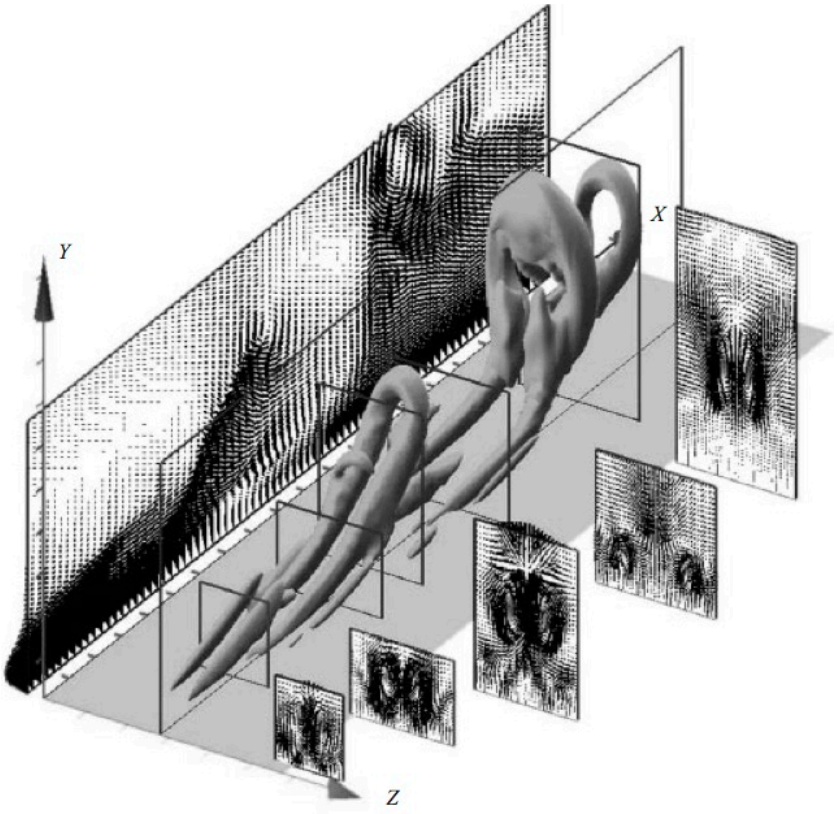

Fig. 2.16: Hairpin vortices computed from the velocity vector field in the plane lying midway between the legs. (Zhou et al., 1999)

ranges between 100 to 200 viscous lengths in the streamwise direction, while legs are about 50 viscous lengths apart. Such close spacing is indicative on how densely populated the near-wall region is with young hairpins, but small hairpins can be found at the upper edge of the boundary layer; in this case the explanation is that they can form even at a distance from the wall. When the packet grows, the larger hairpins move downstream at a faster rate than the smaller and younger hairpins, because the back-induced velocity decreases as the

size increase, but also because the background could be faster the further it is from the wall. The bulges found at the edge of

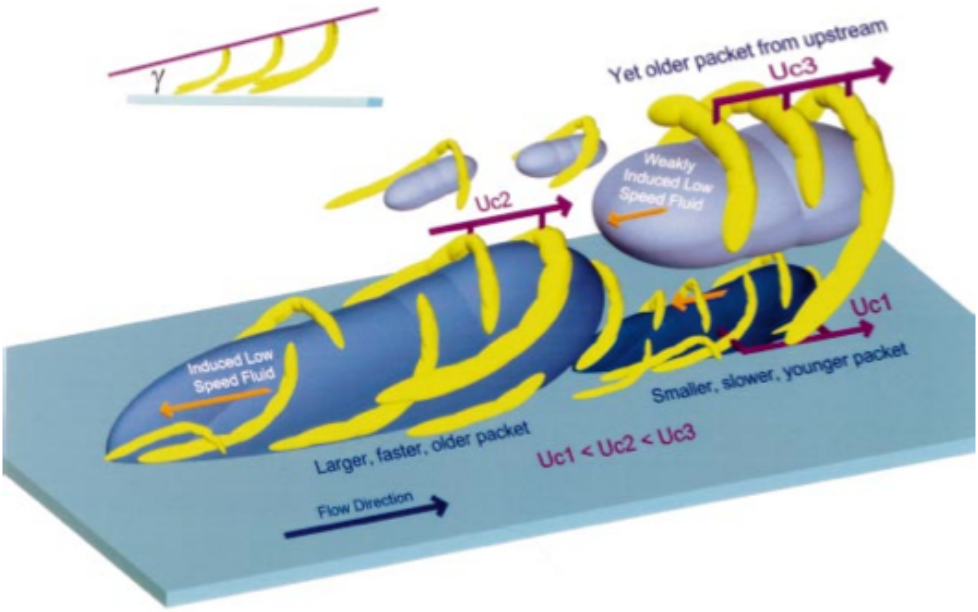

Fig. 2.17: Conceptual scenario of nested packets of hairpins or cane-type vortices growing up from the wall. They align in the streamwise direction creating large zones of nearly uniform streamwise momentum. Smaller packets move more slowly since the large- scale motions induce faster upstream propagation. (Adrian, 2000)

the boundary layer are no other that packets of hairpins that grow until they reach that region. All is summarized in figures 2.17 and 2.18 taken from Adrian (2000): hairpins cores are colored in yellow, while the low-momentum fluid that sustain the formation of hairpins is cooked in shades of blue or brown, respectively. Particularly from figure 2.18, can be depicted three main packets containing several asymmetric hairpins vortices. The cores, as they grow, gets further away from the

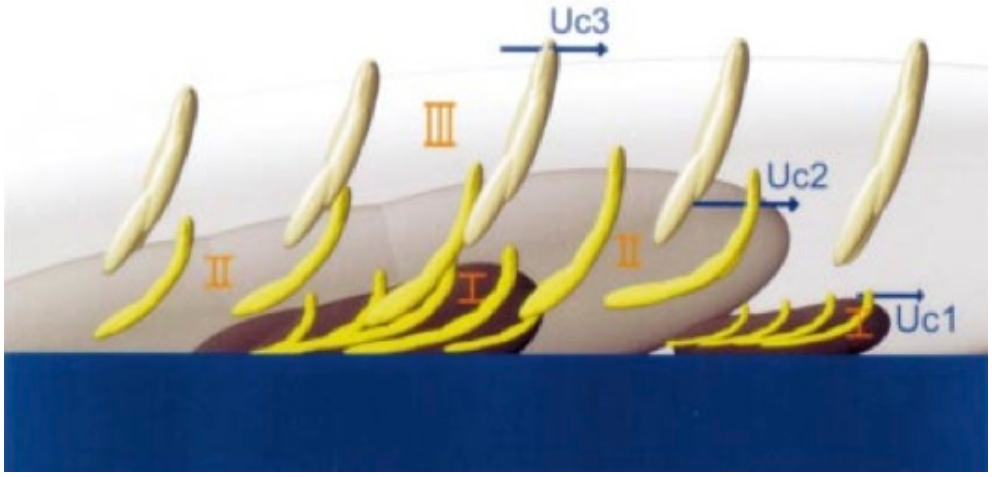

Fig. 2.18: Idealized model of hairpin packets nesting within larger hairpin packets, and traveling at different velocities. The nested hierarchy creates multiple uniform momentum zones, and a lower velocity as one approaches the wall. (Adrian, 2000)

wall, while the large packets have larger hairpins, a sign of faster convection velocity in the streamwise direction. The smaller the packet is the stronger the back induced flow becomes, therefore the smaller end of a packet has a greater back induction than the larger end. As it shown, for small scales the hairpins do not appear aligned, and waviness in the low-speed streaks in the buffer layer leads to think that hairpins could be shifted laterally by as much as the spanwise width of the hairpin itself, for lengths of several hairpins. Nonetheless, if longer distances are considered, hairpins are somewhat uniformly aligned, corresponding to a coherence between the hairpins in packet: this means that an organized pattern of

hairpins does exist. Packets can also grow inside the uniform momentum zone of an older packet, with very small velocity differences, putting less strain on the newly formed hairpins packet.

This model, although simple and that doesn't cover the interactions between hairpin packets, which can only be speculated at this point but could reasonably be of various stages of interactions, well explains the many aspects of structure in the turbulent boundary layer, shedding light on what past researchers have missed. For example: the different structure populations of the turbulent boundary layer proposed by Robinson (1991) is consistent with the hairpin vortex model in the way that each region of the turbulent boundary layer hosts different stages of the hairpin packets. The buffer layer hosts quasi-streamwise vortex legs of the adult hairpins; the logarithmic layer is the main location of the inclined necks and heads of the hairpins, while in the outer layer only the biggest heads of the oldest hairpins can be found. Backs of bulges are the result of the merging of few hairpins at the end of their life. Another example is given by how well the hairpin packet scenario supports Townsend's (1976) attached eddy

hypothesis. His hypothesis states that eddies attached to the wall grow proportionally to the distance from the wall in a self-similar way, just like hairpins mostly do. If low-pass filters are applied so that only cores of the hairpin vortices are considered, what is left of the flow pattern of a packet fully satisfies Townsend's hypothesis.

Chapter 3 - Development and characteristics of riblets

As mentioned earlier, alongside the research into the characterization of the turbulent boundary layer, academic has looked also on ways to harness the coherent structures of the turbulent boundary layer to improve the way we interact with it in all the possible settings, hopefully in a more systematic approach than by chance of seeing a rough tennis ball behaving better after being hit. This chapter will take a look on how riblets technology has become the most promising way to take advantage of the turbulence and how it can drastically improve our everyday world.

3.1 On the development of riblets

Soon after the characterization of the coherent structures in the turbulent boundary layer, a lot of studies were started in the quest of manipulating or managing the turbulent flow to find a way to passively reduce drag generated by those structures. As a pioneer in this research field, Walsh M. J. at NASA Langley research center studied extensively riblets, obtaining drag reductions to 8% and that the best height for the riblets is in the order of the viscous sublayer thickness (Walsh and Lindeman, 1984). Meanwhile in Germany, a group of researchers led by Bechert, began their investigation on fast shark skins, inspired by the observations of Reif and Dinkelacker (1982). They noted that scales of fast sharks, as seen in figure 3.1, are small, at about ⅓ of one millimeter, while the lateral distance between the ridges on top of the scales reaches about 1/20 of one millimeter. At the end of the 1980's riblets studies were so intensive that Choi (1989) even states that "the concept of using a riblet surface, i.e. a surface with longitudinal micro-grooves, to obtain a skin-friction drag

reduction by modifying the coherent structures of the turbulent boundary layer […] is now very close to industrial application". There have been some industrial applications in the past 30 years, but so far no airline company has fitted its whole fleet with riblets. Perhaps the way of living of those years was extremely shocked by the fuel crisis of early 1970's that research was also focus on ways to reduce the cost of fuel. Today it is not much the cost of fuel in monetary terms, instead its cost on the environment that could introduce on a large scale passive ways of drag reduction.

3.1.1 Being inspired by nature

As the earlier research led by Walsh found and confirmed that surfaces with grooves can reduce the drag experienced by the wall, some researchers started to look at nature for what structures could be more effective in passively reducing drag. After all, the laminar flow in nature is not really common: instead there are many examples of turbulent flows, from blood inside living beings to atmospheric flows. Additionally, studying

turbulence on different type of flows helps better understanding the mechanisms behind the phenomenon, getting insights that otherwise could be missed.

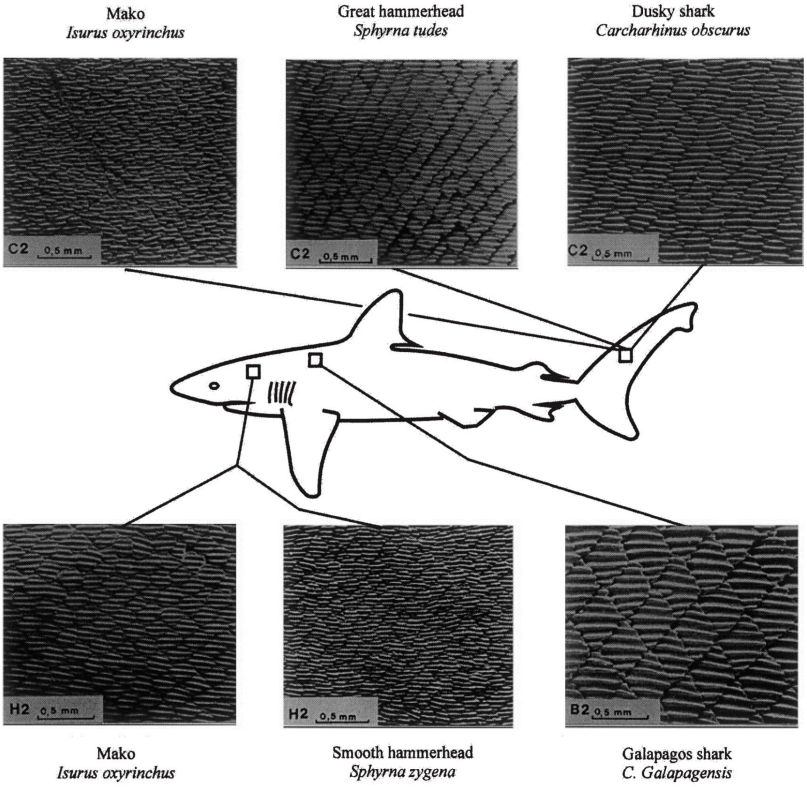

Fig. 3.1: Scale patterns, and their locations on, of some fast species of sharks. (Reif, 1985)

Bechert, since the mid-80's and until his death, produced several studies on riblets designs based on the skins of fast sharks, some of which were initially photographed by Reif (1985) and visible in figure 3.1. Fast sharks as the Mako, Isurus oxyrinchus, swim at high Reynolds numbers in the order of millions, so the flow around them is definitely turbulent and to achieve speeds of 74 km/h, mother nature have given them

three-dimensional scales that are wonders of engineering. Other species of sharks taken into consideration were the Great Hammerhead (Sphyrna tudes), the Smooth Hammerhead (Sphyrna zygena), the Dusky shark (Carcharhinus Obscurus) and the Galapagos Shark (Carcharhinus Galapagensis). Although each has different scale shapes and dimensions, the individual scale usually has prominent ridges, from a single one to up to seven and they interlock between them, resembling a chain armor of medieval times, under the microscope. Figure 3.2 gives a closer look on the body scales of other species of sharks, and it is noticeable the interlocking pattern.

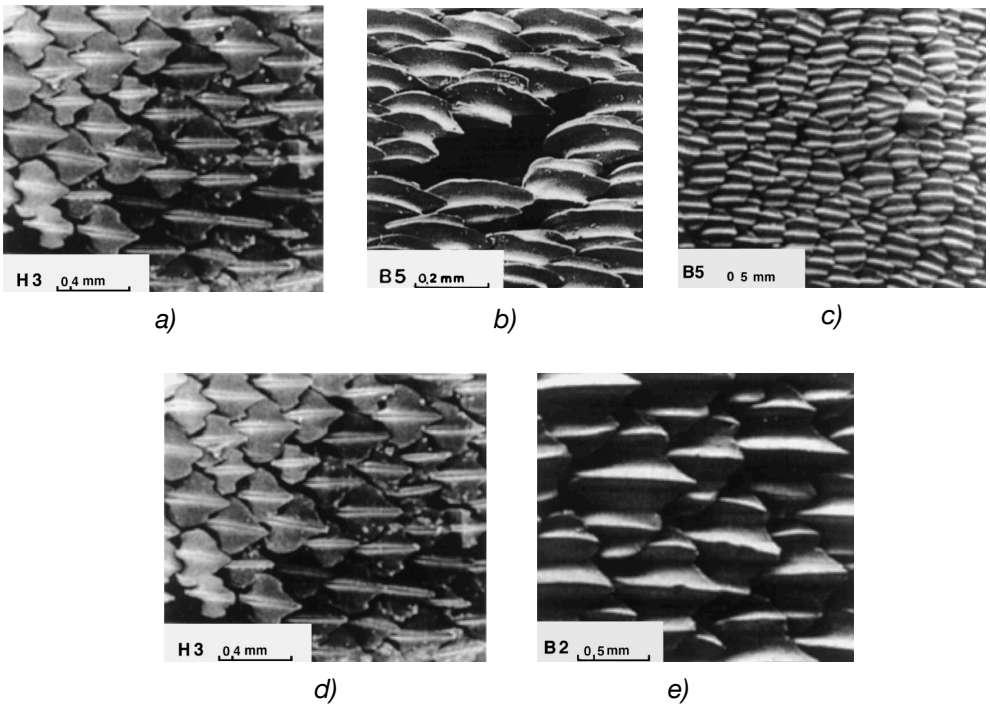

Fig. 3.2: Close up of cale patterns, and their locations on, of some fast species of sharks; a) dogfish (squalidae family); b) great white shark (carcharodon carcharias); c) sandbar shark (carcharhinus plumbeus); d) spiny dogfish (squalus acanthias); e) tiger shark (galeocerdo cuvier) . (Reif, 1985)

Experiments with sharks were not a recent thing: Johnson, quoted by Walsh (1990), towed a dead brown-shark (Carcharhinus plumbeus), finding a drag coefficient somewhat higher than that of a dolphin. Obviously carrying out experiments with a dead shark would not give the same reaction a living shark would have. Petersohn (1959) and Gren (1987) experimented with the spiny dogfish (squalus acanthias): not a really fast one and Bechert and Hage (2006) think it was chosen because of its high availability in the North Sea. While the former found that tubes that had been lined with preserved sharkskin had a higher pressure loss compared to the smooth tubes, the latter was inspired by that species of shark to build a plastic magnified replica of the scales, although his results were also unsatisfactory since no drag reductions was found. Also Bechert et al. (1985) carried out their own experiments on sharkskins, but the results were not satisfactory either. That happened because, as Bechert and Hage (2006) - posthumous article since Bechert died in 2004 - recognized that, flow conditions in a typical wind tunnel would require rib spacings of less than 0.5mm: technology was not ready for such dimensions, yet. So research advanced when Bechert had

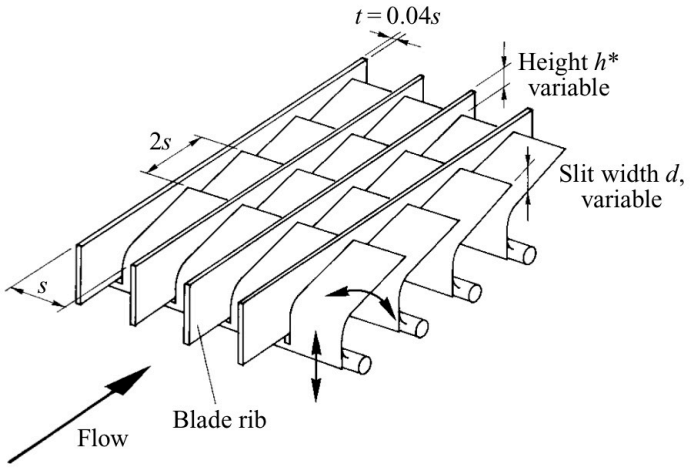

Fig. 3.3: Schematic of the ribs and slits mechanism used on the test plate. (Bechert et al., 1997)

access to the Berlin oil channel: flow conditions would require spacings ten times greater, so much easier to manufacture, and also the possibility to move the scales. With the oil channel, Bechert studied different configurations of test plates. First Bechert et al. (1997) studied a test plate having longitudinal blade ribs, figure 3.3 of initial thickness being 4%

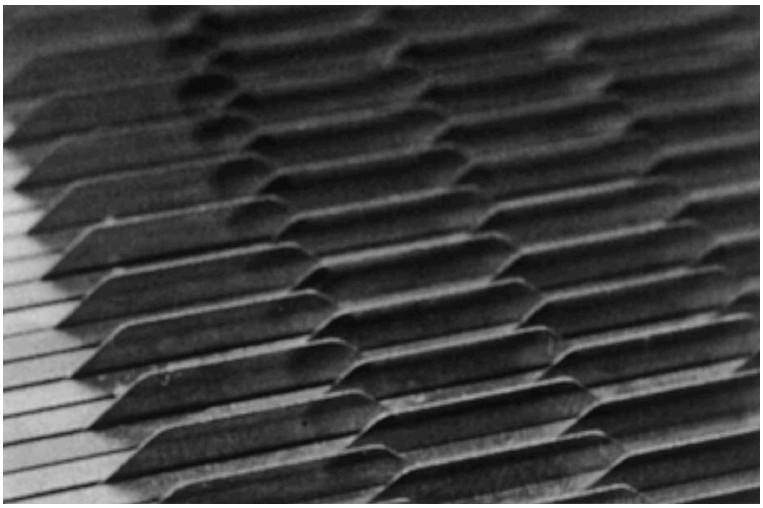

Fig. 3.4: Photograph of the staggered adjustable fins. (Bechert and Hage, 2000).

of the spacing (although they later used thinner blade ribs) in order to investigate the drag reduction by the mechanism of slit ejection. Then, Bechert and Hage (2000) studied a test plate, seen in figure 3.4, made with staggered alternating fins. On this test plate they were able to change the length of the fins to investigate the optimal length. Finally figures 3.5 a) and b), being an exact replica of the shape and behavior of the

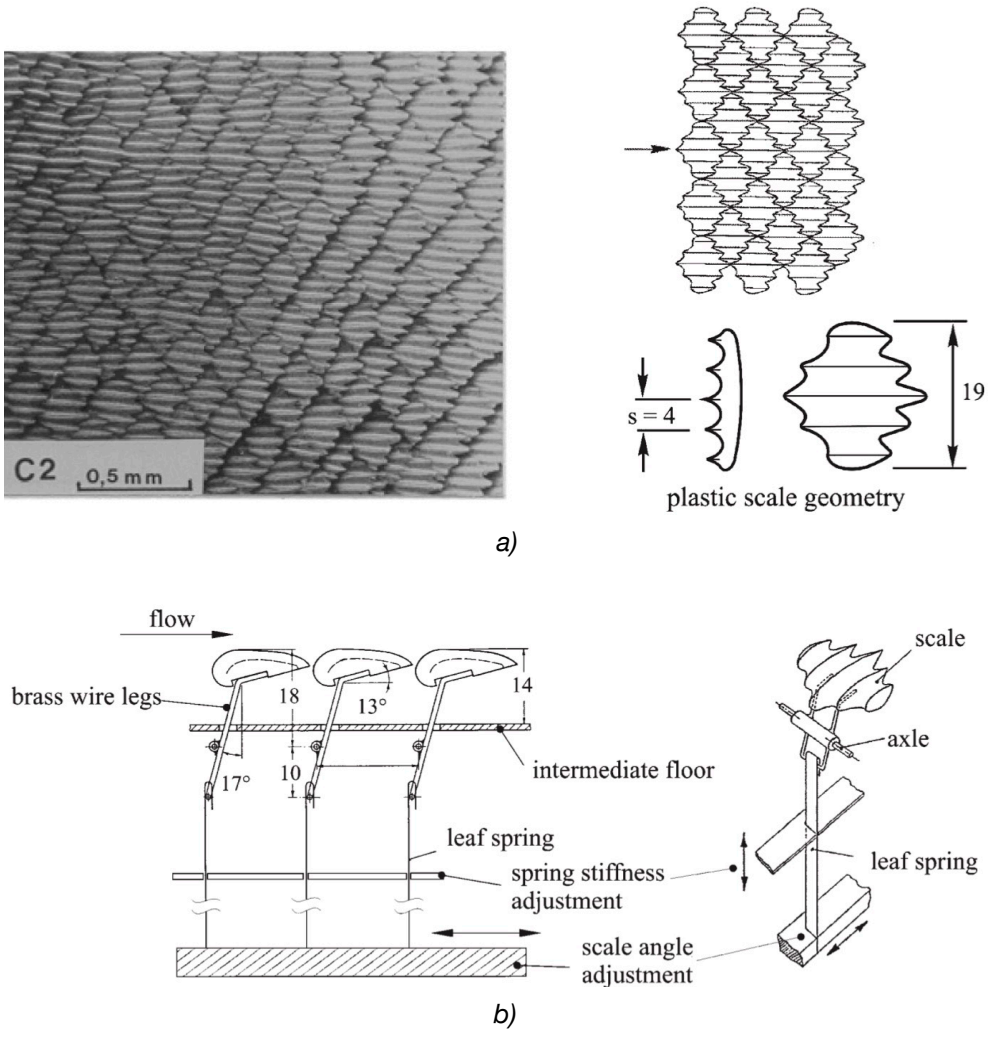

Fig. 3.5: Diagram of the scale replica and its control mechanism. Dimensions are in [mm]. (Bechert and Hage, 2006)

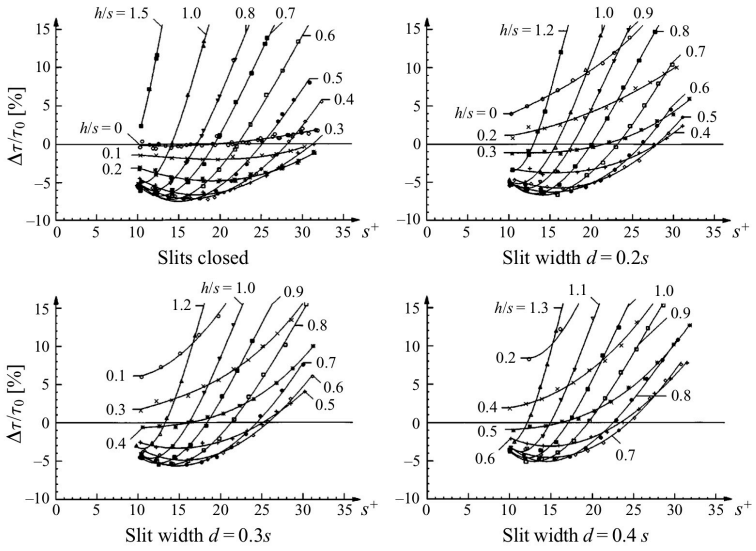

Fig. 3.6: Shear stress reduction graphs obtained with various configurations. (Bechert et al., 1997)

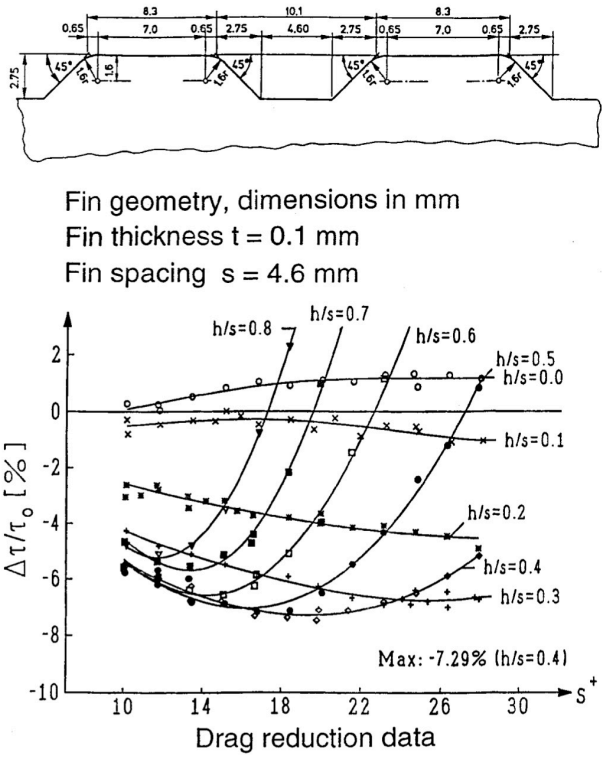

Fig. 3.7: Drag reduction results and relative fin geometry used. (Bechert and Hage, 2000)

hammerhead shark skin, although it took them a lifetime of research. Regarding the results, Bechert et al. (1997) obtained

drag reductions of 7.6% when the slits are completely closed as shown in figure 3.6, Bechert and Hage (2000) reported that all the various configurations of lengths gave performances inferior to traditional bidimensional blade riblets, with the best drag reduction of 7.3%, compared to a flat plate, with spacings of s+=19 and a height equal to 40% the spacing and length of fins twice the spacing, as seen in figure 3.7. Still not exactly great result compared to values of drag reductions of 9% on 2-D blade riblets. Bechert and Hage (2006), using an exact replica of shark skin, reported a drag reduction of just 3.1% when the scales were rigid and aligned to the flow, otherwise there was an actual increase on the drag, as it is all depicted in figure 3.8. Later on, however, Zhang et al. (2011), replicated the

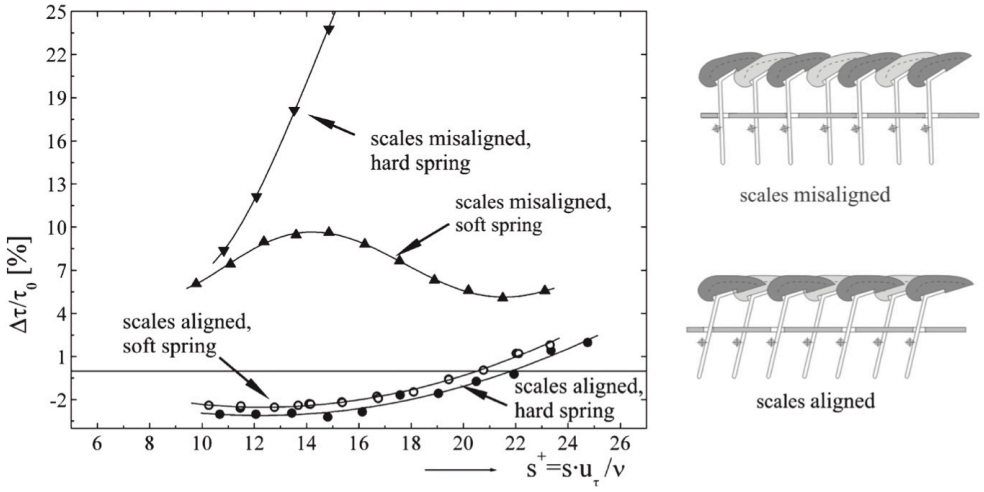

Fig. 3.8. Data on drag reduction and configurations of the hammerhead shark scale replica. (Bechert and Hage, 2006)

experiment of Petersohn (1959), finding a drag reduction of up to 12%.

Obviously the interest in looking for example in nature was not limited to just sharks. As the technology improved, other specimen were considered for research of better ways to reduce drag. An example is given by Chen et al. (2014). His research team, inspired by Bechert's efforts, had the idea to look at bird flight feathers and their characteristic herringbone structure. Depicted in figure 3.9, the feathers have a central

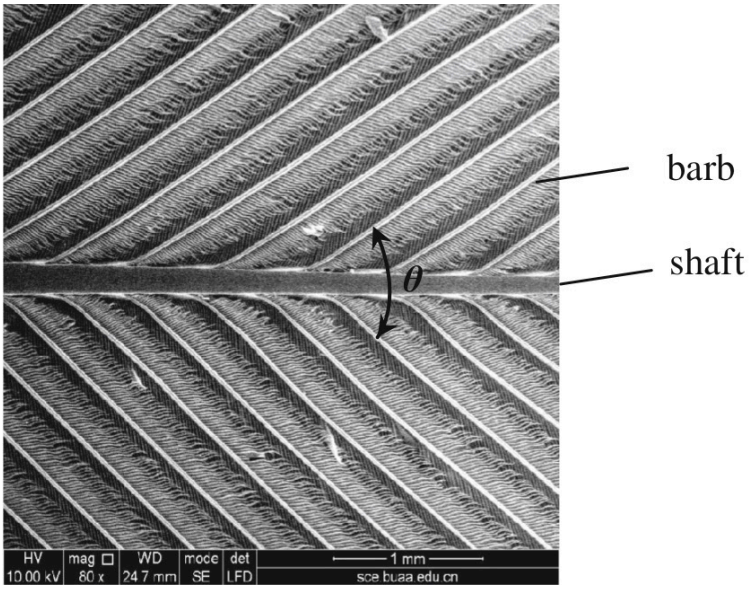

Fig. 3.9: Microscopic photograph of the structure of bird flight feathers. (Chen et al., 2014)

hollow shaft from which spread thinner branches, called barbules, at a given angle measured as shown in figure 3.9, each having thinner and finer hair, called barbs. They

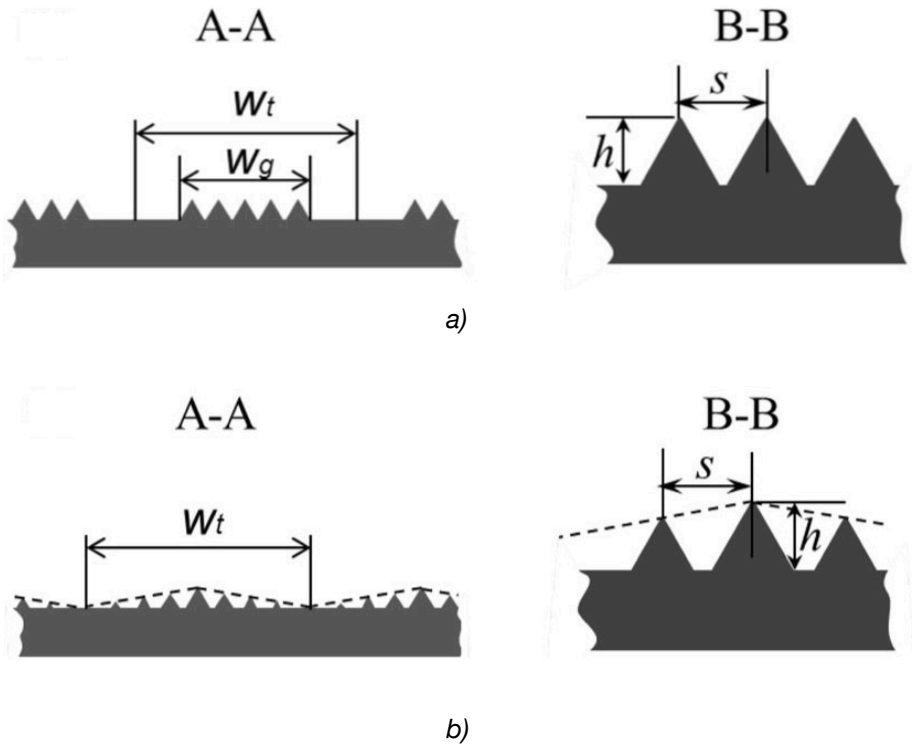

Figgs. 3.10.a and 3.10.b: Sections of the spatial three-dimensional herringbone riblet. (Chen et al., 2014)

transposed the concept to plane, three-dimensional herringbone riblets, diagram of which is in figure 3.10.a, and spacial, three-dimensional herringbone riblets, shown in figure 3.10.b. Where the sections are taken from and their position in relation to the flow, are shown in figure 3.11. Chen et al. (2014) experimented with the angle of the ridges in relation to the flow, where an angle of θ=0° corresponds to conventional riblets aligned with the flow. The results of this investigation are shown in figure 3.12: as one could have assumed, when the angle increases from θ=0° to θ=60°, also the drag reduction

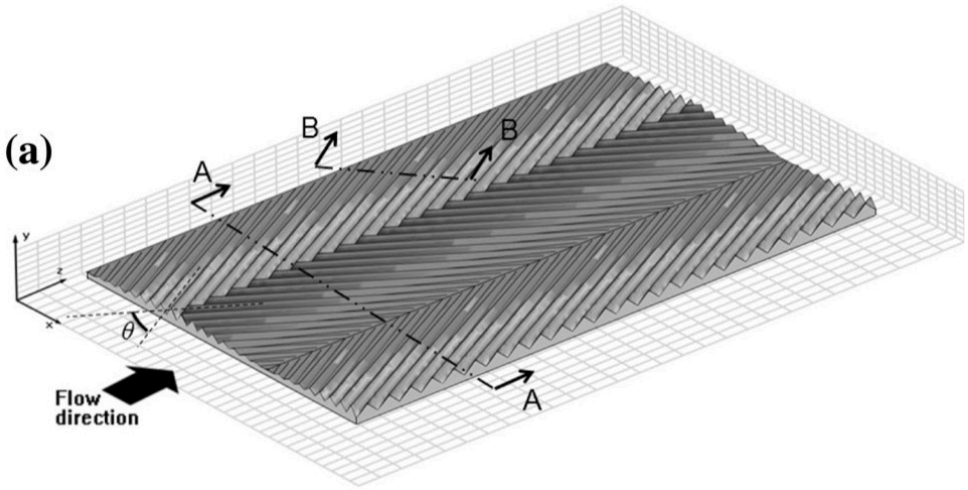

Fig. 3.11: Schematic of test plate equipped with bio-inspired herringbone riblets and flow direction. (Chen et al., 2014)

effects increase. At θ=60°, a drag reduction of 17% is reported, which is astoundingly good. However when the angle increases at θ=90°, that corresponds to riblets being perpendicular to the flow, and θ=120°, the drag reduction effects diminish or even disappear. Comparing the plane vs. the spacial three-dimensional riblets, Chen et al. (2014) obtained an even better

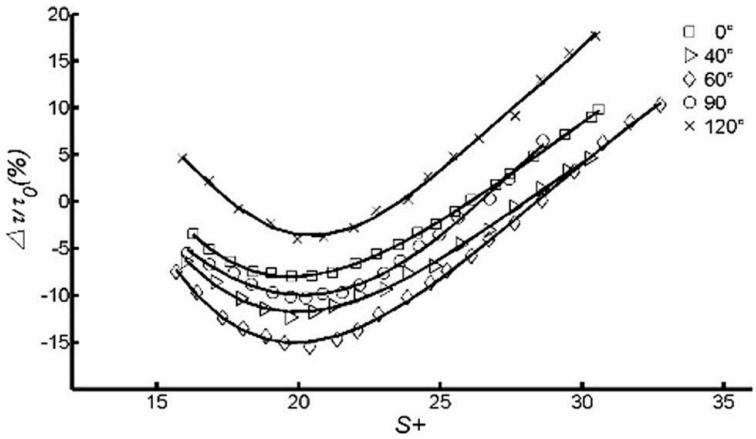

Fig 3.12: Effect of angle theta on drag reduction capability. (Chen et al., 2014)

result, as shown in figure 3.13. The spacial three-dimensional herringbone riblets were able to reduce drag by as much as 21%, compared to a flat plate. Almost three times their result on common flow-aligned riblets.

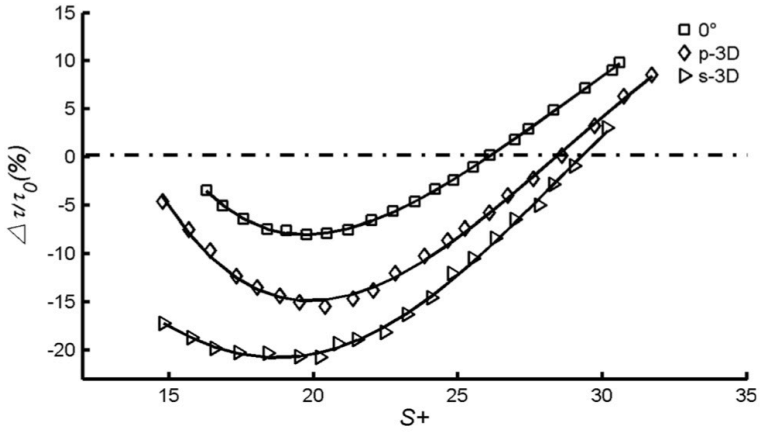

Fig 3.13: Drag reduction results of bio-inspired plane and spacial herringbone riblets. (Chen et al., 2014)

3.1.2 Sinusoidal riblets

Since traditional riblet design has a relatively low drag reduction rate, the quest for better performing designs, that are still easy to manufacture and to maintain, brought to attention the sinusoidal riblets. Compared to the original design, the new design, also part of this research project, makes the riblets in a wavy pattern along the streamwise direction as depicted in

figure 3.14 from Peet et al. (2008), where only the ridges are considered for an easy visualization.

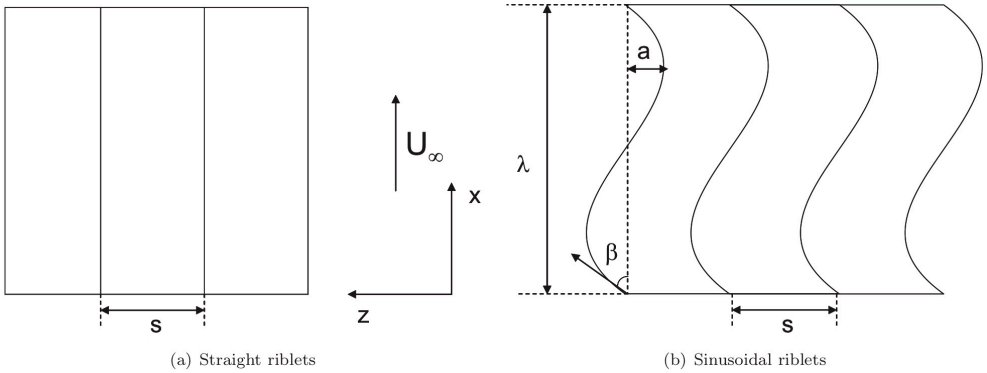

Fig 3.14: Comparison diagram between a) straight and b) sinusoidal riblets showing the main parameters for each. (Peet et al., 2008)

To better define the sinusoidal riblets, new parameters need to be introduced, such as the wavelength λ and the amplitude a, which together give the deviation of the spanwise coordinate from the corresponding coordinate of the straight riblet, using the formula

$$z'(x) = a\sin\left(\frac{2\pi}{\lambda}x\right)$$

Peet et al. (2008) scaled the wavelength by half the distance between the midpoint between the tip and valley on a riblet wall and a flat wall, corresponding to the half-width of the plane channel with the same cross-sectional area, focusing their research on two different ratios

$$\lambda/\delta = \begin{cases} 3.22 \\ 6 \end{cases}$$

By means of a large eddy simulation, the group consistently observed no drag reduction for the smaller wavelength, while a 7.4% drag reduction was obtained for the larger wavelength.

Kramer et al. (2010) performed several tests by varying the amplitude of the wave, but they did not find an appreciable drag reduction effect, especially larger amplitudes even increase drag.

Sasamori et al. (2014) however observed a good drag reduction of up to 11.7%. His team focused on the dependance of the drag reduction of sinusoidal riblets as a function of bulk Reynolds number. They found that the peak of the drag reduction effect for their riblets was at a Reynolds number of about 3400, as shown in figure 3.15 compared to

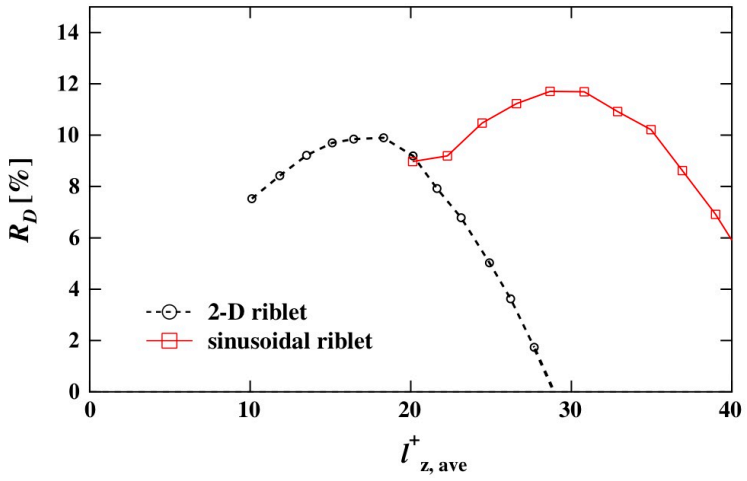

Fig. 3.15: Relationship of the drag reduction rate as a function of the lateral spacing. Optimal 2D riblet: black circles and dashed line (from Bechert et al., 1997); sinusoidal riblets: red squares and solid line. (Sasamori et al., 2014)

the optimized two-dimensional riblets of Bechert et al. (1997). Another graph comparing the two design is reported in figure 3.15: this time the drag reduction rate is plotted as a function of the lateral spacing. It can be noted how the sinusoidal design is most efficient with a lateral spacing of about double that of conventional riblets. The latter become less effective at a spacing the same size of the near-wall quasi-streamwise vortices. The sinusoidal riblets, instead, become most effective when their spacing is larger than the diameter of streamwise vortices.

3.2 How riblets work

Even if turbulence is not fully understood, hence neither the mechanism that enables riblets to effectively reduce drag, during the decades of research there have been some valid insight on what might actually happen.

Choi (1989) in an effort to investigate the near-wall region, compared the turbulence production on a flat wall and over

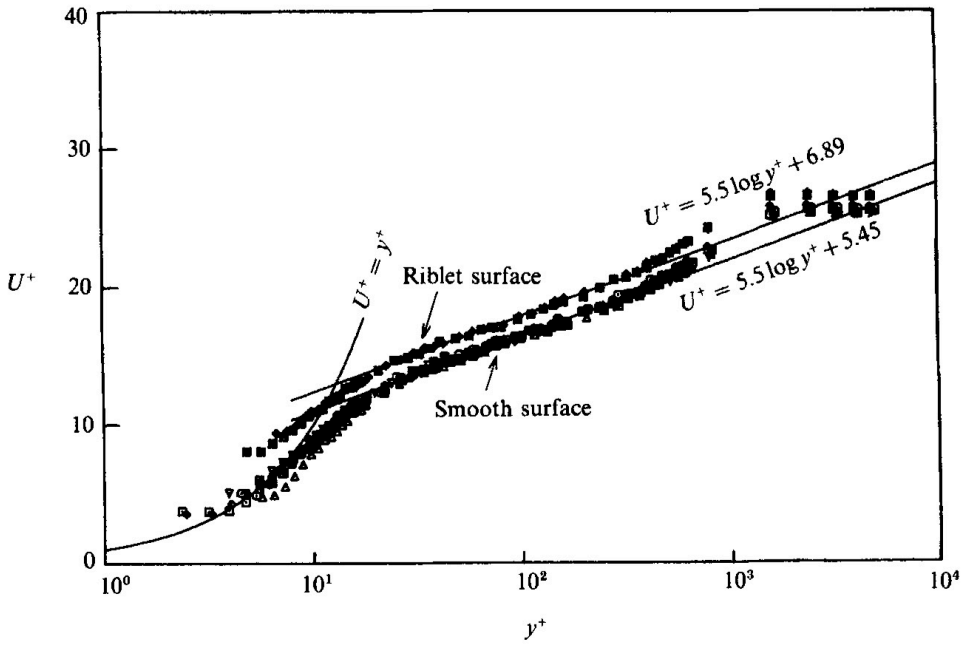

Fig. 3.16: Comparison of the mean velocity profile between the smooth and the riblet surfaces. (Choi, 1989)

riblets.

He reported several observations comparing the two flows. In figure 3.16 is depicted the comparison between the two mean velocity profiles. The one measured with the riblet surface shows an upward shift, leading Choi to suggest an increase of the viscous sublayer thickness corresponding to a decrease of turbulence intensity of about 10%. A reduction on the fluctuating component of wall skin friction, visible in figure 3.17, was measured: it was bound to a period of quiescence

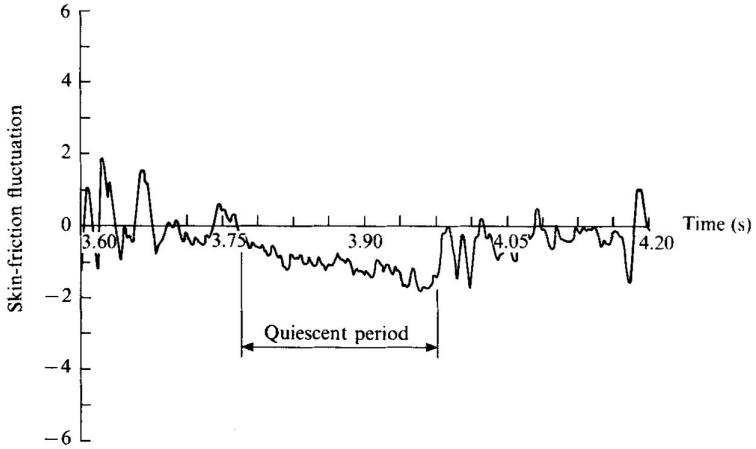

Fig. 3.17: Record of wall skin friction fluctuations in which the quiescent period is marked. (Choi, 1989)

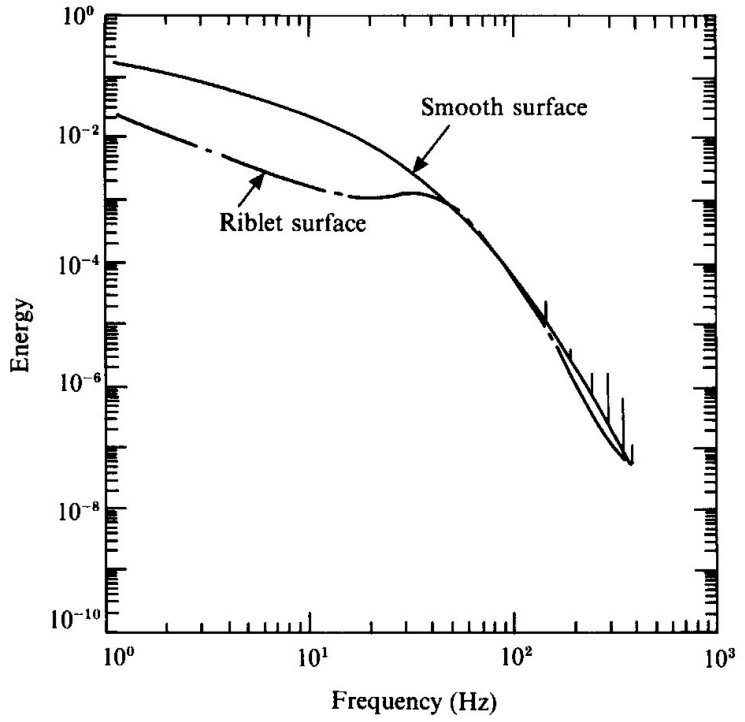

Fig. 3.18: Spectra of wall skin friction fluctuations for the smooth (solid line) and riblet (solid/dash line) surfaces. (Choi, 1989)

due to the partial laminarization of the viscous sublayer, at the bottom of the riblets. With the extraction of the energy spectrum, this reduction mainly involved frequencies below 20Hz, figure 3.18. Another smaller reduction was observed for

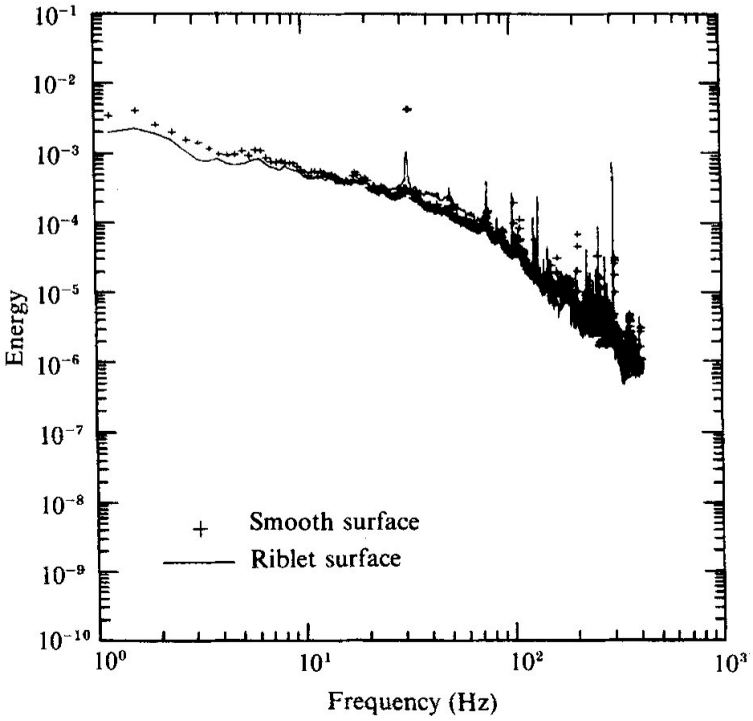

Fig. 3.19: Spectra of wall-pressure fluctuations on smooth (+) and riblet (solid line) surfaces. (Choi, 1989)

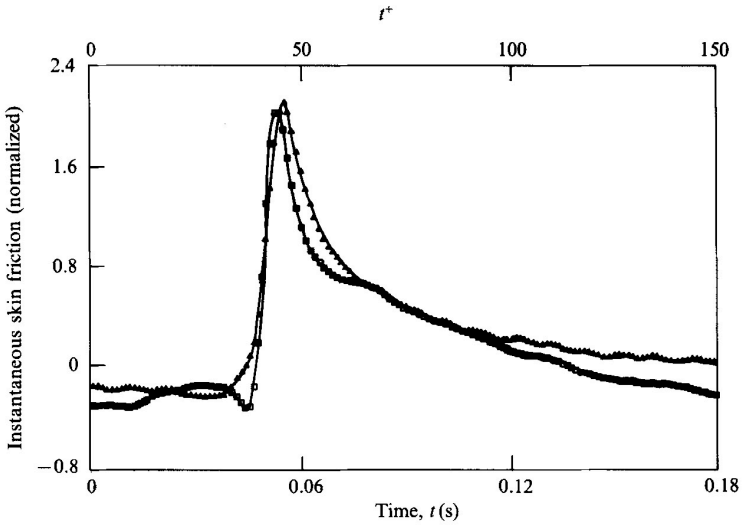

Fig. 3.20: Conditionally sampled burst signature for the smooth (triangles) and riblets (squares) surfaces. (Choi, 1985)

the wall pressure fluctuation spectra, seen in figure 3.19, and also involving the lower frequencies. Such reductions of fluctuations also indicate a lower flow noise. Another significant

result was found regarding the bursting event: when the surface is covered with riblet, the bursting appears to be halved in duration, figure 3.20, with an increase of up to eight times of the burst frequency, that can be observed in the up-leftward translation of the probability density ruction of the wall-skin-friction signal in figure 3.21. Although hairpin legs,

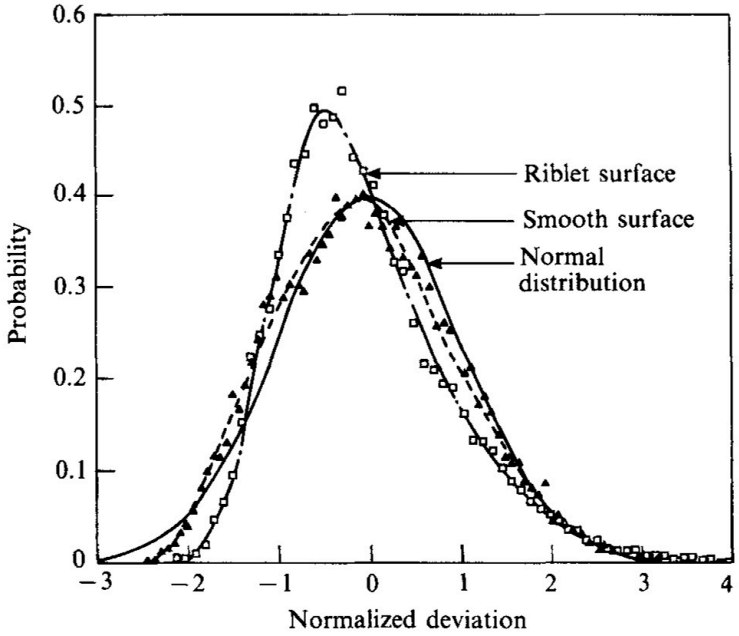

Fig. 3.21: Comparison of probability density of the wall skin friction signal over smooth (dashed line - triangles), and riblet (solid/dot line - squares) and a normal distribution (solid line). (Choi, 1989)

formed by the interaction of the bursting events with the longitudinal vortices, were similar in both cases, Choi (1989) noted that over the riblets the counter-rotating vortices were less wavy. During the bursting event, the conditionally sampled vertical velocity field showed that the flow direction was

negative, indicating a movement toward the wall, instead of away from it. The spanwise dimension of the negative vertical velocity field was twice in the riblet case, consistent with the observation of the flow, in which it was noted that the spanwise spacing between the pairs of longitudinal vortices over the riblets was around two times as wide as that of the smooth wall. As for the possible mechanisms behind the turbulent drag reduction observed with the use of riblets, Choi (1989) proposed that the presence of the riblets restrict the spanwise movement of the longitudinal vortices, which results in an early and rather weak near-wall burst, thus scaling down the turbulence production process by limiting the main event. This is based on the observation that the best spacing for riblets coincides roughly to the dimension of the gap between the longitudinal vortices.

Bechert and Hage (2006) and Bechert et al. (1997) proposed a mechanism on how riblets actually reduce drag. They reasoned that the strong exchange of momentum in a turbulent boundary layer, main cause for the production of drag, is due to the sweeps and the ejections appearing in the viscous sublayer. The former are high-speed lumps of fluid that move

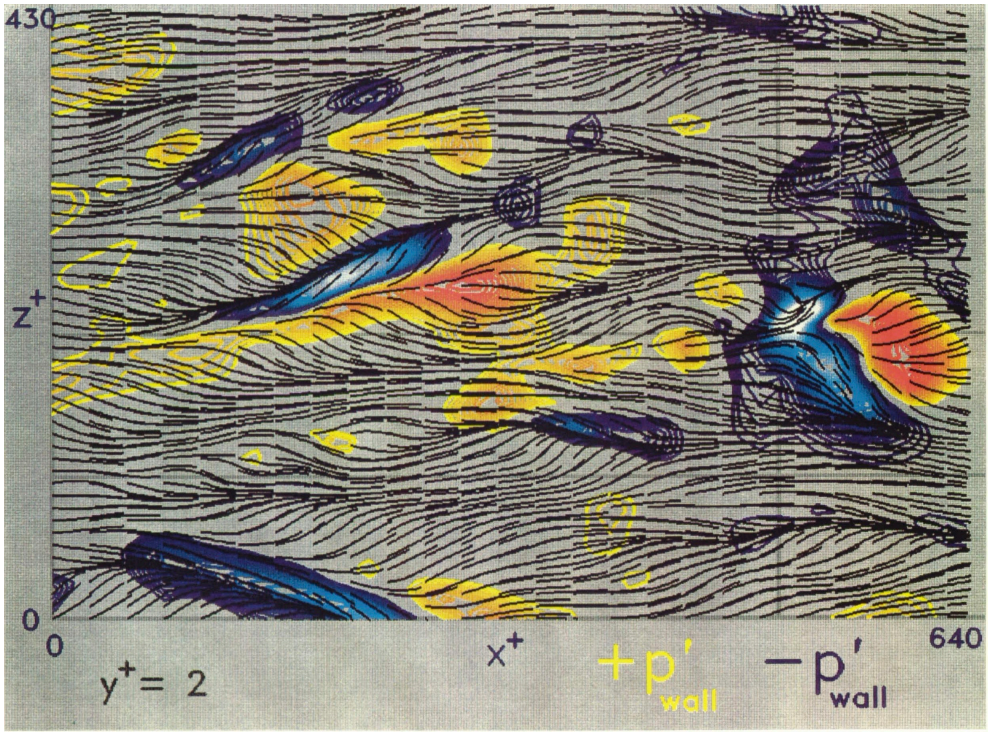

Fig. 3.22: Instantaneous streamlines taken at y+=2 underlaid with contours of wall-pressure. Yellow to red: p+=+3.0 to +25.0; blue to white: p+=-3.0 to -25.0. (Robinson, 1991)

toward the wall, visible in figure 3.22 from Robinson (1991) in yellow to red colors, due to the high pressure, while the latter motion is low-speed fluid that corresponds to low pressure areas, visible in blue to white colors in figure 3.22. This perpendicular motion in reference to the wall generates the shear stress, since the high-speed fluid is decelerated and the low-speed fluid is ejected abruptly. The riblets play their role in the fact that sweeps and ejections need fluid moving in the spanwise direction: the presence of the tiny ridges blocks, or at least greatly reduce the momentum transfer across the z-axis,

in reference to figure 3.22, hence the spanwise velocity are reduced which in turn reduce the skin friction. The major influencing factor in the spanwise flow hampering is the difference of height between the streamwise and the spanwise flows origins, depicted in figure 3.23. Luchini et al. (1991)

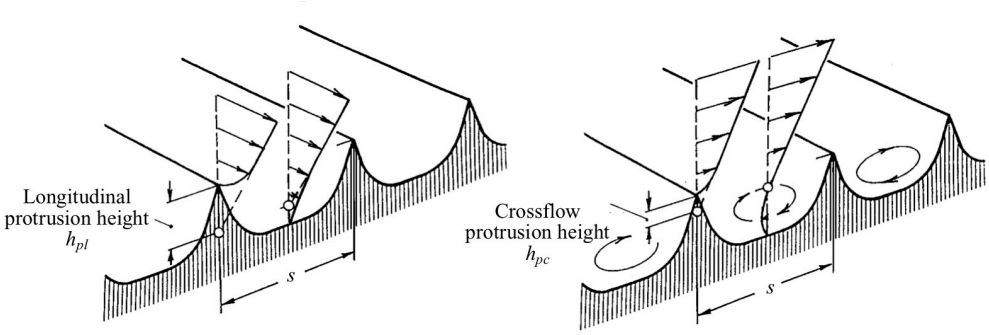

Fig. 3.23: Streamwise and spanwise flows origins. (Bechert et al., 1997)

calculated that the maximum possible difference between the two origins is 13.2% the lateral rib spacing, at least for very sharp and thin ribs alternating deep grooves. The spanwise fluctuations are reduced due to the fact that spanwise flow origin is closer to the rib tip, increasing the shear stress of the spanwise flow. This result was also confirmed by numerical Navier-Stokes computations made by Choi et al. (1993) and experimentally by Weiss (1993). Since the origins difference is a constant fraction of the lateral rib spacing, given a certain geometry of the riblets, as the spacing increases, so the origins

difference does. This linear behavior is confirmed by Bechert et al. (1997) with the results shown in figure 3.24. In the so-called "viscous regime", a linear behavior can be noted up until a lateral non-dimensional spacing of about 10. Hence a possible slope can be calculated noting that the following relation applies

$$\frac{\Delta\tau}{\tau_0} \propto \frac{\Delta h}{s} s^+$$

Luchini (1992) proposed a way to better calculate the relationship between the lateral spacing and the decrease in drag reduction in the following formula

$$\frac{\Delta\tau}{\tau_0} = \frac{0.785}{2\left(c_f\right)^{-\frac{1}{2}} + 1.25} \cdot \frac{\Delta h}{s} s^+$$

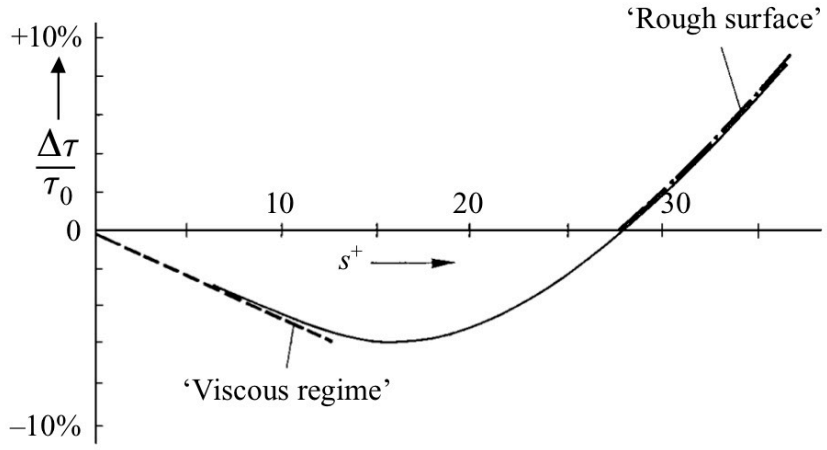

Fig. 3.24: Typical trend of a drag reduction curve. (Bechert et al., 1997)

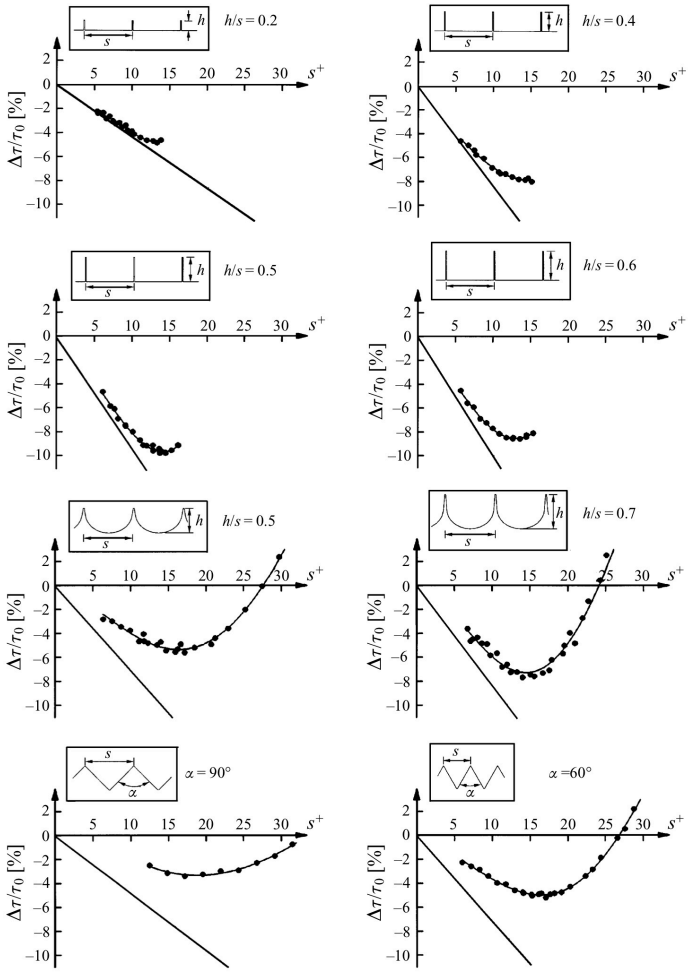

Fig. 3.25: Comparison graphs, for different designs, between the measured (dots) and the predicted drag reduction using Luchini's formula. (Luchini, 1992)

As it is shown in figure 3.25, the predicted slope for the blade riblets is not far off the data. The quality is so high because the finite thickness of the blades is taken into account. Instead for triangular or scalloped riblets, where the sharpness of the ribs has not been considered, Luchini's formula is over-estimating the slope.

Anyway the deviation that appears as the non-dimensional spacing increases, value that is strictly connected to the Reynolds number, is due to the fact that viscous flow assumptions cease to be valid. Bechert et al. (1997) supposed that an increase in wetted area, that means an increase in depth of the grooves, results in a change of behavior of the riblets, closer resembling a rough surface. The behavioral change is due to the fact that deeper grooves create pockets of fluid that begin to slosh between the riblets. This action increases the vertical velocity fluctuations directly impacting the Reynolds stress and therefore the drag. An optimal groove depth is given to a maximum ratio between the height and the lateral spacing of the riblets of 0.6, by Bechert et al. (1997).

Peet et al. (2008) ran Large Eddy Simulations of turbulent flow examining three different geometries of triangular cross-section riblets: straight, wavelength 3.22 times the half the distance between the midpoint between the tip and valley on a riblet wall and a flat wall, corresponding to the half-width of the plane channel with the same cross-sectional area, and wavelength of 6 times that distance. What Peet et al. (2008) found, regarding the mean streamwise vorticity and mean

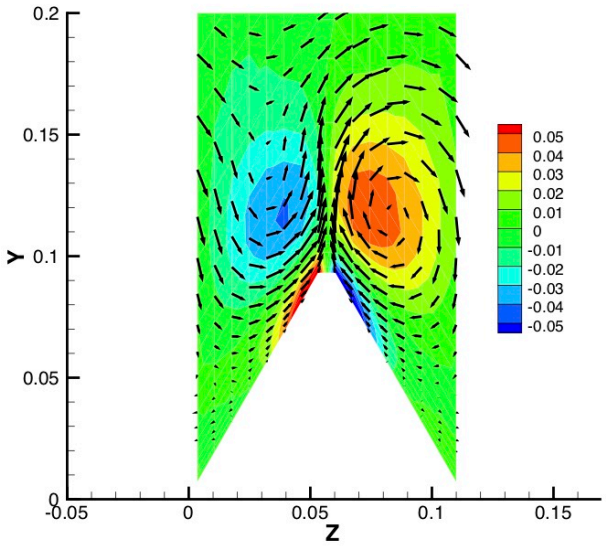

Fig. 3.26: Mean streamwise vorticity (colors) and mean velocity vectors at a transverse plane with straight riblets. (Peet et al., 2008)

velocity vectors is depicted in figures 3.26 and 3.27, where the spanwise flow is shown for the straight riblet and the sinusoidal riblets cases respectively. Furthermore, figure 3.27 shows also

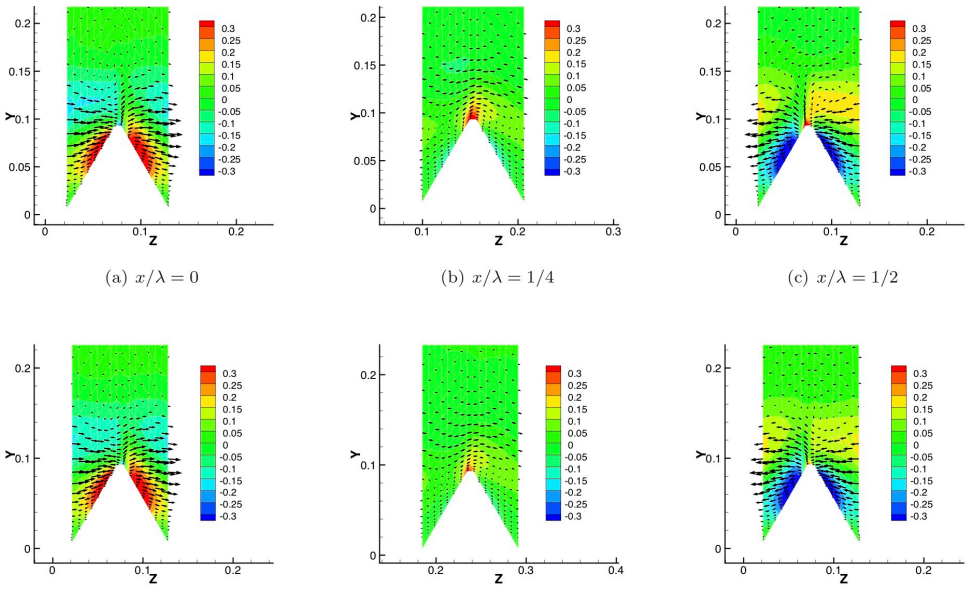

Fig. 3.27: Mean streamwise vorticity (colors) and mean velocity vectors for different transverse planes. Letters a), b) and c) are referred to the λ/δ=3.22; letters d), e) and f) are referred to the λ/δ=6. (Peet et al., 2008)

the evolution at different distances in reference to the wavelength, precisely at 0%, 25% and 50% of the wavelength of the riblets. What is shown is that for the straight riblet a secondary flow develops attached to the riblet: this flow is caused by the turbulent momentum transfer from the central region of the riblet to the valley, then rises from the valley to the tip along the riblet surface, as also reported by Choi et al. (1993), and similar to the sloshing described by Bechert et al. (1997). Meanwhile for the sinusoidal riblets, figure 3.27 shows a different behavior. At a chord of 0%, the flow turns in a positive spanwise direction that results in a positive streamwise vorticity on the surface; as the flow moves down stream, it aligns itself along the riblet, while the surface streamwise vorticity is greatly reduced, at 25% of the chord. Finally at 50% of the chord, large negative streamwise vorticity appears due to a negative spanwise direction. Peet et al. (2008) noted that the maximum mean vorticity level for the sinusoidal riblets were six times that of the straight riblet, equal to 0.05. Taking into consideration a wider instantaneous view of the flow, above the riblet surfaces, Peet et al. (2008) produced figure 3.28, in which the features of the flow are plotted along the velocity vectors in the wallward

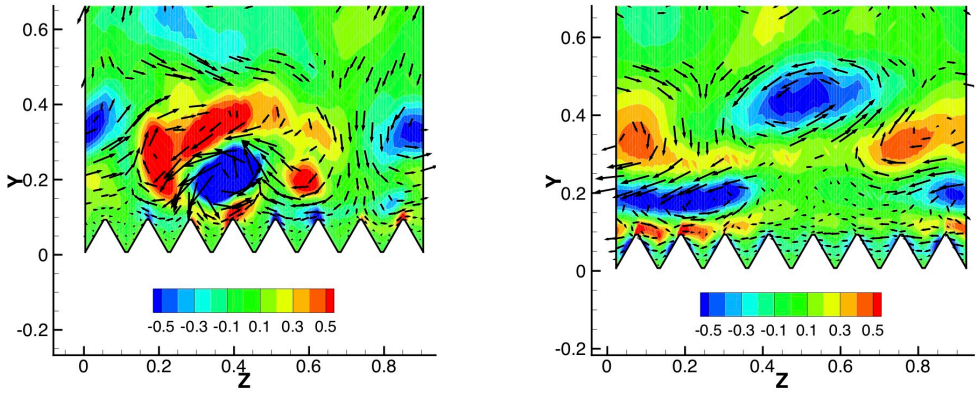

(a) Straight riblets

(b) Sinusoidal riblets (Sinus 1 case)

Fig. 3.28: Instantaneous streamwise vorticity (colors) and instantaneous velocity vectors in a transverse plane. (Peet et al., 2008)

and spanwise directions. This time only the sinusoidal riblet with wavelength ratio of 3.22 is considered. Straight riblets, figure 3.28.a, are able to move away from the wall the coherent streamwise vortices, as previously found by Choi et al. (1993) and Choi (1989). Such vortices often come in pairs and represent, as Robinson (1991) and Adrian et al. (2000) showed, the hairpin legs, that pump high-speed fluid towards the wall and eject low-speed fluid away from it. In the case of sinusoidal riblets, figure 3.28.b, the structure of boundary layer differs a lot, at least comparing the instantaneous photograph. The streamwise vortices are not alongside, instead on top of each other. Vorticity, that spawned from the riblet surface, is shed into the boundary layer and lifted above by the spanwise motion. Also the vorticity is shown in layers, limited to only four.

Beyond there seems to be no vorticity, probably because of the now weak spanwise motion. Such organized vortex shedding alts the production of canonical streamwise vortices, drastically reducing the turbulence production due to bursts at the wall, hence reducing the turbulent component in skin friction drag. A better depiction of such well organized vortex structure is reported in figure 3.29: while near the wall in the straight riblet

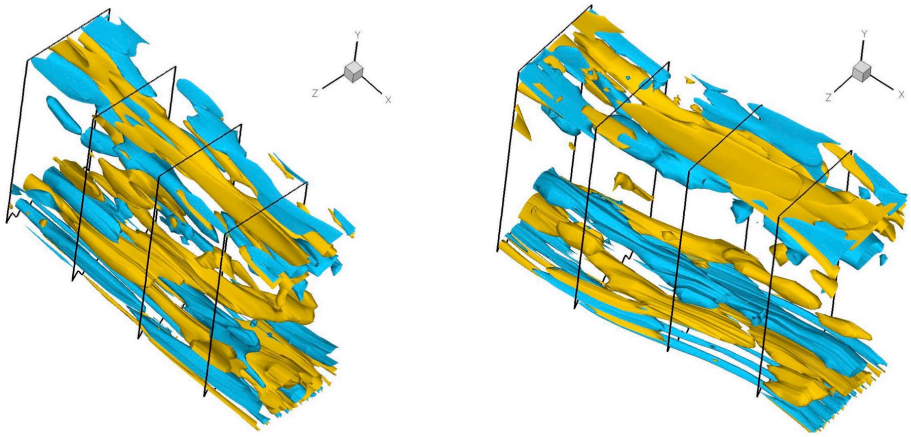

(a) Straight riblets (b) Sinusoidal riblets (Sinus 1 case)

Fig. 3.29: Isosurfaces of instantaneous streamwise vorticity. (Peet et al., 2008)

case, figure 3.29.a, is quite noticeable the chaos of vortex production, in the sinusoidal case, figure 3.29.b, the streamwise vortices are much better aligned and organized, almost resembling a laminar behavior. Finally the statistics shows, in figure 3.30, that streamwise turbulence intensity is slightly greater for the sinusoidal riblets than the straight ones,

while the spanwise turbulence is noticeably reduced for the sinusoidal riblets, compared to straight ones. A possible

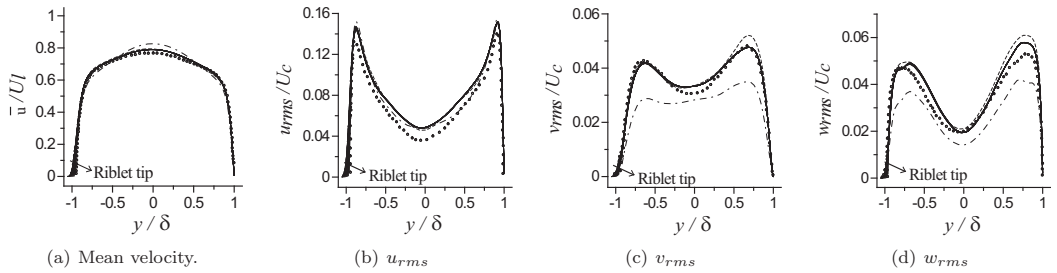

(a) Mean velocity. (b) u_{rms} (c) v_{rms} (d) w_{rms}

Fig. 3.30: Statistics data for Smagorinsky's model (—), modified Smagorinsky's model (- -), dynamic model with local averaging (-··-), DNS (∘). (Peet et al., 2008)

explanation for the former behavior involves the increase of fluctuations in the streamwise direction, because of inhomogeneity of the mean flow in that same direction, while for the great reduction in spanwise turbulence is due to the annihilation of the irregular coherent streamwise vortices. Hence, when transverse turbulent fluctuations are restrained and brought to a minimum, the transfer of turbulent momentum close to the wall is also reduced, and in turn so does the shear stress, greatly impacting the drag reduction. The latter is the reason why they were included in our research project.

Chapter 4 - Experimental setup and procedure

The experimental research at the core of this thesis was carried out in the aerodynamic laboratory Modesto Panetti of the Polytechnic Institute of Turin, during the second quarter of 2019. The object of this period was to confirm the results found in the aforementioned literature, by studying our own riblets surfaces. Straight and sinusoidal riblets were studied, which will be better described in section 4.2. Additionally, the final goal of the research was to determine a new procedure, built from the ground up, on how to take drag measurements with riblets surfaces, in order to later study the viscous sublayer by digital particle image velocimetry or D-PIV.

4.1 The wind tunnel and its accessories

The wind tunnel used in this research is located in the aerodynamic laboratory dedicated to Modesto Panetti, in the department of Aerospace Engineering of the Polytechnic Institute of Turin. As a historical side note, Modesto Panetti was one of the first professors of aeronautics in Italy, introducing the new discipline in Italy at the Polytechnic Institute of Turin, in which he established the aero-technique laboratory. He, after WWII, was elected senator of Italian republic and later served as minister of the Postal and Telecommunication ministry in 1953 (Source: I.T.I.S. "Modesto Panetti" website).

The particular wind tunnel used in the research is of the open circuit type, having a rectangular testing chamber, as depicted in the scheme in figure 4.1, identified with its color "Fucsia". The seven main sections are:

1) Inlet convergent;
2) Electric motors;
3) Divergent with screens and honeycomb mesh;

4) Settling chamber;

5) Convergent;

6) Testing chamber;

7) Upward deflector.

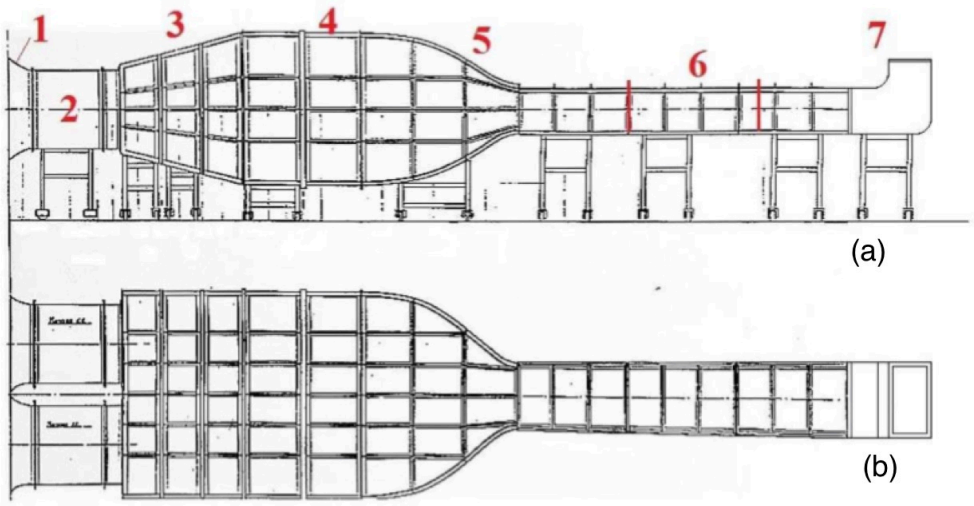

Fig. 4.1: Schematics of the wind tunnel; a) left view; b) top view.

The electric powering the wind tunnel are the old MC 104 CD from 1964, made by Marelli. With a power of about 9700W,

Table 4.1: Characteristics of the wind tunnel.

Characteristic	Value	Measuring Unit
Length test chamber	4	m
Height test chamber	0.5	m
Width test chamber	0.7	m
Divergence	0.5	degrees
Contraption ratio	12:1	
Maximum velocity	30	m/s

they move two co-rotating fans, visible with the inlet convergent in figure 4.2.

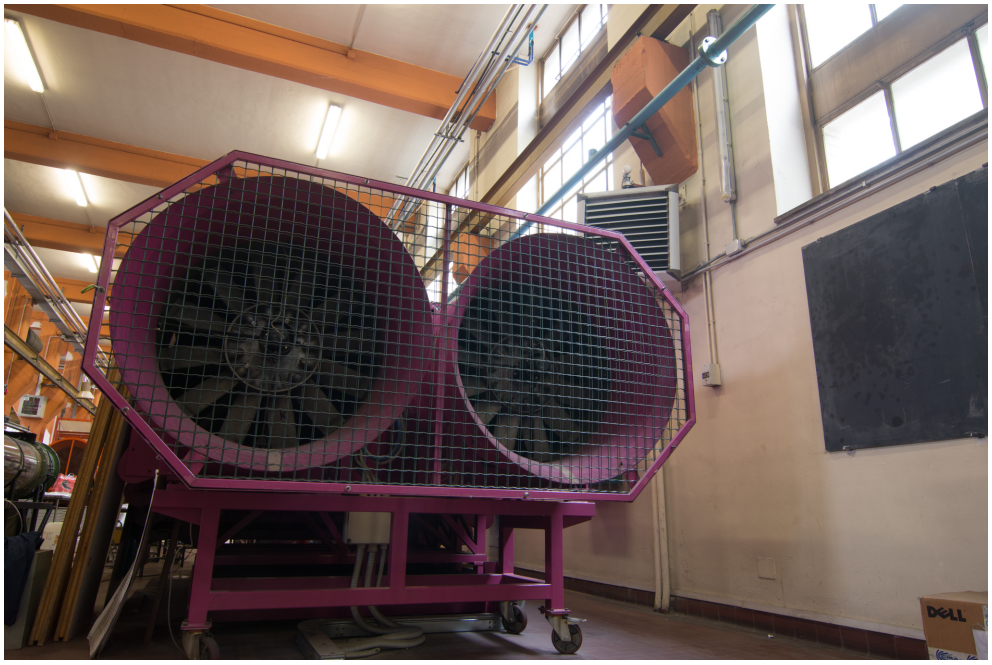

Fig. 4.2: Inlet and rotors of the wind tunnel.

Fig. 4.3: Right side view, with the operational table and side panel of the testing chamber removed.

In figure 4.3, from right to left, can be seen the convergent that leads to the testing chamber. A medium density fiberboard runs from the convergent through the whole testing chamber, for the whole length of about 4 meters. The testing chamber, which dimensions are reported in table 4.1, can therefore be seen divided by such board, in figure 4.4, which was

Fig. 4.4: Closer view of the testing chamber with the medium density fiberboard in the middle of the frame. From it, the various tubes for measuring the pressure gradients hang.

developed in order to use this wind tunnel only for boundary layer research on the top half. Access to the testing chamber is given by two panels, one on each side, made of acrylic. One of the three panels that divide the testing chamber has a rectangular opening to allow the positioning of the riblet

Fig. 4.5: Inside view of the testing chamber. Flow is moving towards the viewer. It's noticeable the labyrinth in the hole for the plaques.

surface, as seen in figure 4.5. The midpoint of this cavity is found at 1.6m from the leading edge of the ideal flat plane that runs inside the wind tunnel, far enough that a turbulent boundary layer is fully formed. However, a strip of aluminum tape, with multiple tiny edges was added about 50cm upstream the leading edge of the cavity, seen also in figure 4.5. Halfway the thickness of the board is located a labyrinth. The task of this random structure is to avoid any leakage from the top half, where the air is pumped, to the bottom half, disconnected from the rest of the wind tunnel and therefore it doesn’t experience any flow. The same panel is equipped with a series of static pressure probes, which location is identified in

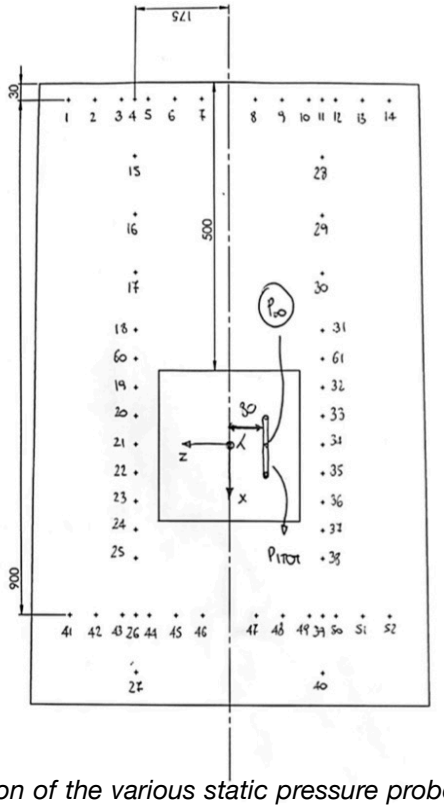

Fig. 4.6: Location of the various static pressure probes on the main board. The flow moves downward in reference to the picture.

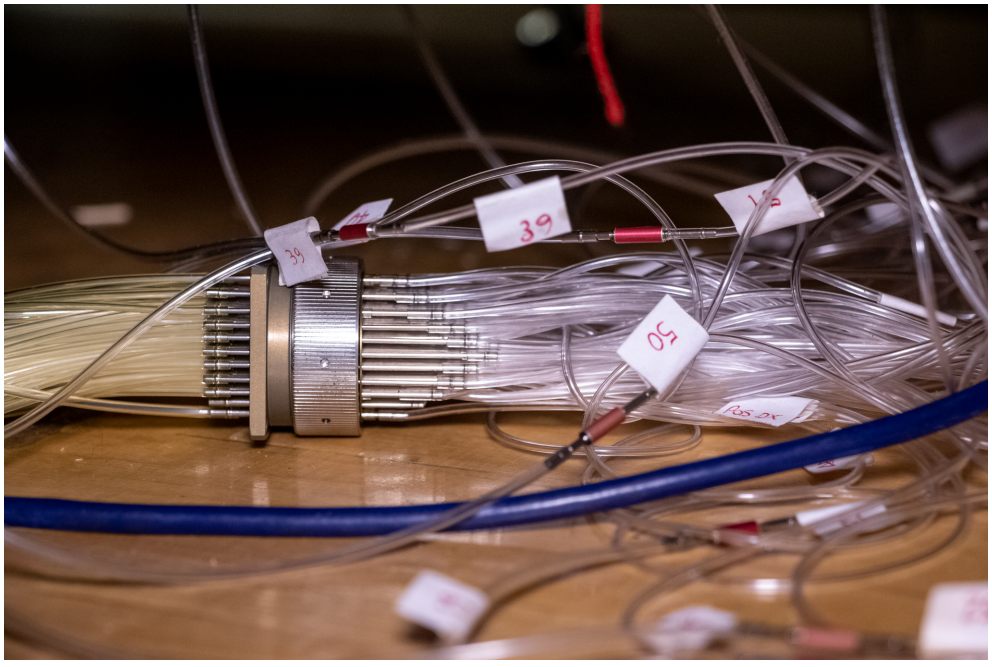

Fig. 4.7: The ZOC33 Scanivalve, used for measuring the static pressures at the wall.

figure 4.6, used to measure the streamwise and spanwise

Fig. 4.8: Inner view of the upward deflector.

Fig. 4.9: The wind tunnel control panel, with the various controls for each motor and the two displays.

pressure gradients. Each probe has a unique tubing, visible in the bottom half of figure 4.4, that connects to a Scanivalve,

visible in figure 4.7.

Inside the upward deflector is a series of slits that deflect the flow upward: they are visible in figure 4.8.

The wind tunnel is controlled by a dedicated panel, figure 4.9. Each motor can be controlled singularly or simultaneously. Two LCD panels indicate the speed in [RPM]. The maximum rotational speed that can be achieved is 1350RPM, corresponding to a flow speed of about 23m/s. That velocity, however, was never achieved for safety concerns.

4.2 The riblets surfaces and their supporting apparatus

Our research project focused on the characterization of four surfaces with different features, specifically:

- flat;
- longitudinal riblets, seen in figure 4.10;

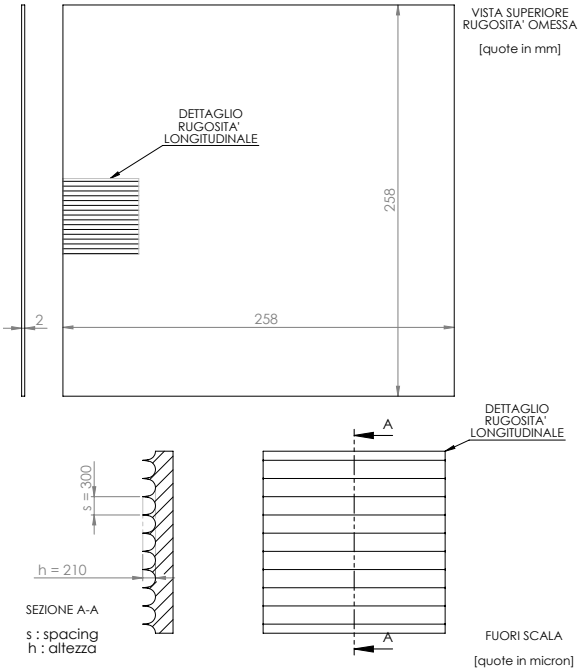

Fig. 4.10: Schematic drawing of the surface with longitudinal riblets.

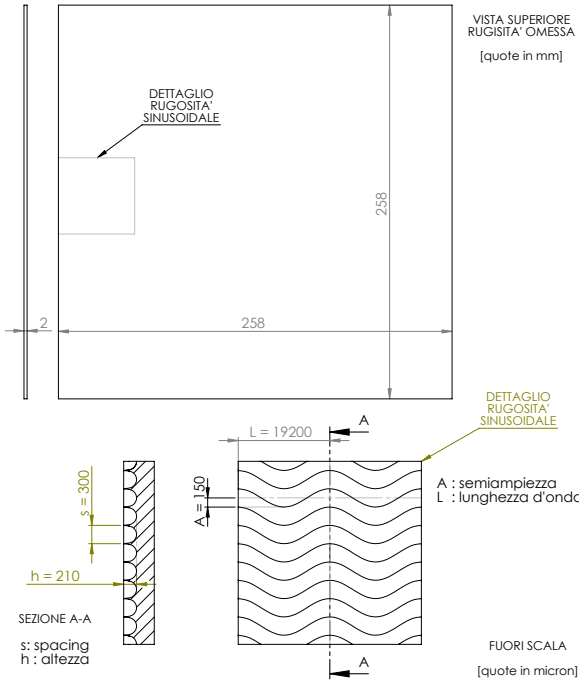

Fig. 4.11: Schematic drawing of the surface with sinusoidal riblets with amplitude a=150μm.

- sinusoidal riblets with semi-amplitude:
  - a=150, seen in figure 4.11;

- a=600, seen in figure 4.12.

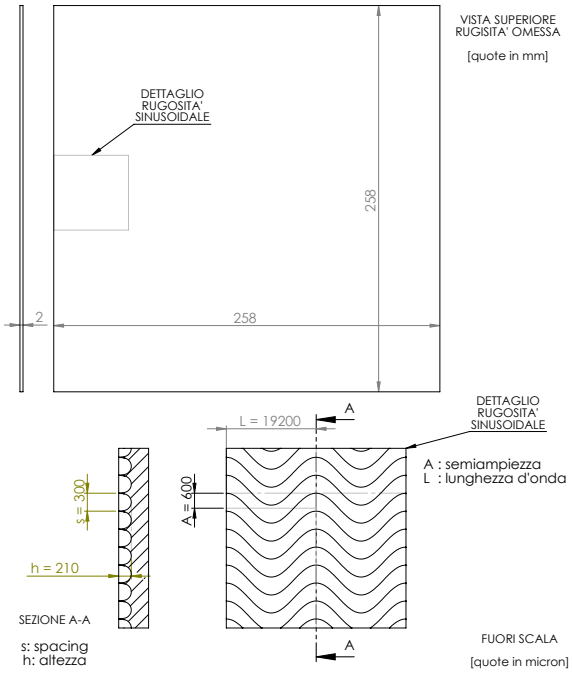

Fig. 4.12: Schematic drawing of the surface with sinusoidal riblets with amplitude a=600μm.

Fig. 4.13: Close up view of the four threaded sockets, used to attach the plaque to the force sensor.

In figures 4.10 through 4.12 are also reported the macroscopic dimensions of the four panels. All the riblets have a lateral spacing of 300μm, and height of 210μm. The riblets were manufactured in acrylic. Each plate also features 4 threaded holes, used for attaching it to the mounting apparatus, as depicted in figure 4.13.

The final mounting apparatus was actually what took most of our temporal resources, since we had to re-design it from the ground up. In previous experiments, the wind tunnel hosted a floating element balance, as depicted in figure 4.14, as reported by Magro (2017), which consisted of four containers filled with water. They allowed the floatation of the studied plate, but it was a method that required a lot of time before being operative. Additionally, it needed constant verification. Something not suitable for the later goal of the new research: PIV measurements.

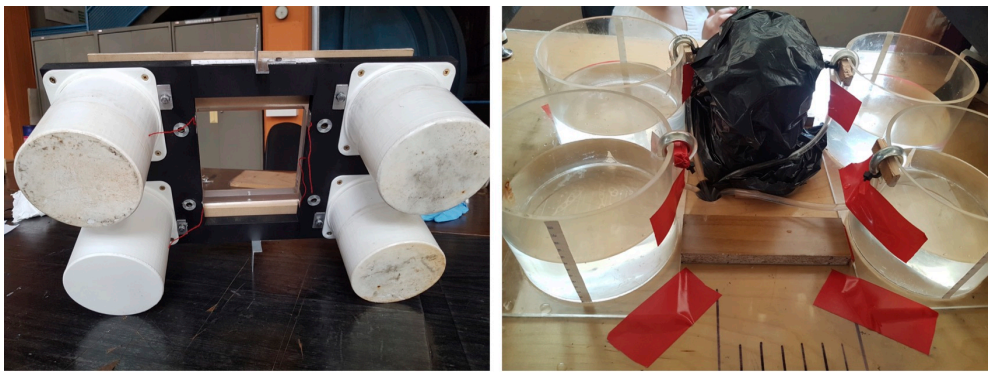

Fig. 4.14: The old floating elements (left image) to which the surfaces were attached and the four corresponding containers filled with water (right image). (Magro, 2017)

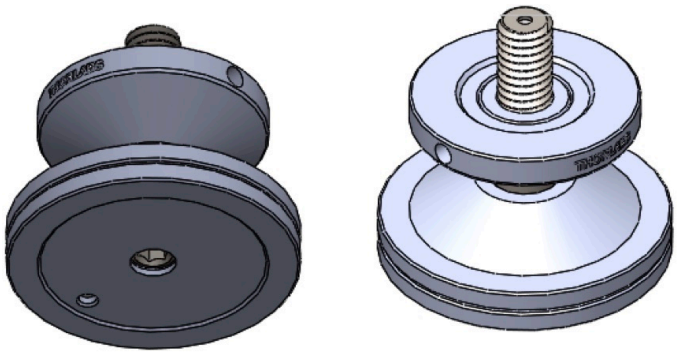

Fig. 4.15: Thorlabs' swivel foot, model SWB/M, from Thorlabs' website.

Because the wind tunnel bottom is covered by a wood board, its flatness is inconsistent from day to day, and even during one single day of collecting data, due to changes in humidity and temperature that modify the wood. It took us several trials, until we finally came to the current mounting apparatus that allowed us to study a surface in about 20 minutes. To overcome the issue of the testing chamber bottom

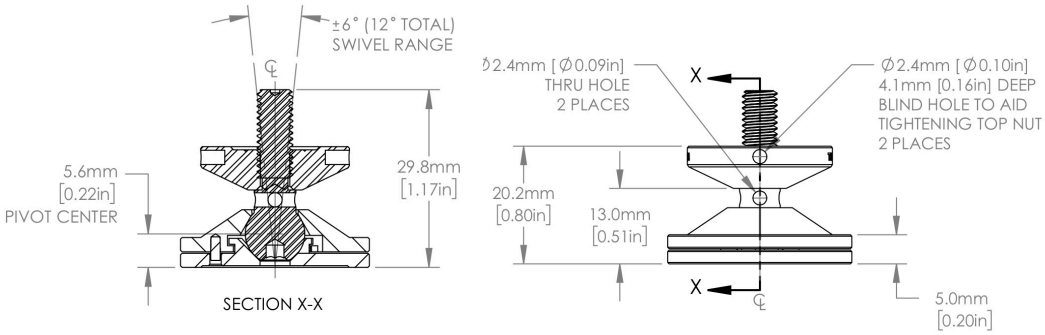

Fig. 4.16: Lateral and section view of Thorlabs' swivel foot, model SWB/M, from Thorlabs' website.

unevenness, we used three articulated mounting bases manufactured by Thorlabs, with part number SWB/M, figure

4.15. The main feature of these feet, which dimensions are depicted in figure 4.16, is their swivel capability: from the central axis of the screw, the base can swivel in a total range of 12°, allowing great conformability to any uneven surface. The total number of feet used is three, since it's the minimum and sufficient number of points across which a plane can be defined in a stable manner.

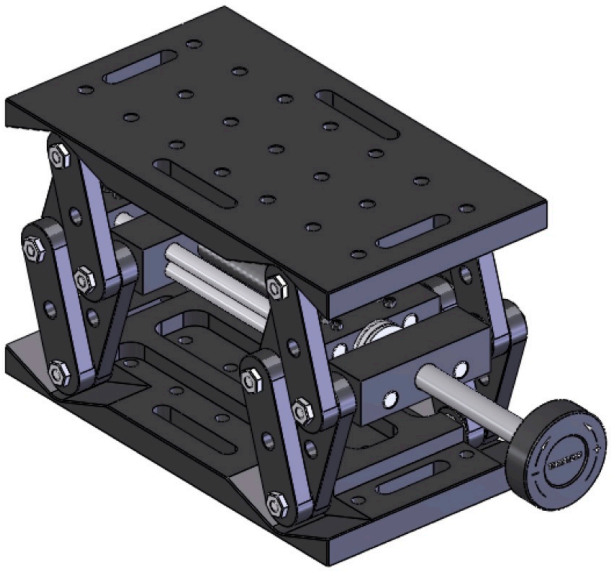

Fig 4.17: Thorlabs' lab jack, model L490/M, from Thorlabs' website.

The lab jack used is also manufactured by Thorlabs, with part number L490/M, figure 4.17, which dimensions are shown in figure 4.18. Initially two lab jacks were used, as can be seen in figure 4.19, but with the addition of a stepping motor, figure 4.20, made the whole apparatus very unstable and cumbersome to work with in the limited volume of the testing

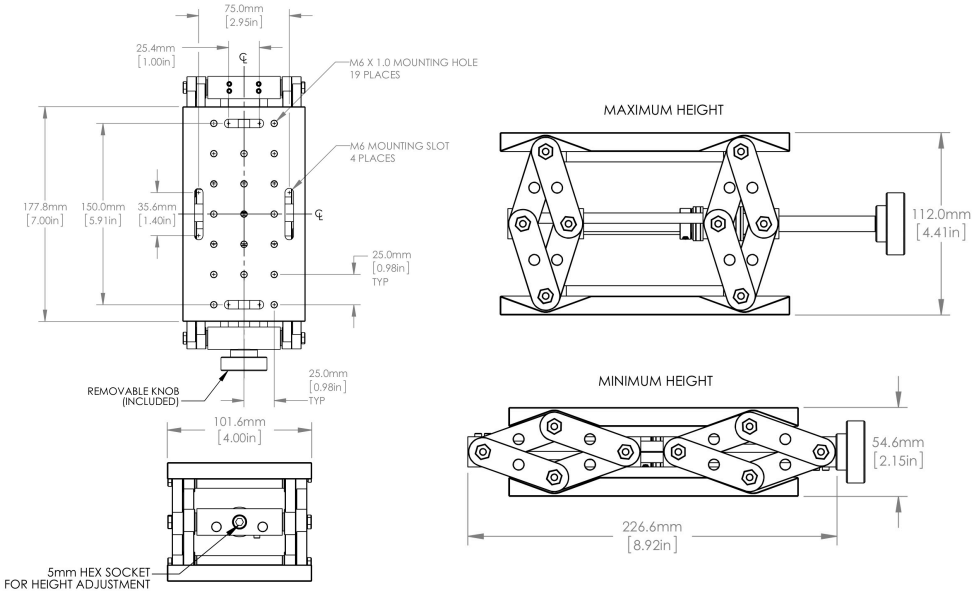

Fig 4.18: Dimensions and schematics of Thorlabs' lab jack, model L490/M, from Thorlabs' website.

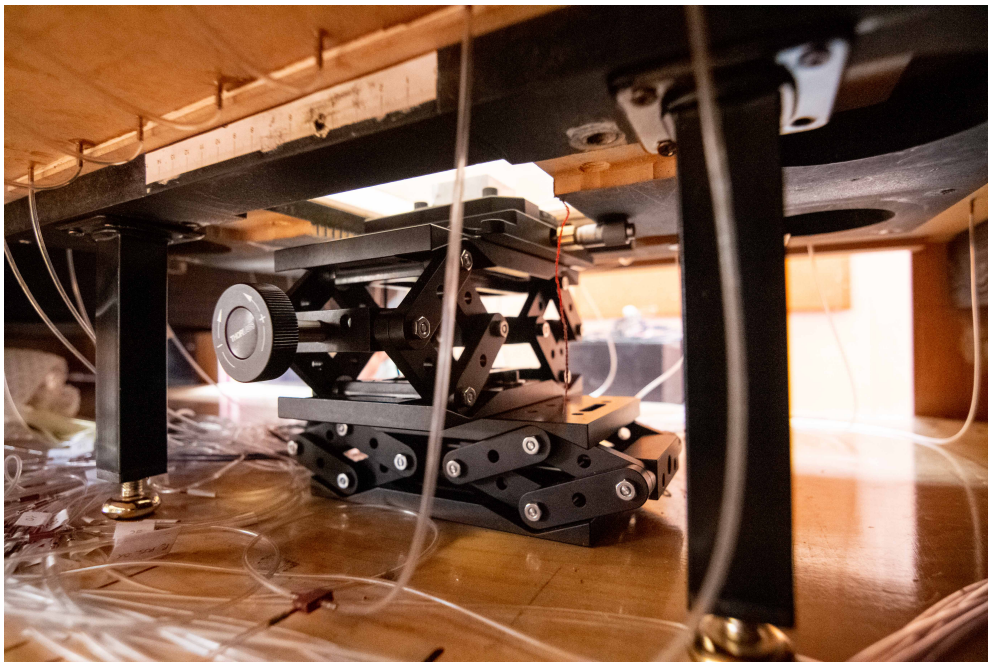

Fig. 4.19: The initial supporting apparatus with two model L490/M lab jacks. Flow moving from right to left.

chamber. Therefore in the final solution only one lab jack was used, proving to be a good choice. The stepping motor, able to complete one rotation in 200 steps, corresponding to a rate of

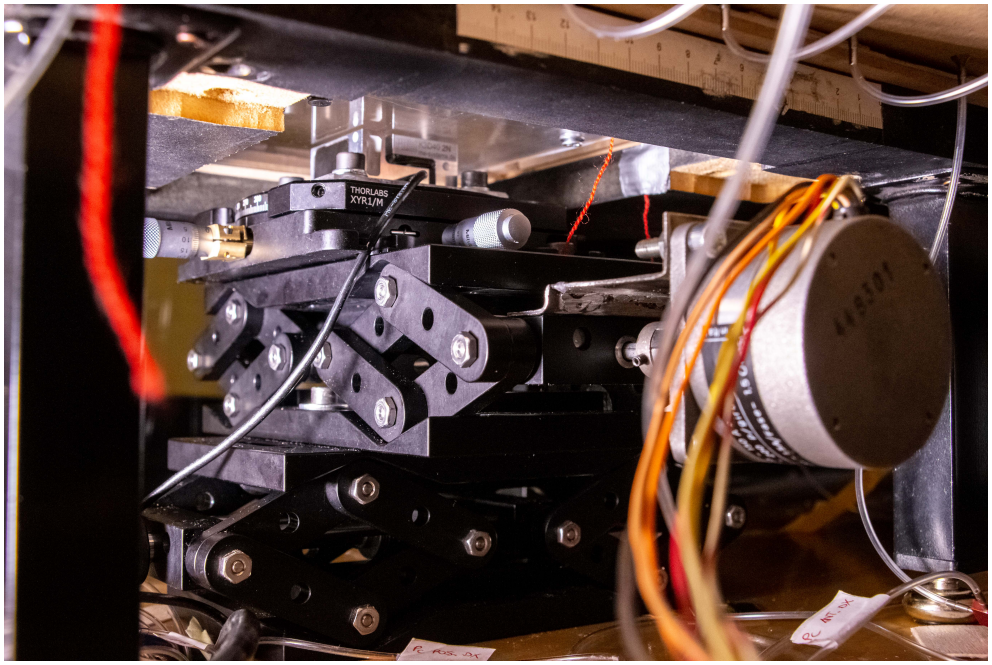

Fig. 4.20: The supporting apparatus deployed in its final position.

Fig. 4.21: Stepping motor MAE HY-200-2215-A-8, used to change the y position of the plaque.

0.02mm in 30 steps, is an old MAE HY-200-2215-A-8, figure 4.21, to which a hexagonal shaft was attached to regulate the

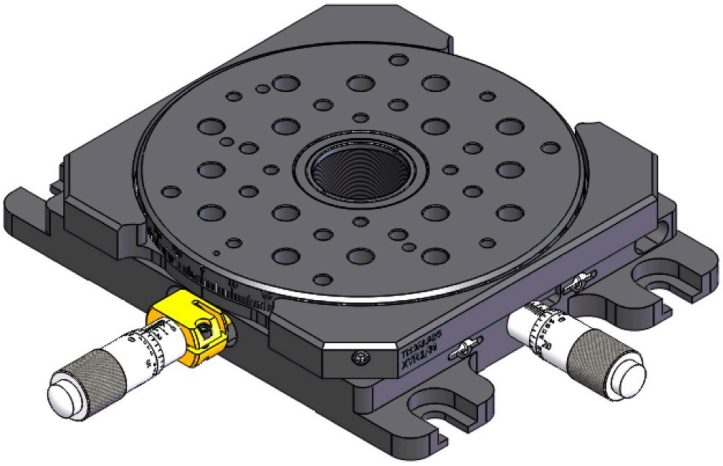

Fig. 4.22: Thorlabs' translational stage support, model XYR1/m, from Thorlabs' website.

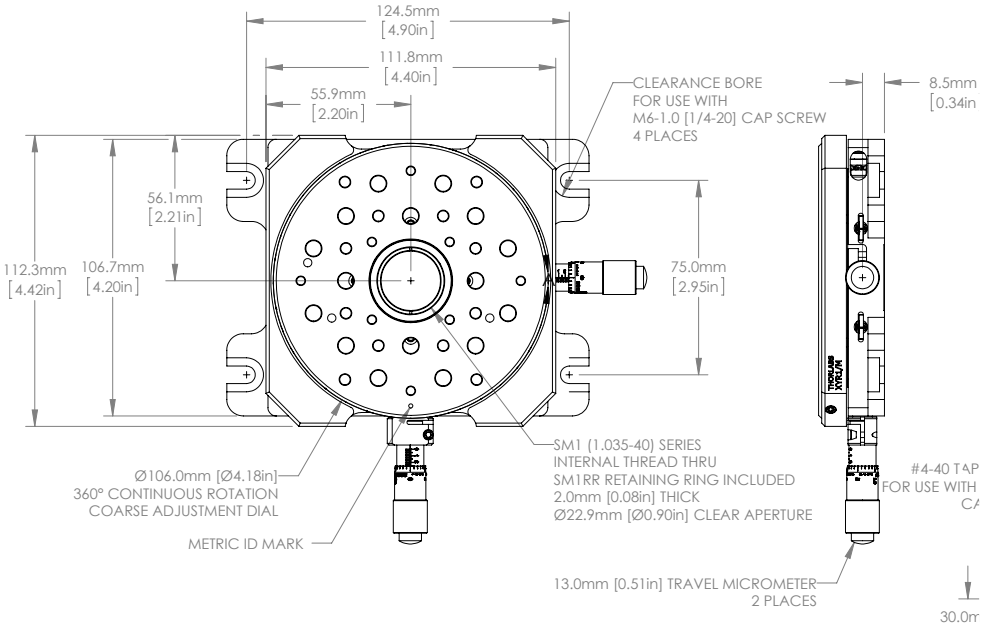

Fig. 4.23: Schematics of Thorlabs' translational stage support, model XYR1/m, from Thorlabs' website.

lab jack in the y direction, in reference to the flow. However the rate was not always consistent, since the connections between the stepping motor shaft and the hexagonal socket in the jack

lab were very loose, we lost several steps every time a change in direction was made. Therefore we later introduced the laser, described in the following section.

To better regulate the position the various plates, we needed also a 2-axis tool that would allow us the translation of the plate in the streamwise and spanwise directions, as well as the rotation around the y-axis. This tool would allow to leave an accurate gap between the testing chamber floor and the test plate, so that no contact is made. Additionally we can control the correct alignment of the riblets to the flow, by a rotating adjustment. The instrument that gave us such controls is the

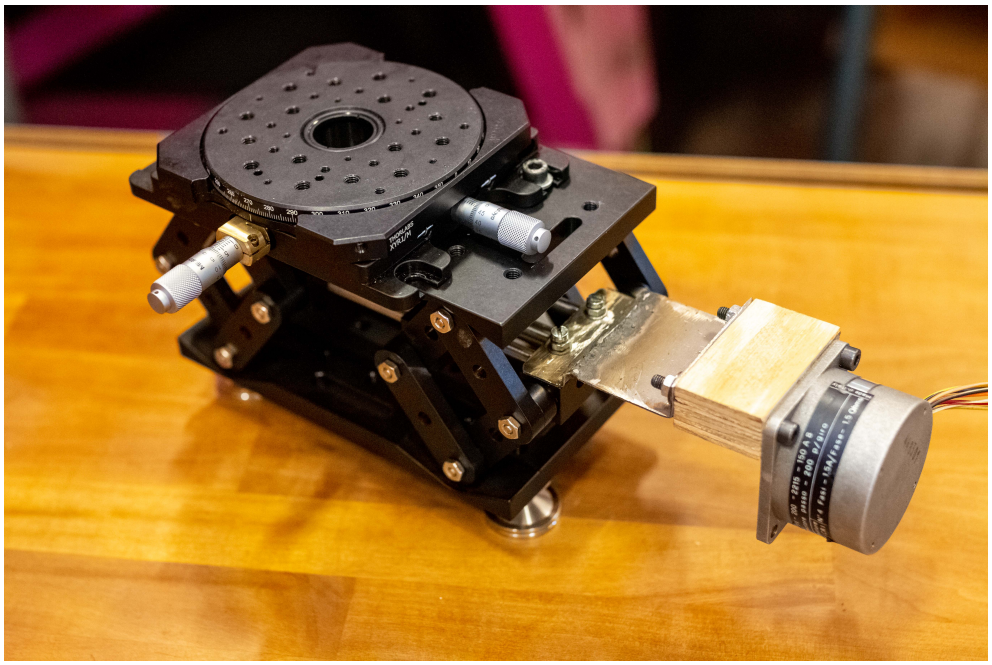

Fig. 4.24: View of the completed supporting apparatus, with Thorlabs' translation stages support and lab jack. The stepping motor is attached to the latter.

Thorlabs' XY translation stages, with part number XYR1/M, in figure 4.22 its rendering, while in figure 4.23 its dimensions and features. The supporting apparatus in its main components is visible in figure 4.24, mounted together with M6 screws.

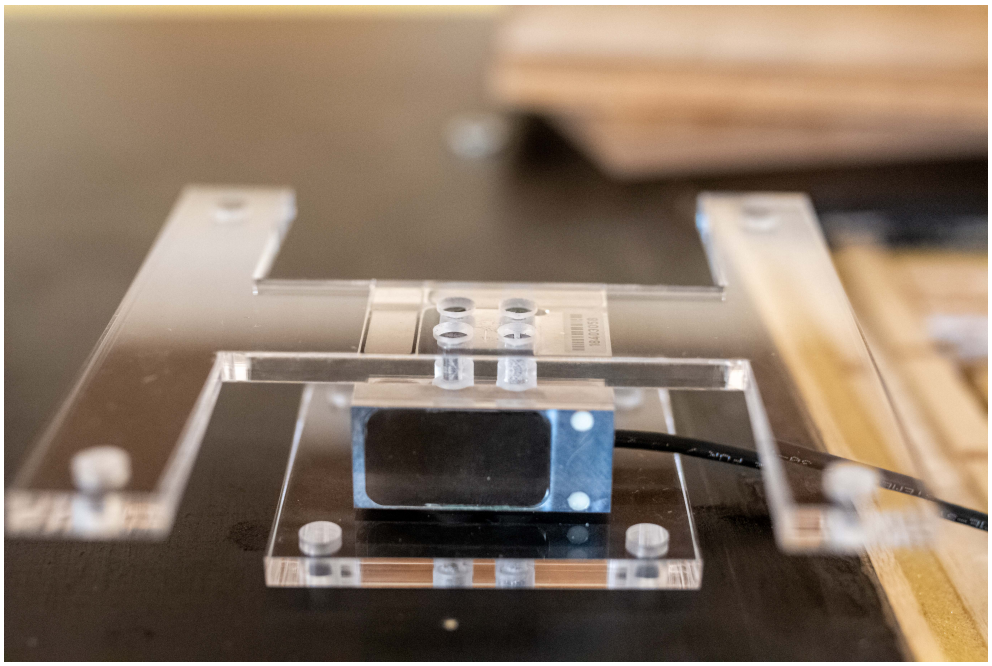

Fig. 4.25: View of the 3-axis force sensor K3D40±2N, with the two acrylic interfaces for the supporting apparatus (bottom plate) and the various plaques (top H-shaped plate).

Finally, on top of it, an acrylic plaque was mounted. The plaque is an interface between the support and the force sensor (see section 4.3 for more info), on top of which another H-shaped plaque is placed, working as an interface between the force sensor and the various surfaces to be tested. The top assembly can be seen in figure 4.25.

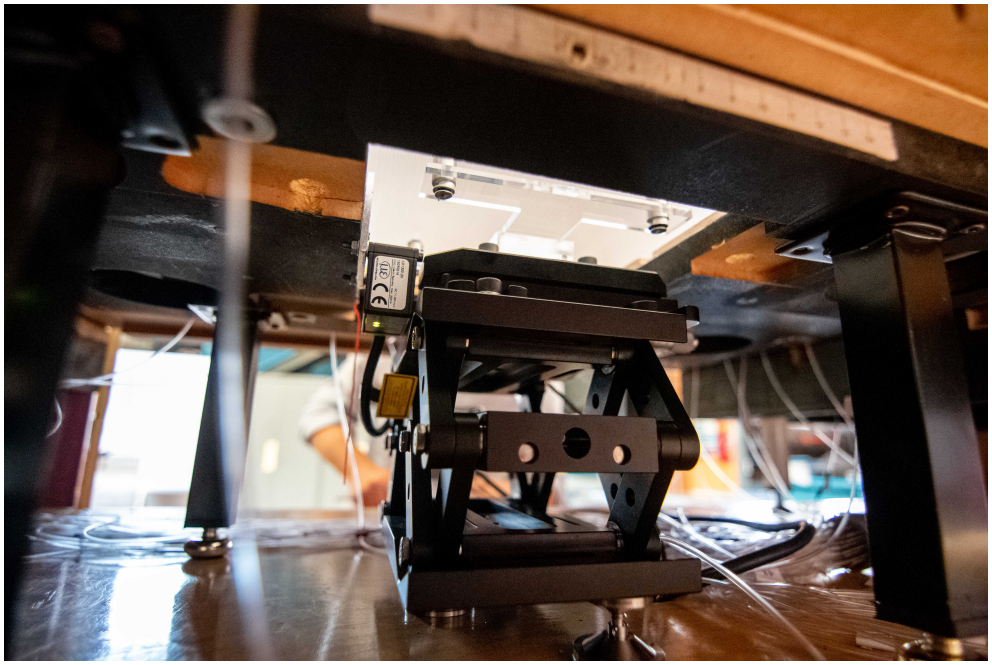

Fig. 4.26: Left side view of the supporting apparatus in its working position.

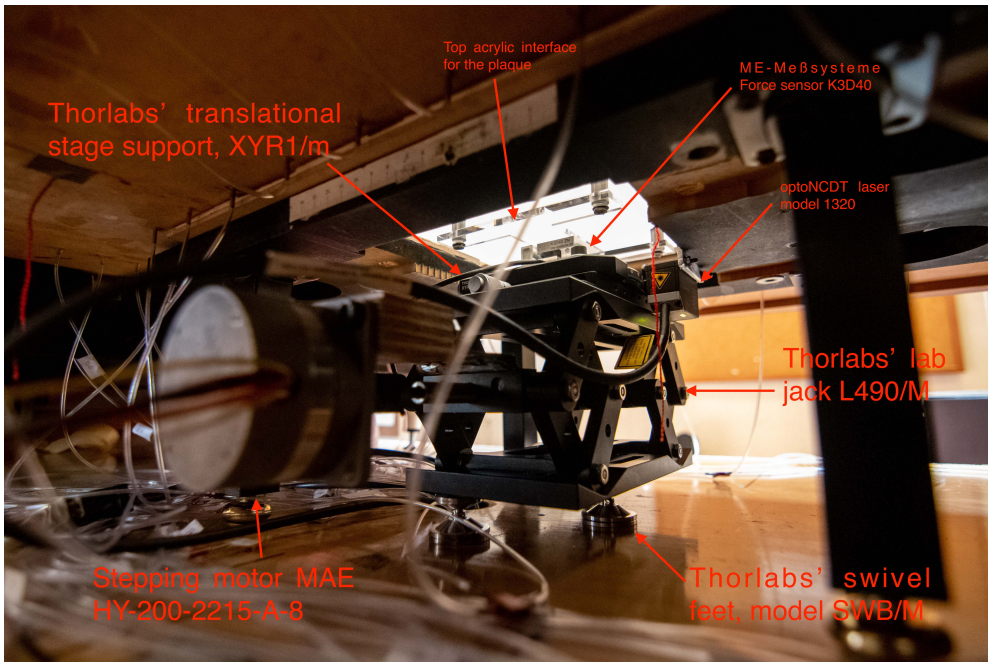

Fig. 4.27: Right side view of the supporting apparatus in its working position.

The supporting apparatus can be seen in its final configuration and deployment in figure 4.26, seen from the

right side of the wind tunnel, and figure 4.27, seen from the left side of the wind tunnel, with each component labelled.

4.3 Data acquisition instruments and procedure

The main goal of the research project is to directly measure the drag experienced by the surface interacting with the flow. Such task was achieved with the use of the force sensor, previously mentioned. The sensor used is the K3D40, three-axis force sensor manufactured by ME-Meßsysteme, specifically the variant model capable of measuring forces up to ±2N. Technical specifications are listed in table 4.2. The model, already visible in figure 4.25 but better depicted in figure 4.28, with dimensions and features listed in figure 4.29, was powered and its signal processed by a Vishay 2210 Signal Conditioning Amplifier system, figure 4.30. Although we had the ability to read three channels, from the three axis force

Table 4.2: Characteristics of theME-Meßsysteme three-axis force sensor K3D40.

Characteristic	Value	Measuring unit
Rated force (x,y,z) (tension/ compression)	±2	N
Operating force	200	% FS
Natural frequency	500	Hz
Height	20	mm
Length/width	40	mm
Torque limit	5	Nm
Bending moment limit	5	Nm
Breaking force	600	% FS
Accuracy class	0.5	%
Relative linearity error	0.2	% FS
Crosstalk x-to-y and y-to-x	0.5	% FS
Crosstalk z-to-x/y and x/y-to-z	1	% FS

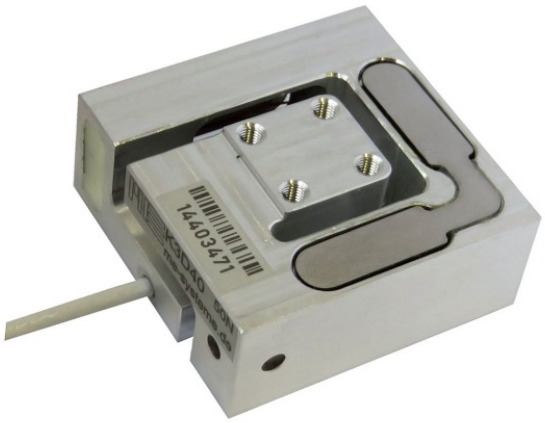

Fig. 4.28: 3-axis force sensor, model K3D40±2N, by ME-Meßsysteme.

sensors, we used only the streamwise axis, for a time constraint and due to several technical issues on learning the

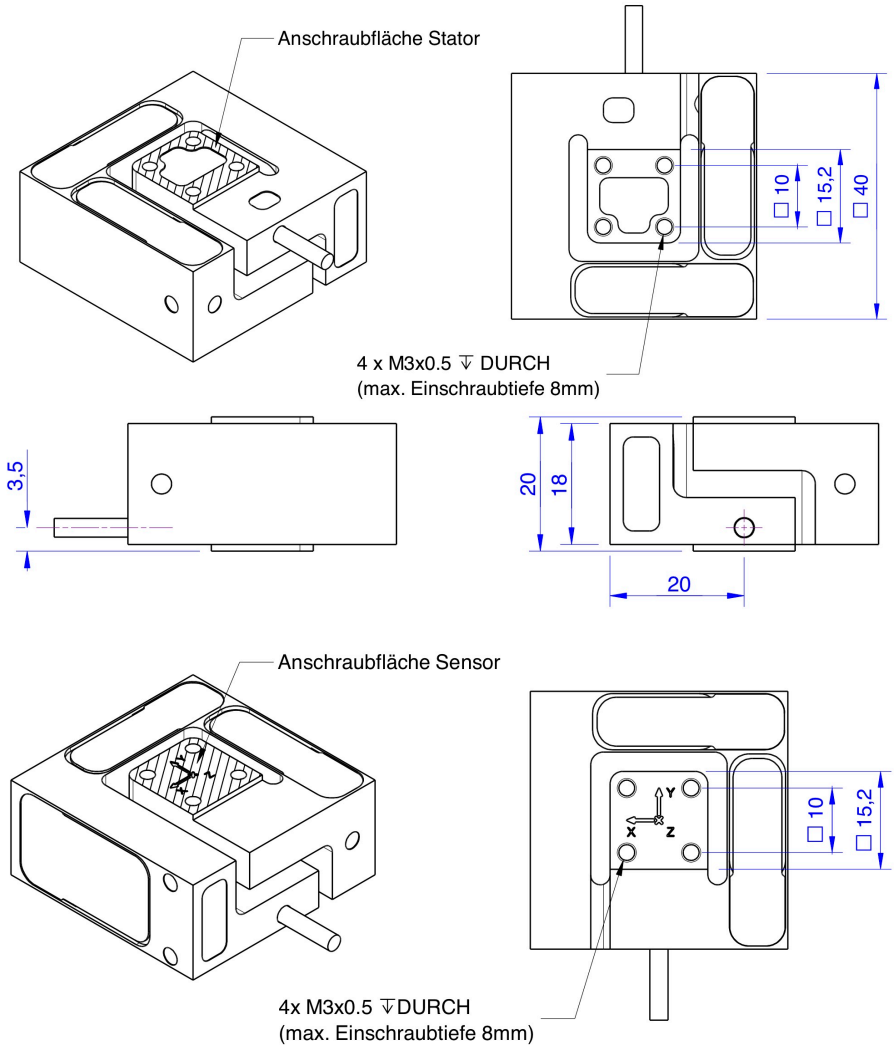

Fig. 4.29: Bottom, lateral and top view and dimensions of the 3-axis force sensor, model K3D40±2N, from ME-Meßsysteme website.

new sensor. For example, at one point, we were deceived by near-by streetcar passing close to the lab: the force sensor was so accurate that we detected the wallward fluctuations. Another time we had to call the producer technician to actually explain to us how we could and could not use the force sensor. Therefore we settled for the simplest architecture to gather the necessary data.

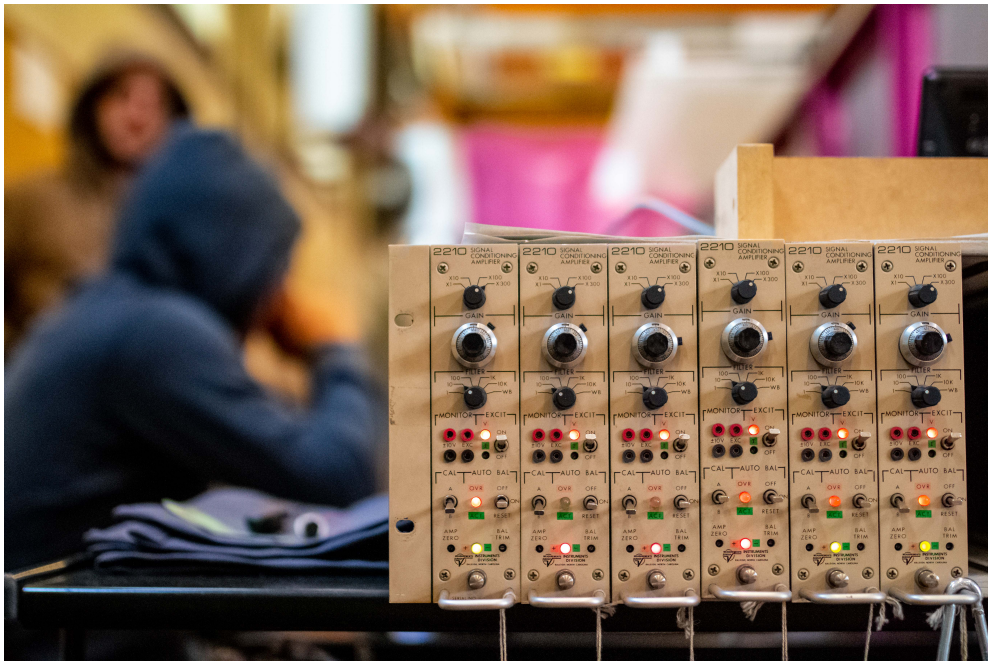

Fig. 4.30: View of the array of Vishay 2210 Signal conditioning amplifier system.

The signal was read by LabView® via some National Instrument modules that can interact digitally with the computer. Another module was dedicated to the already mentioned Scanivalve, to get the pressure gradients, and a third was dedicated to write the laser reading. The laser used is manufactured by optoNCDT, model number 1320, ideal for measuring lengths with an accuracy of just 9µm, enough to determine which part of the riblets are exposed to the flow. The laser is attached to the medium density fiberboard to give a reading of the distance between it and the bottom side of the plate, covered with black tape.

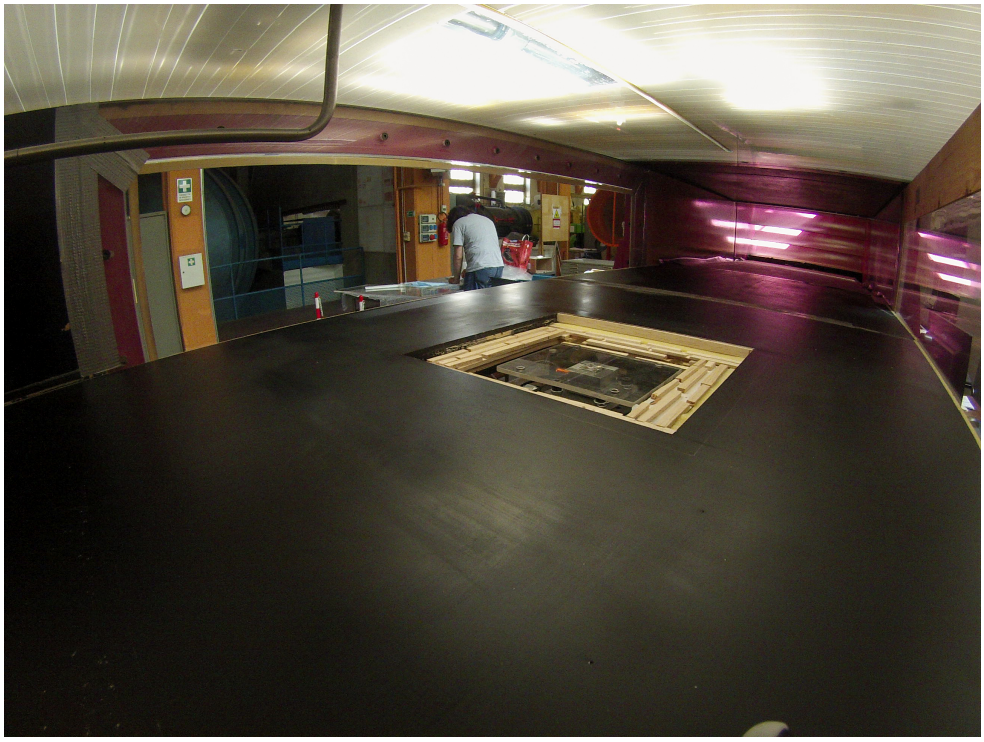

Fig. 4.31: View from inside of the test chamber with the cut out on the flat plane where the plaque will be positioned.

To another National Instrument® module, model Setra 239C, was attached a Pitot tube, visible in figure 4.5, positioned above the testing plate at about halfway the height of the testing chamber.

The procedure to set up the experiment and to acquire the necessary data took about 16 minutes, according to a timelapse I produced during the research campaign. After removing the left side acrylic panel of the testing chamber, in figure 4.31 I'm shown preparing the testing plate. This step consists of screwing in threaded sockets onto the testing plate,

figure 4.13, making sure that they are separated by a rubber

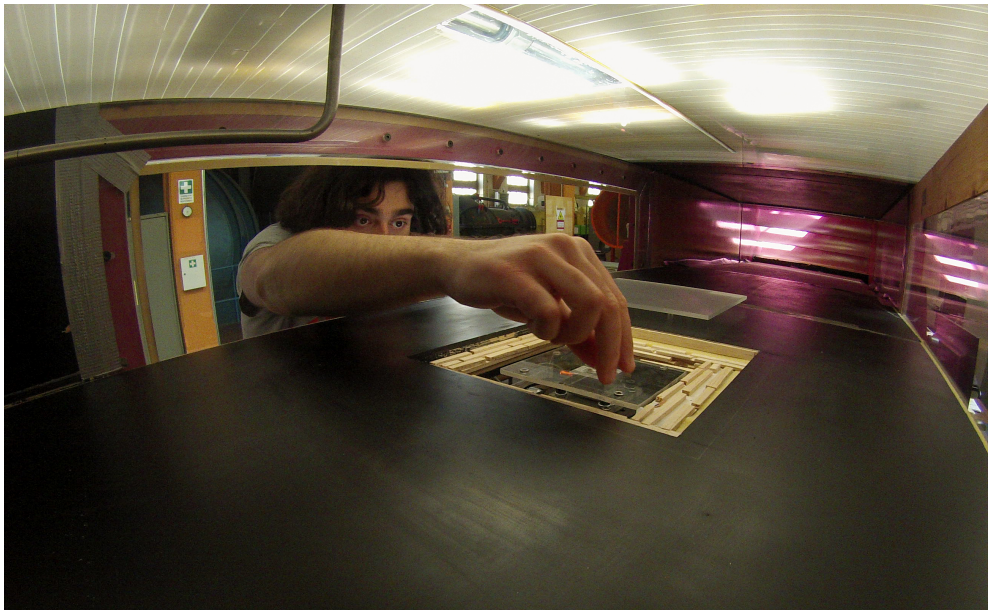

Fig. 4.32: View from inside of the test chamber while positioning the metal gaskets on the acrylic interface.

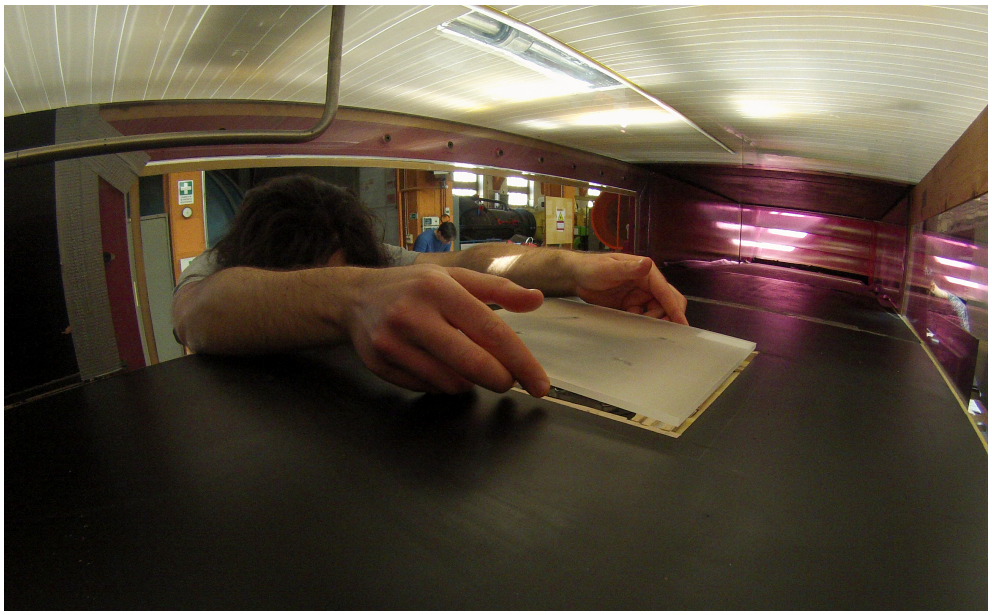

Fig. 4.33: Manual positioning of the test plaque onto the acrylic interface, making sure to intercept the metal gaskets.

gasket, to avoid damaging the plate. Also they were tighten

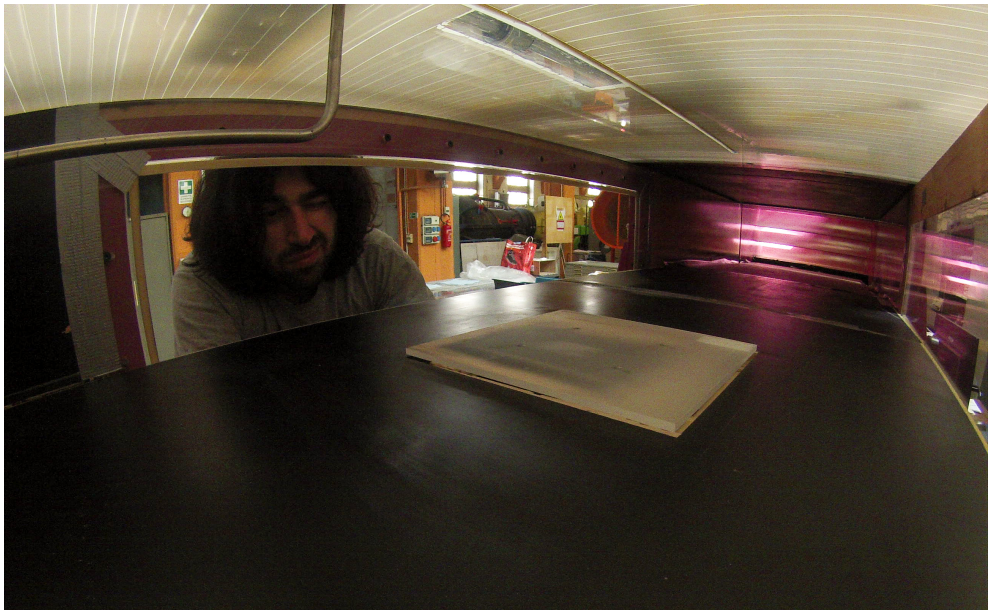

Fig. 4.34: Preliminary visual check of the plaque positioning.

just enough until the thread was all in, without further strength. The testing plate is then moved inside the testing chamber, where the interface plaque, between the 3-axis force sensor and the plate, is prepared by first lifting it all the way upward and then by positioning several metal gaskets on each hole, as portrayed in figure 4.32. Finally the plate is carefully moved into position, making sure not to disturb the loose metal gaskets placed earlier, figure 4.33. This was a tricky step, since the supporting apparatus was not leveled yet, and any sudden move could have dislodged the metal gaskets. Once the test plate was on, it was the turn of inserting and tightening the screws from below: a step where patience was needed with a

pinch of acrobatics, given the tight space available and having a screw precariously attached to the screwdriver moving amidst the jungle of instruments and pipes, as figure 4.27 shows. With the plate securely fastened, the whole apparatus was then gently lowered in order to accomodate the plate in its final position making sure, figure 4.33, that it didn't touch the inner board of the cavity it would sit in. The leveling of the plate comes next. First by means of adjusting the height of the Thorlabs' swivel feet, so to make the plate plane coincide with the plane of the medium density fiberboard, while assuring a gap surrounding the plate of about 2-3mm, small enough to avoid any leakage of flow toward the bottom half of the testing chamber, but also big enough to allow its displacement due to the drag force, without any unwanted contact that would pollute the data collection. When the co-planarity was reached, it was the turn of adjusting the height of the riblets, or of the top part of the testing plate: the tips had to be at the same level of the medium density fiberboard. To do so, a flat piece of glass and a sheet of paper were used. The riblets plate was lowered consistently, the piece of glass placed to cover the cavity from three sides, and the piece of paper in between the

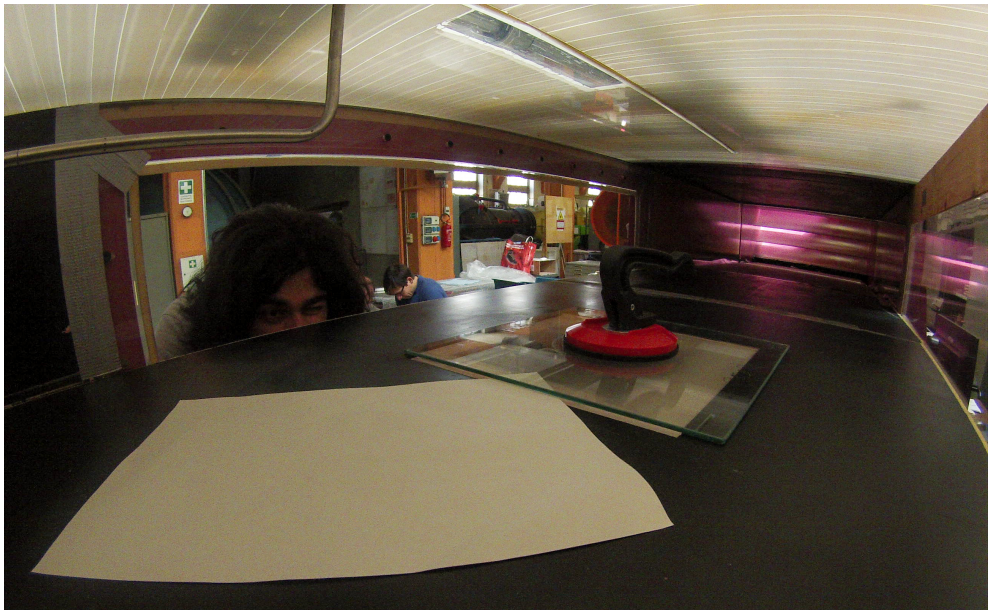

Fig. 4.35: Leveling of the plaque to the flat surface of the test chamber.

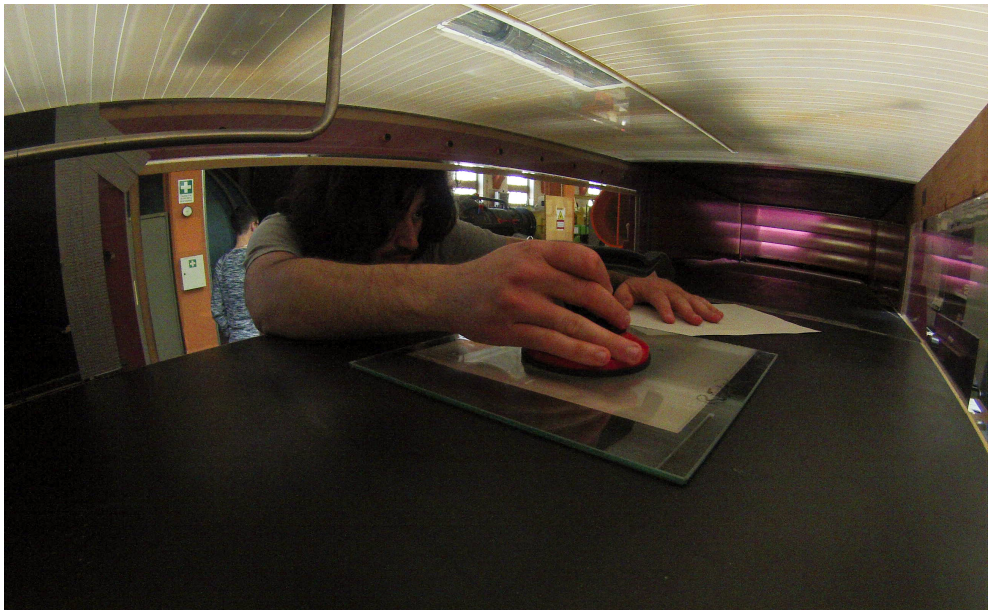

Fig. 4.36: Leveling of the plaque to the flat surface of the test chamber, from the downstream position.

riblets and the glass, as shown in figure 4.35. The same was repeated in the rear side, to ensure good leveling, as seen in figure 4.36. When the sheet of paper is slightly grasped by the

riblets tips, the initial height was achieved. That was also the zero height measured by the laser.

After a final check by the professor Gaetano Iuso and the

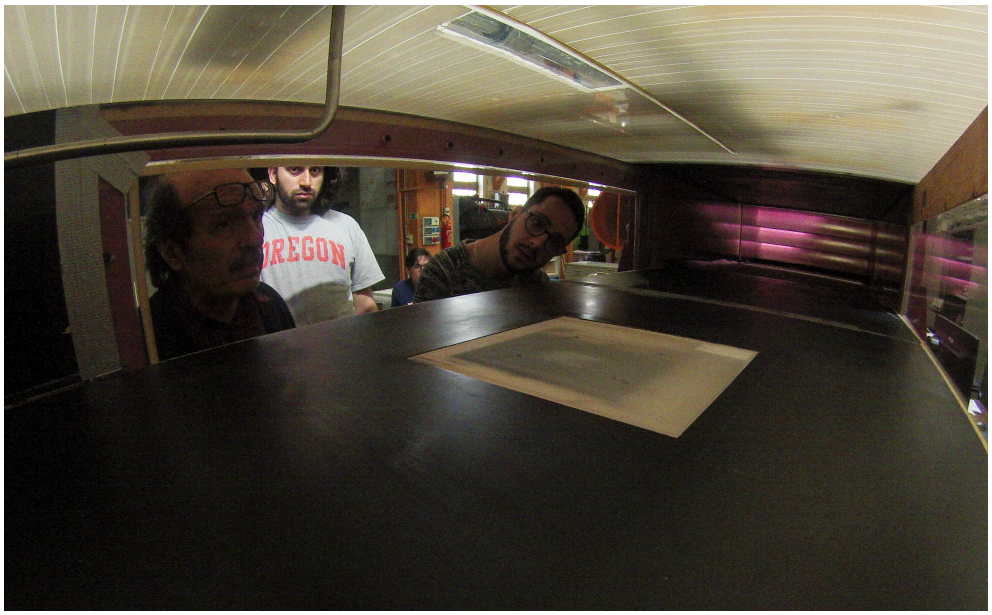

Fig. 4.37: Professor Iuso and colleague Scrimieri double checking the positioning of the plaque.

colleague Luigi Scrimieri, figure 4.37, the wind tunnel testing chamber was securely closed with the acrylic panel, seen in figure 4.38. We were ready to proceed to the next step, before powering the wind tunnel on. That was to set the data collection parameters and to tare all the instruments. Beginning from the latter, the only instrument that needed special care was the Vishay 2210 Signal Conditioning Amplifier system. Specifically its bridge needed to be re-set every time before and sometimes even between, data collection. Then, after

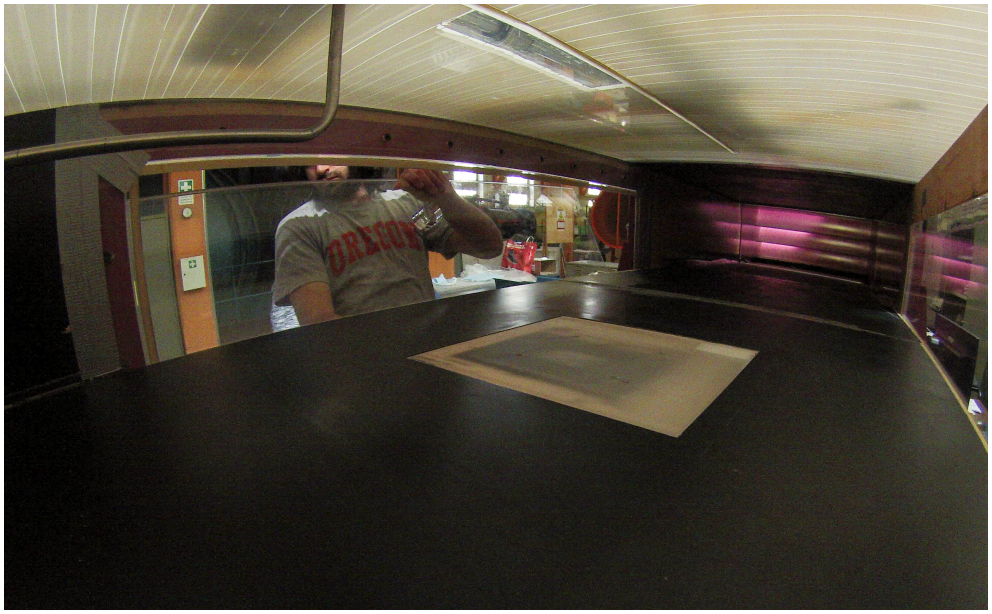

Fig. 4.38: Closure of the test chamber with the acrylic panel, ready to begin the testing.

collecting the environment temperature and pressure, to later define the density and all the other parameters (see chapter 5 for more info) useful in our analysis.

With the software Labview we collected the mean values of the various sensors, starting from the offset-value, collected when the wind tunnel was yet to be powered. Then the wind tunnel was finally powered on, at a speed of 400 RPM, corresponding to about 4.88m/s or Re=491000, sometimes even 350RPM, but we noticed that at this low speed the flow wasn't consistent enough since the wind tunnel wasn't designed for low speed flows. After each collection, the speed was increased up to 1100 RPM, corresponding to a flow speed

Fig. 4.39: Average test run, from left to right: professor Cafiero superintending, fellow graduate student Scrimieri transcribing the data, myself operating the wind tunnel.

of 20.95m/s or a Re=2100000. Once the speed ramp was completed, we varied the height of the riblets by 60 to 100 steps, and then ran the wind tunnel again, collecting the usual data. This was repeated for each plate until we gathered enough data to describe a pattern. Figure 4.39 shows an average test run, from left to right: professor Gioacchino Cafiero superintending the activity, fellow graduate student Luigi Scrimieri transcribing the data, and myself operating the wind tunnel or the stepping motor.

Chapter 5 - Data analysis and results

This chapter will present the complete data analysis and results of the data collected during the research campaign. The presentation is divided in three section: first how the data of force and pressure values were corrected and used to achieve a canonical graph to evaluate any drag reduction or increase effects. Then a section dedicated to the effect on drag by the height of each riblet geometry, and how different heights of the plate could result in an unbelievable drag reduction or even a drag increase. The third section will show the comparison between the various surfaces, previously described in section 4.2, to actually assess if and by how much each riblets geometry could help reduce drag.

5.1 Steps for achieving a drag reduction graph

The first recorded parameters were the temperature and the pressure of the environment of the laboratory, taken before each experimental run. Due to the position of the laboratory, facing Southward and with great windows letting the direct sunlight hit the wind tunnel, temperature and pressure were crucial to record. They were used to calculate the density of the air, the fluid we were working with, with the relation:

$$\rho_{\text{amb}} = \frac{p_{\text{amb}}}{R_{\text{air}} T_{\text{amb}}}$$

with the universal constant R for dry air is equal to 287J/(kgK) and the temperature value is expressed in Kelvin.

Knowing the temperature, it's easy to obtain the viscosity via the Sutherland's (1893) formula:

$$\mu = \frac{\sigma T_{\text{amb}}^{\frac{3}{2}}}{T_{\text{amb}} + \chi}$$

where σ and χ are constant values, with the latter known as Sutherland's constant. For air their values is equal to:

$$\begin{cases} \sigma = 1.458 \cdot 10^{-6} \dfrac{kg}{msK^{\frac{1}{2}}} \\ \chi = 110.4K \end{cases}$$

The kinematic viscosity ν is then obtained by the following ratio:

$$\nu = \frac{\mu}{\rho_{\text{amb}}}$$

The Pitot tube, or perhaps should be called the Bernoulli's tube, since it can provide each component of the simplified form of Bernoulli's equation, was set up to obtain the dynamic pressure:

$$q = P_0 - P = \frac{1}{2}\rho_{\text{amb}} u^2$$

which is the difference between the total pressure exerted by the flow and the static pressure. The velocity is then easily calculated as:

$$u = \sqrt{2q\rho_{\text{amb}}}$$

Hence, knowing the kinematic viscosity, the velocity and the characteristic length of the flat plate equal to 1.6m, the Reynolds number is obtained with the known equation:

$$\text{Re} = \frac{uL}{\nu}$$

The flow speed was also used to calculate the pressure gradient, to later correct the force measured by the 3-axis force

sensor, as in the following relation

$$\frac{dp}{dx} = 0.3416 \frac{\mathrm{Pa} \cdot \mathrm{s}}{\mathrm{m}^2} \cdot u - 0.3018 \frac{\mathrm{Pa}}{\mathrm{m}}$$

where the empirical values are obtained by the various static pressure probes surrounding the plate being tested.

The drag force was directly measured in gram-force, although it needed some corrections. As any other probe, the 3-axis force sensor gives a measure even when the wind tunnel was not powered on: that is the offset value to subtract to the other measured values, as in the following:

$$D = D_{\mathrm{mea}} - \bar{D}_0$$

in which the mean offset value, of a set of three measurements, is subtracted to the value measured during the test run.

However this obtained value was still polluted with the influence of the pressure gradient, for which it had to be corrected with the following relation:

$$D_{\mathrm{true}} = D - 2.5 \cdot \left(0.0045 \frac{S}{g} \frac{dp}{dx} \right)$$

where S is the surface area of the tested plate and g is Earth gravitational acceleration.

Once the corrected drag force is obtained, the drag coefficient is calculated with the following equation:

$$C_{D_{\text{mea}}} = \frac{D_{\text{true}} \cdot g}{\frac{1}{2}\rho S u^2}$$

This measured drag coefficient is then compared to the empirical drag coefficient obtained from the formula

$$C_D = \frac{0.074}{\text{Re}^{0.2}}$$

to obtain finally a percentage with the following equation

$$\% = \frac{C_{D_{\text{mea}}} - C_D}{C_D} \cdot 100$$

If the percentage is the dependent variable value, the independent variable value is defined as the adimensional spacing, calculated with the following equation:

$$s^+ = 20 \cdot \sqrt{\frac{1}{2} C_D u^2} = 20 \cdot \sqrt{\frac{1}{2} \frac{0.074}{\text{Re}^{0.2}} u^2}$$

The graphs comparing the drag reduction capabilities of the various surfaces were obtained by plotting the last two calculated variables.

5.2 Comparisons between surfaces.

The first surface tested was, of course, the flat surface for two main reasons: to validate and benchmark our experimental setup and to assess that the boundary layer in the test chamber was indeed turbulent. As figure 5.1 shows, the obtained drag coefficient from four different acquisitions made with the flat surface, closely follow the theoretical value.

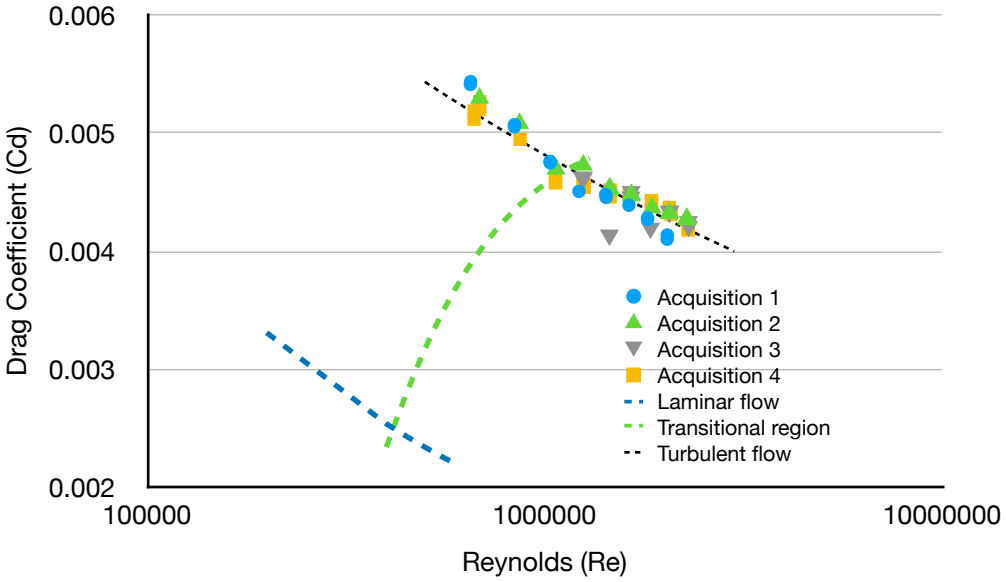

Fig. 5.1: Drag coefficient as a function of Reynolds number for a flat surface.

Once we proved that our procedure and the experimental setup were working as expected, we moved on to test the surface with straight longitudinal riblets. In doing so, since the

alignment of the tip of the riblets to the surrounding surface is crucial, yet very difficult to achieve for the area involved, due to unevenness caused by fluctuations of atmospheric conditions or vibrations of the experimental setup caused by the working wind tunnel, we acquired several data in a range of heights in order to capture the behavior of the riblets at different positions. Starting from the alignment with the riblets tips being at the same level of the surrounding flat surface wall of the test

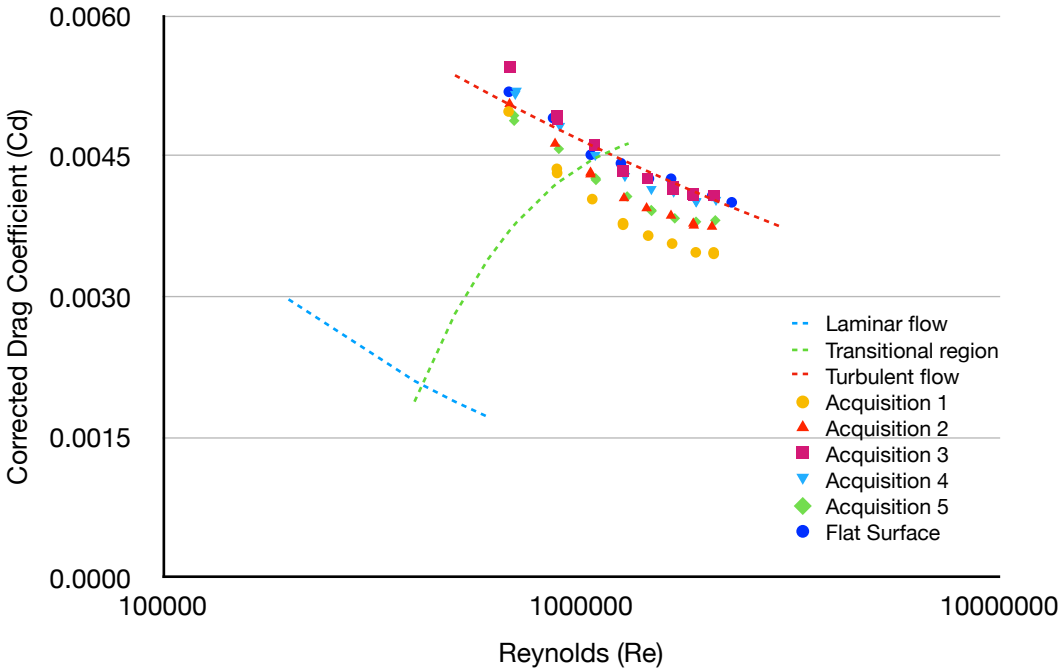

Fig. 5.2: Drag coefficient as a function of Reynolds number for the longitudinal riblets.

chamber, as described in chapter 4, with the stepping motor we increased the height until the riblets troughs were aligned to the wall of the test chamber. In this case the drag coefficient,

as reported in figure 5.2, still sits within the turbulent region, however it is noticeable the reduction as the riblets assume lower positions, with an ideal position corresponding to the midpoint of the riblets being located at the same height of the surrounding wall. As a first glance comparison aid, in figure 5.2

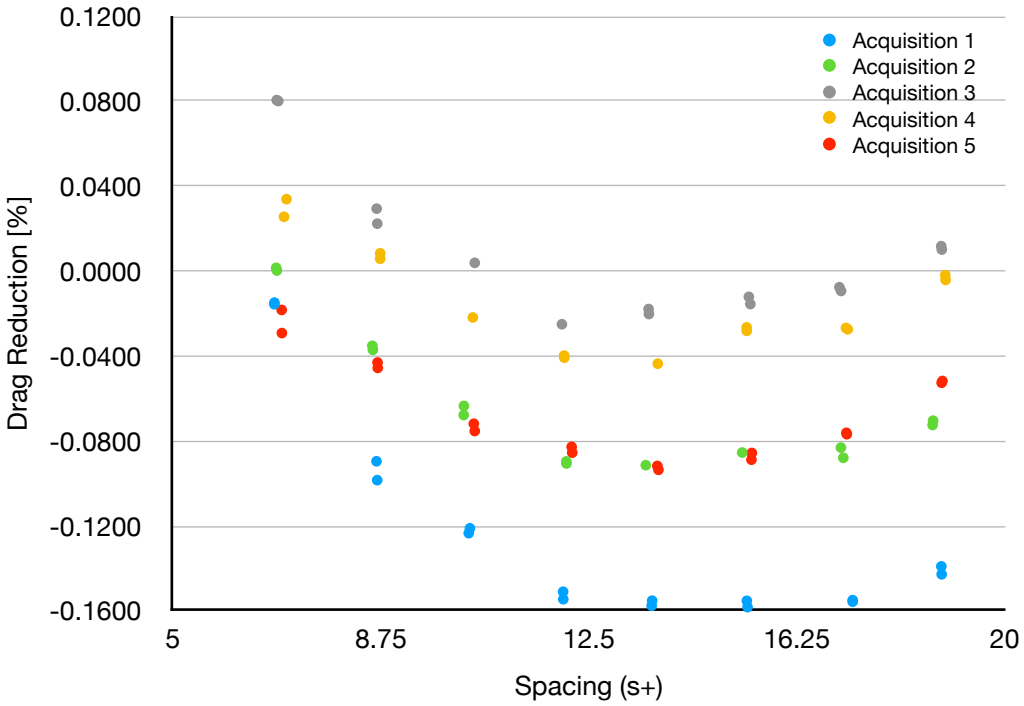

Fig. 5.3: Drag reduction as a function of the spacing for the longitudinal riblets.

the average of the flat surface runs is also reported. In figure 5.3, instead, the percentage points in drag reduction as a function of the spacing are reported. The lowest percentage reductions are to be taken with extreme care, since they obviously are well beyond any other literature for the specific riblets, hence it's possible that the riblets tips were well below

the wall of the test chamber. However we still kept them as the height we measured was well within our predicted range.

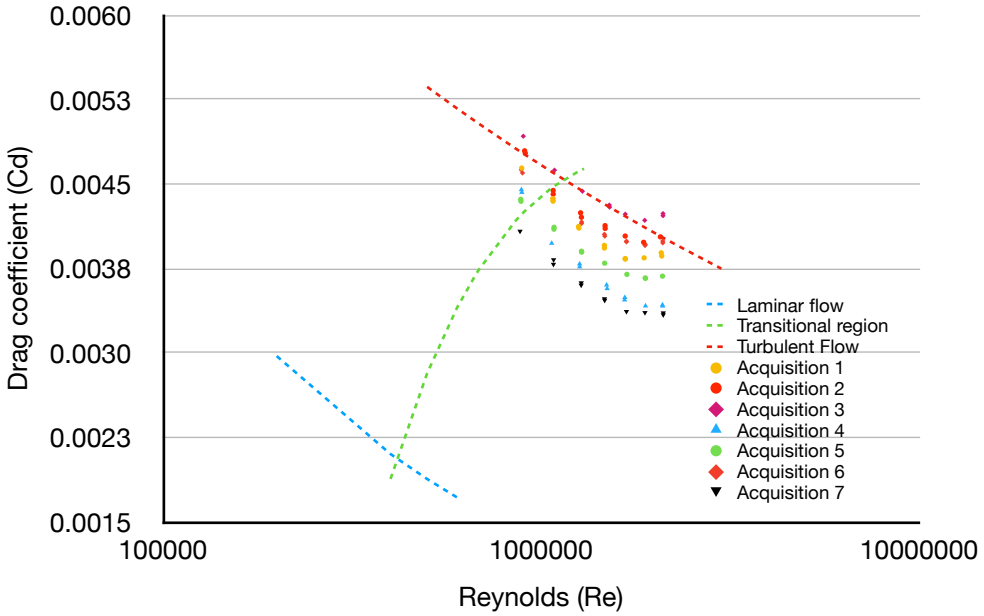

Fig. 5.4: Drag coefficient as a function of Reynolds number for sinusoidal riblets with amplitude a=150μm.

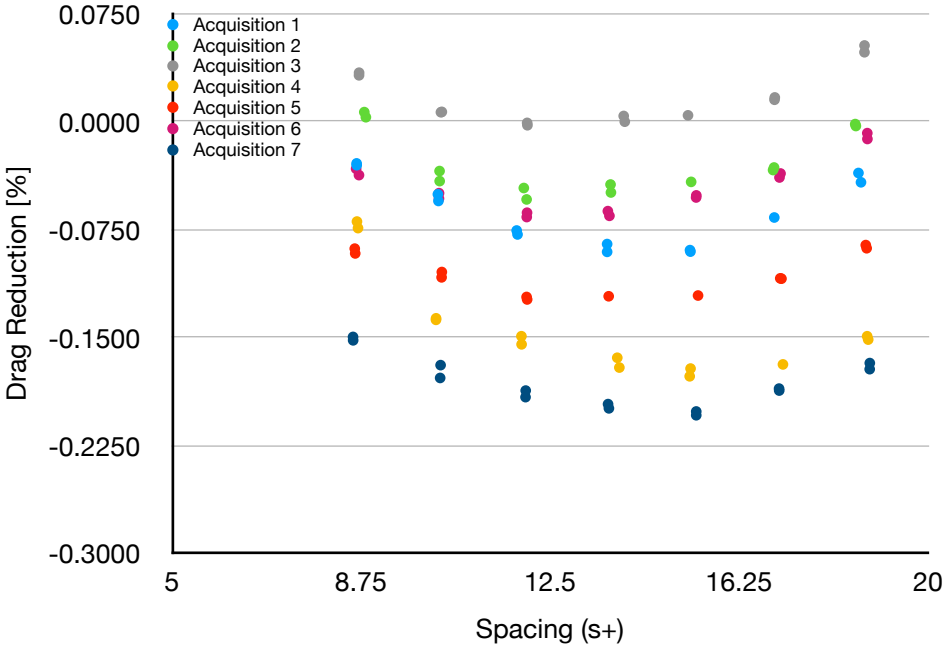

Fig. 5.5: Drag reduction as a function of the spacing for sinusoidal riblets with amplitude a=150μm.

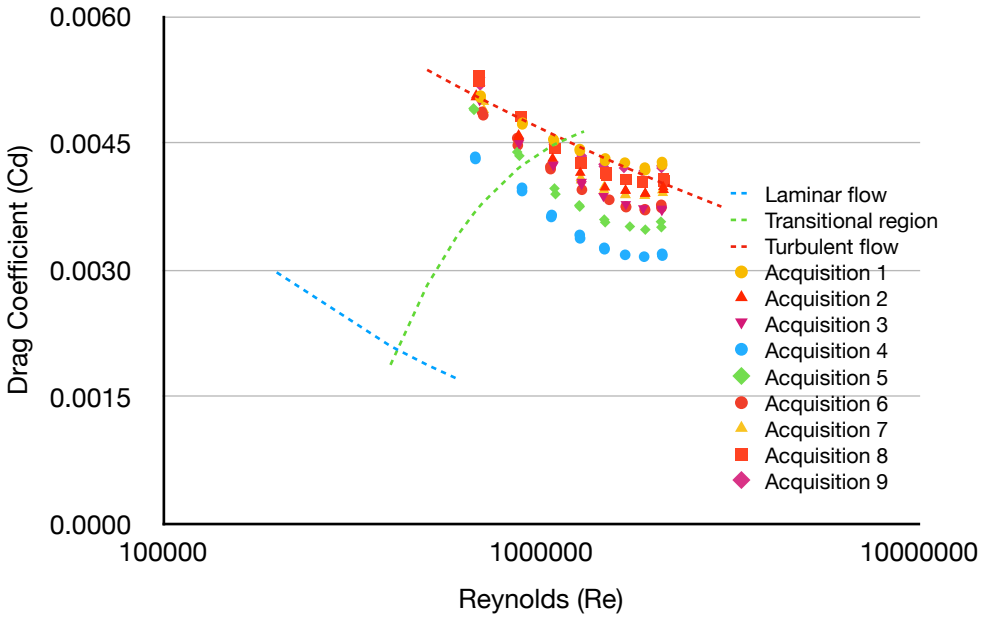

Fig. 5.6: Drag coefficient as a function of Reynolds number for sinusoidal riblets with amplitude a=600μm.

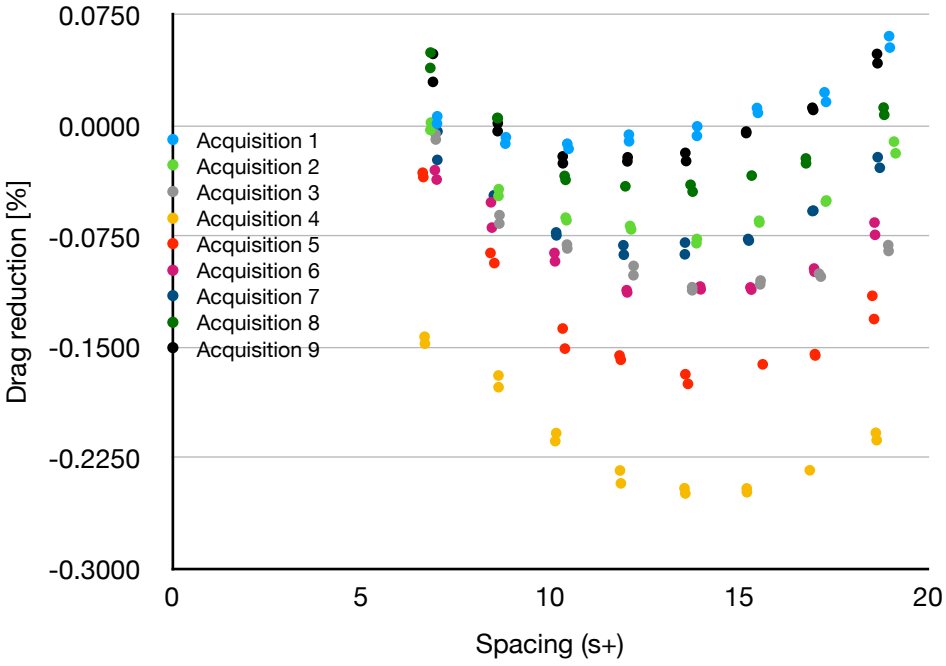

Fig. 5.7: Drag reduction as a function of the spacing for sinusoidal riblets with amplitude a=600μm.

The same was done with the sinusoidal riblets with amplitude a=150μm, reported in figures 5.4 and 5.5, and the

sinusoidal riblets with amplitude a=600μm, reported in figures 5.6 and 5.7. Of greater interest are the graphs depicted in figures 5.8 and 5.9.

They are obtained by averaging the result for each specific surface, with data collected in a height maximum range of 150μm. In figure 5.8 it is highly appreciated how the riblets reduce the drag coefficient compared to the theoretical value of a flat surface, dotted red line, and the experimental flat surface data, yellow dots. This means that for all the instances in which a turbulent boundary is present, having a ribletted surface will produce, even in bad case scenarios, an advantage to a perfectly flat surface.

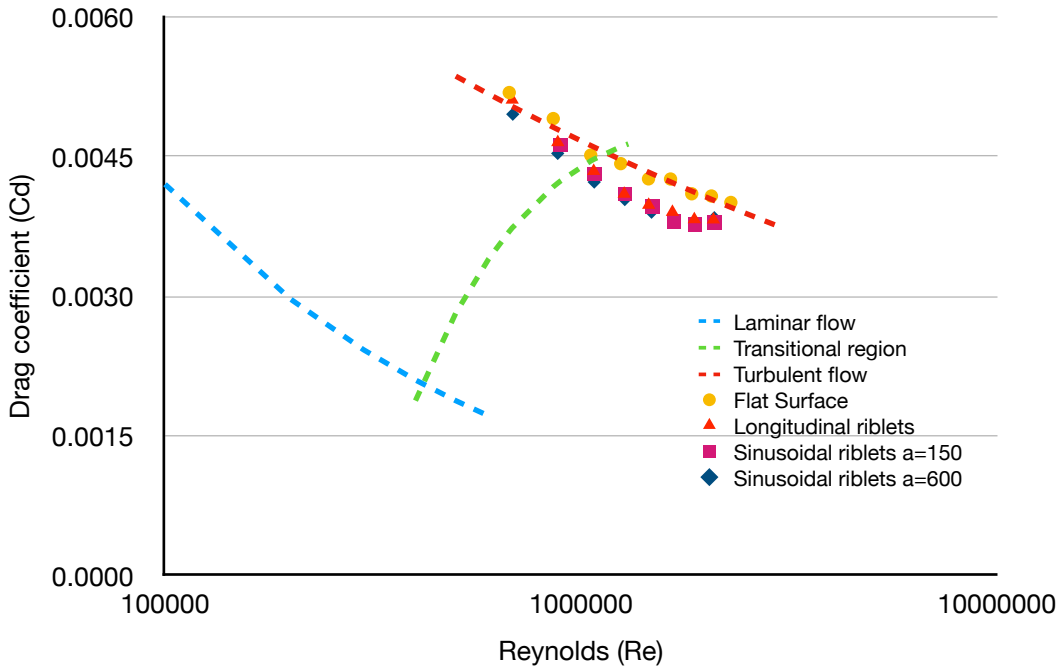

Fig. 5.8: Drag coefficient as a function of Reynolds number for all the studied surfaces.

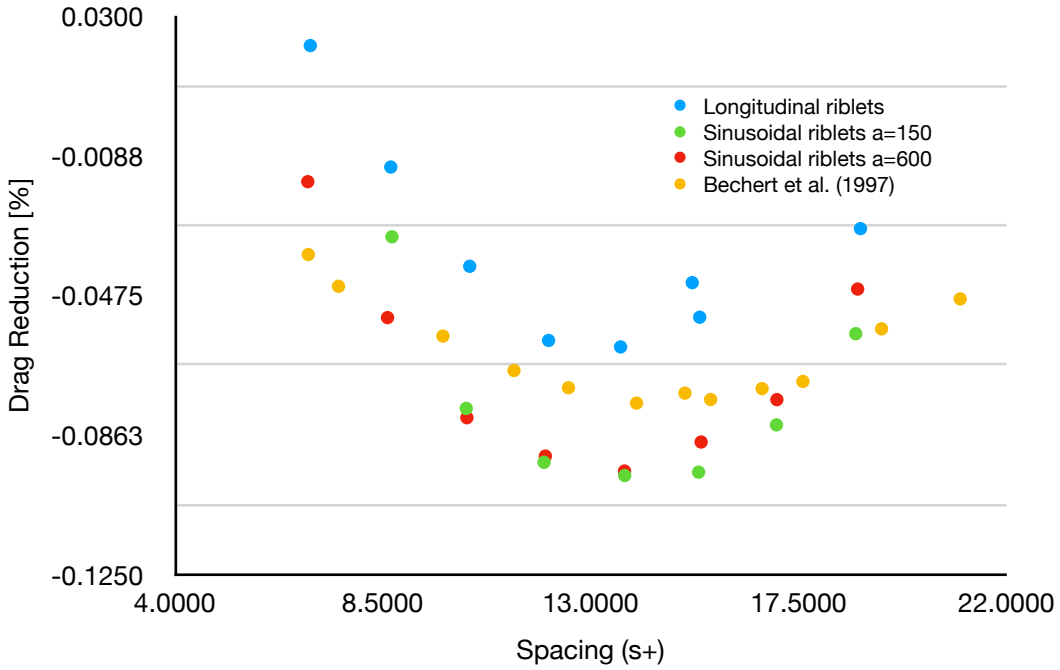

Fig. 5.9: Drag reduction as a function of spacing for all the studied surfaces compared with Bechert et al. (1997) data.

Meanwhile, in figure 5.9, the average percentage of drag reduction of the riblets surfaces studied are compared with the data by Bechert et al. (1997). Bechert's data are represented by the yellow dots and they are between our obtained values of the longitudinal riblets, with a maximum average drag reduction of 6.18%, and of the sinusoidal riblets, which, regardless of their amplitude, the maximum average drag reduction obtained is around 9.5%. This result is consistent with what we expected, however, to better characterize each amplitude, a more refined way of alignment must be implemented, along with a more rigid and insulated

experimental setup, in order to avoid any vibration from the wind tunnel engines.

6. Conclusions and final considerations

Although research is ongoing and it's quite promising, the actual uses are still limited, despite the optimism of researchers on a working technology that even in 1989 Choi wrote that it was very close to industrial applications. The primary industry for this type of research, even if it has achieved great results in more efficient engines offering very performing aircrafts such Airbus' A350 and Boeing's B787-Dreamliner and B777, has not fully embraced this technology born as a reaction to the oil crisis of the early 1970's. Only few times there have been experimental applications on actual aircrafts. Notably the firstly mentioned Szodruch (1991), which conducted a drag reduction experiment by covering 70% of an Airbus A320 aircraft, as shown in figure 1.1, in 3M riblet film, reporting a total drag reduction shy of 2% at common Mach numbers for that aircraft in cruise. Beneficial effect of riblets were also reported at supersonic speed of between 1.2 and 1.6, hence very high Reynolds numbers. In this case Zuniga et al. (1992) equipped

3M riblets on a Lockheed F-104G flight test fixture, shown in figure 6.x, finding a drag reduction of up to 15% in drag coefficients, as seen in figure 6.xx. Other tests were made using scaled down models of aircrafts, such as the Dornier 328 aircraft studied by Hoeven and Bechert (1991). They found even an improvement of the lift coefficient, in the order of 1%, without compromising the maximum value nor the corresponding stall angle, as seen in figure 6.xxx. Bechert and Hage (2006) argued on some reasons why the industry has been reluctant on a widespread use of such films. Some of the issues, at least 15 years ago, could have been rational; for instance the quality of adhesive, possible damage from UV radiation and overall maintenance, to which even Bechert and Hage (2006) argued on how far the improvements have gotten in the adhesive research, and even in the plastic film manufacturing, by using fluorine, able to protect from UV radiation and also being a dirt repellent. However also economics fluctuations have to be considered on this research: as a major example is the Airbus A380. Designed in an era of major increase in the airline industry, Airbus announced in 2019 that its production would stop by 2021, as reported by

Schwartz (2019) for NPR. Also Boeing 747-8 doesn’t fly as a passenger aircraft for any U.S. airline, as reported in an article by Ostrower (2017) for CNN. So one is left with the consideration that Bechert and Hage (2006) proposed: they argued that if airlines would equip their fleet with riblets film, they would see a profit increase of about one million dollars (2006 dollars) per aircraft per year, but they also noted that the same amount has been invested for the riblet research every year, wondering if "this research has been too expensive".

Probably not, since by studying the flow above the riblets, we sure improve our understanding of the turbulent boundary layer and we are not able to foresee any future invention that this understanding could sparkle. After all, only in 1903 humans have successfully lifted from Earth with a motorized aircraft, in 1957 we reached space, and in 2021 we have flown the first aircraft on another planet: Mars.

References

Abe H., Kawamura H., Matsuo Y., 2004, "Surface heat-flux fluctuations in a turbulent channel flow up to Re_τ=1020 with Pr=0.025 and 0.71.", Int J Heat Fluid Flow, 25:404-19.

Adrian R. J., Meinhart C. D., Tomkins C. D., 2000, "Vortex organization in the outer region of the turbulent boundary layer.", J. Fluid Mech, 411, 1-54.

Akinlade, O. G., 2005, "Effects of surface roughness on the flow characteristics in a turbulent boundary layer", Department of mechanical engineering, University of Saskatchewan, Saskatoon, Canada.

Azad R., Burhanuddin S., 1983, "Measurements of some features of turbulence in wall-proximity.", Exp Fluids, 1:149-60.

Bechert D. W., Bruse M., Hage W., Van Der Hieven J. G. T., 1997, "Experiments on drag-reducing surfaces and their optimization with an adjustable geometry.", J. Fluid Mech., vol 338, pp. 59-87.

Bechert D. W., Bruse M., Hage W., 2000, "Experiments with three-dimensional riblets as an idealized model of shark skin.", Experiments in Fluid 28, 403-412.

Bechert D. W., Hage W., 2006, "Drag reduction with riblets in nature and engineering.", WIT transactions on state of the art in science and engineering, vol. 4, WIT Press.

Bechert D. W., Hoppe G., Reif W.-E., 1985, "On the drag reduction of the shark skin.", AIAA-Paper 85-0546.

Bernard P., Wallace J., 2002, "Turbulent flow: analysis, measurement and prediction", NJ, USA: John Wiley & Sons, Inc.

Black T. J., 1968, "An analytical study of the measured wall pressure field under supersonic turbulent boundary layers.", Nasa CR-888.

Blackwelder R. S., Haritonidis J., 1983, "Scaling of the bursting frequency in turbulent boundary layers.", J Fluid Mech, 132:87-103.

Blackwelder R. S., Kovasznay L. S. G., 1972, "Time scales and correlation in a turbulent boundary layer.", Phys. Fluids, vol. 15, no. 9.

Bradshaw P., Huang G. P., 1995, "The law of the wall in turbulent flow.", Proc R Soc Lond A 451:165-188.

Cenedese A., Romano G. P., Antonia R. A., 1998, "A comment on the linear law of the wall for fully developed turbulent change flow", Exp Fluid, 25:165-70

Chauhan K. A., Monkewitz P. A., Nagib H. M., 2009, "Criteria for assessing experiments in zero pressure gradient boundary layers.", Fluid Dyn Res, 41:021-404.

Chen H., Rao F., Shang X., Zhang D., Hagiwara I., 2014, "Flow over bio-inspired 3D herringbone wall riblets.", Exp Fluids, 55.1698.

Choi K.-S., 1985, "Near-wall turbulence structure on a riblet wall.", BMT Ltd, Feltham, Middlesex, UK.

Choi K.-S., 1989, "Near-wall structure of a turbulent boundary layer with riblets.", J. Fluid Mech. vol. 208, pp. 417-458.

Choi H., Moin P., Kim J., 1993, "Direct numerical simulation of turbulent flow over riblets.", J. Fluid Mech., vol. 255, 503-539.

Clauser F. H., 1956, "The turbulent boundary layer", Adv Appl. Mech., 4:1-51.

Coles D.., 1956, "The law of the wake in the turbulent boundary layer", J Fluid Mech, 1:191-226.

Corino E. R., Brodkey R. S., 1969, "A visual investigation of the wall region in turbulent flow.", J. Fluid Mech., Vol. 37, pt. 1.

Corrsin S., 1943, "Investigation of flow in an axially symmetric heated jet of air." NACA Adv. Conf. Rep. 3123

Einstein H. A., Li H., 1956, "The viscous sublayer along a smooth boundary." J. Eng. Mech. Div. ASCE 82(EM2) Pap. No. 945.

Falco R. E., 1972, "Coherent motions in the outer region of turbulent boundary layer.", Phys. Fluids Suppl. vol. 20, no. 10.

Falco R. E., 1980, "The production of turbulence near a wall.", AIAA Paper 80-1356.

Falco R. E., 1982, "A synthesis and model of wall region turbulence structure.", Structure of turbulence, heat and mass transfer, p. 124, Hemisphere.

Grass A. J., 1971, "Structural features of turbulent flow over smooth and rough boundaries.", J. Fluid. Mech. Vol. 50.

Gren P., 1987, "Structured surfaces and turbulence.", licentiate thesis, Division of Fluid mechanics, Lulea University, Sweden.

Head M. R., Bandyopadhyay P., 1981, "New aspects of turbulent boundary layer structure.", J. Fluid Mech., vol. 107.

Hutchins N., Choi K., 2002, "Accurate measurements of local skin friction coefficient using hot-wire anemometry.", Prog Aerosp sci, 38:421-46.

Kawamura H., Abe H., Matsuo Y., 1999, "Dns of turbulent heat transfer in channel flow with respect to Reynolds and Prandtl number effects.", Int J Heat Fluid Flow, 20:196-207.

Kim H. T., Kline S. J., Reynolds W. C., 1971, "The production of turbulence near a smooth wall in a turbulent boundary layer", J. Fluid Mech., 50:133-60.

Kline S. J., Reynolds W. C., Schrod F. A., Runstadler P. W., 1967, "The structure of turbulent boundary layers", J. Fluid Mech., Vol. 30.

Kline S. J., Robinson S. K., 1989 a, "Quasi-coherent structures in the turbulent boundary layer. Part I: status report on a community-wide summary of the data." Near Wall Turbulence. Proc Zaric Meml. Conf., 1988 ed. S. J. Kline, N. H. Afghan, pp. 200-17. New York: Hemisphere.

Kline S. J. Robinson S. K., 1989 b, "Turbulent boundary layer structure: progress, status, and challenges.", Proc. IUTAM Symp Struct of Turbulence and Drag Reduction, 2nd, Zurich.

Kline S. J., Runstadler P. W., 1959, "Some preliminary results of visual studies of the flow mode of the wall layers of the turbulent boundary layer.", Trans ASME, Ser. E 2:166-70.

Kramer F., Grüneberger R., Thiele F., Wassen E., Hage W., Meyer R., 2010, "Wavy riblets for turbulent drag reduction.", 5th Flow control conference, Chicago, Illinois, AIAA 2010-4583.

Liu Z. C., Adrian R. J., 1998, "Visualization of hairpin vortex structure with PIV and DNS.", 8th International symposium on flow visualization, Sorrento, Italy, 1st -4th September 1998.

Luchini P., 1992, "Effects of riblets on the growth of laminar and turbulent boundary layers.", The 7th European drag reduction meeting, 24-25 September, Berlin, Germany.

Luchini P., Manzo F., Pozzi A., 1991, "Resistance of a grooved surface to parallel flow and cross-flow.", K. Fluid Mech., vol. 228, 87-109.

Magro C., 2017, "Bilancia aerodinamica per la determinazione della resistenza d'attrito su una placca piana: validazione della tecnica di misura.", Dipartimento di Ingegneria Aerospaziale, Politecnico di Torino.

McKeon B., Li J. D., Jiang W., Morrison J. F., Smits A. J., 2004, "Further observations one the mean velocity distribution in fully developed pipe flow.", J Fluid Mech, 501:135-47.

Millikan C. B., 1938, "A critical discussion of turbulent flows in channels and circular tubes", Proceedings of the 5th international congress on applied mechanics, Cambridge, MA, USA, p.386-92.

Moin P., Kim J., 1985, "The structure of the vorticity field in turbulent channel flow. Part 1: analysis of instantaneous fields and statistical correlations.", J. Fluid Mech., vol. 155.

Monin A. S., Yaglom A. M., 1971, "Statistical fluid mechanics: mechanics of turbulence.", vol. 1, Cambridge, MA, MIT press.

Nychas S. G., Hershey H. C., Brodkey R. S., 1973, "A visual study of turbulent shear flow.", J. Fluid Mech., Vol. 61.

Offen G. R., Kline S. J., 1974, "Combined dye-streak and hydrogen-bubble visual observations of a turbulent boundary layer." J. Fluid Mech. 62:223-39.

Offen G. R., Kline S. J., 1975, "A proposed model of the bursting process in turbulent boundary layers.", J. Fluid. Mech. 70:209-28.

Örlü R., Fransson J. H. M., Alfredsson P. H., 2010, "On near wall measurements of wall bounded flows — The necessity of an accurate determination of the wall position", Progress in Aerospace Sciences, 46, 353-387.

Ostrower J., 2017, "Boeing's 747 jumbo passenger plane is on the way out.", https://money.cnn.com/2017/07/19/news/companies/the-last-747-jumbo-jetliner/index.html

Park J., Y., Chung M., K., 2004, "Revisit of viscous sublayer scaling law", Phys fluid, 16:478-81.

Patel V. C., 1965, Calibration of the Preston tube and limitations on its use in pressure gradients.", J Fluid Mech, 23:185-208

Patel V. C., Head M. R., 1969, "Some observations on skin friction and velocity profiles in fully developed pipe and channel flow.", J. Fluid Mech, 38:181-201.

Peet Y., Sagaut P., Charron Y., 2008, "Turbulent drag reduction using sinusoidal riblets with triangular cross-section.", The 38th AIAA fluid dynamics conference and exhibit, AIAA 2008-3745:9.

Petersohn E., 1959, "Concerning an investigation of the flow in pipes, internally covered with shark skin.", AE-I-444, FFA, The aeronautical research institute of Sweden.

Pope S., 2000, "Turbulent flows", Cambridge, UK: Cambridge University Press.

Prandtl L., 1925, "Bericht über Untersuchungen zur ausgebildeten Turbulenz", ZAMM, 5:136-9.

Prandtl L., 1932, "Zur turbulenten Strömung in Rohren und längs platten." Ergebnisse der Aerodynamischen Versuchsanstalt zu Göttingen, 4:18-29.

Purtell L. P., Klebanoff P. S., Buckley F. T., 1981, "Turbulent boundary layer at low Reynolds number.", Phys Fluids, 24:802-811.

Reif W. E., Dinkelacker A., 1982, "Hydrodynamics of the squamation in fast swimming sharks.", Neues Jahrbuch für Geologie und Paläontologe, Abhandlungen, 164, pp. 184-187.

Reif W. E., 1985, "Squamation and ecology of sharks.", Courier Forschungsinstitut Senckenberg Nr. 78, pp 1-255, Frankfurt am Main.

Robinson S. K., 1991. "The kinematics of turbulent boundary layer structure.", Nasa Tech. Mem. 103859.

Schwartz M. S., 2019, "Airbus To Stop Production Of A380 Superjumbo Jet.", https://www.npr.org/2019/02/14/694620105/airbus-to-stop-production-of-a380-superjumbo-jet

Smith C. R., Metzler S. P., 1983, "The characteristics of low-speed streaks in the near-wall region of a turbulent boundary layer.", J. Fluid Mech., Vol. 129.

Sutherland W., 1893, "LII. The viscosity of mass and molecular force.", The London, Edinburgh, and Dublin philosophical magazine and journal of science, vol. 36 (223):507-531.

Szodruch J., 1991 "Viscous drag reductions on transport aircraft", AIAA Paper 91-0685.

Theodorsen T., 1952, "Mechanism of turbulence.", Proc 2nd Midwestern conference on Fluid Mech., Ohio State University, Columbus, Ohio.

Townsend A. A., 1956, "The structure of turbulent shear flow", Cambridge Univ. press, 315 pp 1st ed.

Townsend A. A., 1976, "The structure of turbulent shear flow." 2nd edition Cambridge, UK, Cambridge University press.

Tsukahara T., Seki Y., Kawamura H., Tochio D., 2005, "DNS of turbulent channel flow at very low Reynolds numbers.", Proceedings of the 4th international symposium on turbulence and shear flow phenomena, Williamsburg, USA, p. 935-40.

Von Kármán T., 1930, "Mechanische Ähnlichkeit und Turbulenz in: Proceedings of the 3rd international congress on applied mechanics", Stockholm, Sweden, p. 85-93.

Wallace J. M., Eckelmann H., Brodkey R. S., 1972, "Thee wall region in turbulent shear flow.", vol. 54, pt. 1.

Walsh M. J., Lindeman A. M., 1984, "Optimization and application of riblets for turbulent drag reduction.", AIAA Paper 84-0347.

Walsh M. J., 1990, "Viscous drag reduction in boundary layers.", eds. D. M. Bushnell & J. N: Hefner, Progress inn Astronautics and Aeronautics, vol. 123, AIAA: Washington, pp. 203-262.

Wei T., Schmidt R., McMurtry P., 2005, "Comment on the Clauser chart method for determining the friction velocity", Experiments in Fluids, 38:695-699.

Weiss M. H., 1993, "Drag reduction with riblets in pipe flow.", Phd Diss., University of Calgary, Alberta, Canada.

Willmarth W. W., Tu B. J., 1967, "Structure of turbulence in the boundary layer near the wall.", Phys. Fluids, vol. 10, p. S134.

Willmarth W. W., Lu S. S., 1972, "Structure of the Reynolds stress near the wall.", J. Fluid Mech., Vol. 55.

Zagarola M. V., Smits A. J., 1998, "A new mean velocity scaling for turbulent boundary layers", Proceedings of FEDSM ’98.

Zhang D. Y., Luo Y. H., Chen H. W., Jiang X. G., 2011, "Exploring drag-reducing grooved internal coating for gas pipelines.", Pipeline Gas Journal, 238(3):58-61.

Zhou J., Adrian R. J., Balachandar S., 1996, "Autogeneration of near-wall vortical structures in channel flow.", Phys. Fluids 8, 288-290.

Zhou J., Adrian R. J., Balachandar S., Kendall T. M., 1999, "Mechanisms for generating coherent packets of hairpin vortices in channel flow.", J. Fluid. Mech. 387, 353-396.

Zhou J., Meinhart C.D., Balachandar S., Adrian R. J., 1997, "Formation of coherent hairpin packets in wall turbulence.", Self-sustaining mechanisms of wall turbulence (ed. R. L. Panton), pp 109-134. Computational mechanics, Southampton, UK.

Zuniga F. A., Anderson B. T., Bertelrud A., 1992, "Flight test results of riblets at supersonic speeds.", Nasa Tech Memo 4387.